

# **Utilisation of Waste Heat Energy from an Internal Combustion Engine for Tri-Generation**

**Noman Uddin Yousuf**

A thesis submitted to

Auckland University of Technology

in fulfilment of the requirements for the degree of

**Doctor of Philosophy (PhD)**

**2017**

School of Engineering, Computer and Mathematical Sciences

# ABSTRACT

This thesis presents an investigation of the utilisation of waste heat energy from an internal combustion engine for tri-generation. In articulating this, a preliminary experimental investigation was performed which involved employing waste heat from a diesel engine to drive a diffusion absorption refrigeration (DAR) system and a water heater system. Based on the experimental results it was found that the performance of this type of tri-generation system was severely limited by the narrow operating range and cooling capacity of the DAR cycle.

To understand the narrow operating range, the DAR cycle was modeled for steady state operating conditions. Using a sensitivity analysis, it was found that the generator temperature significantly influences the overall performance of the DAR system. It was hypothesised that this performance could be enhanced through an improved thermal driven bubble pump.

To better understand the DAR bubble pump, an airlift based bubble pump system was developed to produce controllable operating conditions. Experiments on the airlift based bubble pump system were performed to characterise different two-phase flow regimes inside the single lift-tube of the bubble pump. Four flow regimes were identified and mapped based on the superficial velocities of the air and water. Furthermore, it was found that the performance of the bubble pump was affected by the lift-tube diameter, submergence ratio, and airflow rate.

Having examined the operating characteristics of the bubble pump experimentally, a model was developed to predict its performance. To realise this model, empirical

correlations were developed to determine the void fraction for each flow regime. The model reinforced the finding of limited pumping capacity from a single lift-tube.

However, to overcome the limited pumping capability of single lift-tube bubble pump, multiple lift-tubes were examined as a way to improve the pumping performance. It was found that using multiple lift-tubes is a viable solution as it improves the pumping capacity of the bubble pump. However, the flow rate of each lift-tube in a multiple lift-tube configuration was observed to be non-uniform. Analytical modelling of a multiple lift-tube bubble pump showed an inability to accurately predict the pumping characteristics. To overcome this, a novel artificial neural network (ANN) technique was used to predict their pumping capacity. The results showed that the ANN was capable of accurately predicting the performance of the multiple-lift tube bubble pump.

Finally, the influence of multiple lift-tubes on the performance of the DAR system integrated in a tri-generation system was examined. It was found that at high heat inputs, a DAR system with a multiple lift-tubes bubble pump showed an increase in performance and an improved operating range for an internal combustion engine driven tri-generation system using a diffusion absorption refrigeration.

# ACKNOWLEDGEMENT

First of all, thanks to Almighty Allah for His infinite blessing and making me capable enough to pursue and complete this research work.

I wish to express my sincerest gratitude to the NED University of Engineering and Technology, Pakistan for giving me the opportunity to pursue this doctoral research here at the Auckland University of Technology, New Zealand.

This research work would not be possible without the professional guidance, patience and support from my supervisors: Dr. Timothy Anderson, Dr. Michael Gschwendtner, and Dr. Roy Nates. I would like to express my heartiest gratitude to them for my professional and personal development. Whenever I felt low, their sincere support was a source of inspiration and motivation. They helped me a lot in growing my confidence, ability to work independently, improving my critical thinking, and capability to deliver solutions.

My gratitude goes to AUT and the School of Engineering who supported this research in many ways. In particular, the administrative staff especially Josephine Prasad for taking care of different matters. I thank Jim Crossen, Mark Masterton, and Tim Luton from the mechanical workshop for their continuous support in building test rigs.

I would especially like to thank my research colleagues Piratheepan, Reza, Aziz, Uzair, and Waseem for the valuable discussions and help during this journey.

My deepest appreciation goes to my dear parents, Nasir Uddin Yousuf and Nishat Rukhsana for their love and care to which I will always be in debt. They have provided me the best possible environment in bringing me up as a better human being. I would like to thank my loving and caring wife Ifra Noman for her continuous support in completing this task and my little baby boy Usman Uddin Yousuf who has brought a joy to our life. I would like to thank my brother, Nadeem Uddin Yousuf for his continuous support and help. I wish to thank all my relatives and friends, in New Zealand and back in Pakistan for their moral support and best wishes.

# **LIST OF PUBLICATIONS**

Yousuf, N., Anderson, T., Gschwendtner, M. and Nates, R., 2016, “Predicting the Pumping Characteristics of Multiple Parallel Tube Airlift Pumps”, Proceedings of the 20<sup>th</sup> Australasian Fluid Mechanics Conference, Perth, December 2016

Yousuf, N., Anderson, T., Gschwendtner, M. and Nates, R., 2016, “Performance of a Cooling System Driven by Engine Exhaust Heat”, Proceedings of the 4<sup>th</sup> International Conference on Sustainability and the Cold Chain, Auckland, April 2016

Yousuf, N., Biteau, E., Anderson, T., Gschwendtner, M. and Nates. R., 2014, “Modelling the Performance of a Diffusion Absorption Refrigeration System”, Proceedings of the 2014 Asia-Pacific Solar Research Conference, Sydney, December 2014

# TABLE OF CONTENTS

ABSTRACT .....	ii
ACKNOWLEDGEMENT .....	iv
LIST OF PUBLICATIONS .....	vi
TABLE OF CONTENTS .....	vii
LIST OF FIGURES .....	xii
LIST OF TABLES .....	xvii
NOMENCLATURE.....	xviii
ATTESTATION OF AUTHORSHIP .....	xxii
Chapter 1: Introduction .....	1
1.1    Overview .....	1
1.2    Waste heat .....	3
1.3    Co-generation .....	5
1.4    Tri-generation .....	5
1.4.1    Components of tri-generation systems .....	6
1.4.2    ICE based tri-generation system .....	7
1.4.3    Decentralised tri-generation system .....	8
1.4.4    Studies on decentralised tri-generation systems .....	8
1.5    Research Question .....	11
Chapter 2: Preliminary experimental investigation.....	12

2.1	Selection of tri-generation components.....	12
2.1.1	Selection of an ICE .....	12
2.1.2	Selection of refrigeration technology.....	13
2.2	Experimental method .....	16
2.3	Energy analysis.....	18
2.4	Results and discussion.....	19
2.5	Conclusion.....	24
Chapter 3: Modelling the performance of a diffusion absorption refrigeration system..		26
3.1	Introduction .....	26
3.2	Working principle.....	26
3.3	Previous studies on DAR systems.....	29
3.4	Thermodynamic analysis of diffusion absorption refrigeration system .....	31
3.4.1	Generator.....	33
3.4.2	Bubble pump .....	33
3.4.3	Separator .....	34
3.4.4	Rectifier.....	34
3.4.5	Condenser.....	35
3.4.6	Evaporator .....	35
3.4.7	Gas heat exchanger .....	36
3.4.8	Absorber.....	37
3.4.9	Solution heat exchanger .....	38
3.4.10	Performance parameters.....	38



3.5	Solution verification of the model.....	39
3.6	Influence of system parameters and components.....	40
3.6.1	Influence of generator temperature on performance.....	41
3.6.2	Influence of generator temperature on circulation ratio.....	43
3.6.3	Influence of strong solution mass fraction on COP .....	44
3.6.4	Influence of rectifier.....	44
3.6.5	Influence of evaporator temperature on COP .....	46
3.6.6	Influence of condenser temperature on COP .....	47
3.7	Comparison between DAR model and preliminary experiment .....	48
3.8	Conclusion.....	49
Chapter 4: Performance analysis of a bubble pump.....		51
4.1	Overview .....	51
4.2	Experimental method .....	55
4.3	Experimental results .....	57
4.3.1	Flow visualization .....	57
4.3.2	Influence of the submergence ratio .....	63
4.3.3	Influence of the lift-tube diameter.....	65
4.4	Flow regime map.....	67
4.5	Bubble pump model .....	69
4.6	Void fraction models .....	76
4.6.1	Homogenous flow model .....	76
4.6.2	Separate flow model.....	77

4.6.3	Drift flux model.....	77
4.7	Estimation of the parameters of drift flux model .....	78
4.8	Experimental method .....	79
4.9	Comparison between model and experimental results .....	83
4.10	Performance of a heat driven bubble pump.....	86
4.11	Concluding remarks .....	89
Chapter 5: Influence of multiple lift-tube on the performance of bubble pump.....		91
5.1	Overview .....	91
5.2	Experimental method .....	93
5.3	Experimental results .....	94
5.3.1	Observation of flow regimes in multiple lift-tubes.....	94
5.3.2	Influence of the additional lift-tube.....	98
5.4	Multiple lift-tube bubble pump modelling .....	100
5.5	Concluding remarks .....	103
Chapter 6: Artificial neural network based modelling of a multiple lift-tube bubble pump.....		104
6.1	Overview .....	104
6.2	Method.....	105
6.3	Results and discussions .....	109
6.4	Predicting the performance of heat driven bubble pump .....	115
6.5	Concluding remarks .....	116
Chapter 7: Influence of lift-tube quantity on the performance of a DAR tri-generation system.....		118

7.1	Overview .....	118
7.2	Modelling scheme .....	118
7.3	Result and discussion .....	120
7.4	Conclusion.....	124
Chapter 8: Conclusions and recommendations .....		126
8.1	Conclusions .....	126
8.2	Recommendations .....	127
References .....		129
Appendix A: Energy analysis.....		138
A.1	Refrigeration effect.....	138
A.2	Heat transfer to DAR system.....	139
Appendix B: Uncertainty analysis .....		141
Appendix C: Predicting the performance of a heat driven bubble pump.....		144
Appendix D: Experimental data of an airlift pump.....		151

# LIST OF FIGURES

Figure 1: Primary energy consumption by region (Jradi and Riffat, 2014) .....	1
Figure 2: Global energy consumption by fuel (Jradi and Riffat, 2014) .....	2
Figure 3: Approaches for utilisation of waste heat energy .....	4
Figure 4: Schematic diagram of an ICE based tri-generation system .....	7
Figure 5: Absorption cooling system (Srikhirin and Aphornratna, 2002) .....	13
Figure 6: Electricity utilisation for alternative cooling technology (Hughes et al., 2011) .....	14
Figure 7: Diffusion absorption refrigeration system (Rodriguez-Munoz and Belman-Flores, 2014) .....	15
Figure 8: Schematic of the experimental tri-generation setup .....	16
Figure 9: Temperature profile at 50% CCP mode .....	19
Figure 10: Temperature profile at 75% CCP mode .....	20
Figure 11: Temperature profile at 100% CCP mode .....	21
Figure 12: Temperature profile at 100% CCHP mode.....	22
Figure 13: Performance of the DAR system at different operating modes.....	23
Figure 14: Useful output energy at different operating modes .....	24
Figure 15: Schematic of a diffusion absorption refrigeration cycle.....	27
Figure 16: Schematic of the diffusion absorption refrigeration system.....	32
Figure 17: Influence of generator temperature on COP .....	41
Figure 18: Influence of generator temperature on ammonia mass fraction of vapours leaving generator .....	42

Figure 19: Influence of generator temperature on circulation ratio .....	43
Figure 20: Influence of ammonia mass fraction of strong solution on COP .....	44
Figure 21: Influence of mass fraction of ammonia vapour entering condenser on COP .....	45
Figure 22: Influence of evaporator temperature on COP.....	46
Figure 23: Ratio of inert gas flow rate to refrigerant flow rate .....	47
Figure 24: Influence of condenser temperature on COP.....	48
Figure 25: Schematic of a bubble pump .....	51
Figure 26: Vertical two-phase flow regimes (Montoya et al. 2016) .....	52
Figure 27: Schematic of the experimental setup .....	56
Figure 28: Bubbly flow regime .....	57
Figure 29: Bubble train comprising of small air slugs.....	58
Figure 30: Taylor bubbles in a slug flow regime .....	59
Figure 31: Unstable churn flow regime .....	60
Figure 32: Annular flow regime.....	61
Figure 33: Flow regime visualisation and performance of a 10 mm lift-tube airlift pump at submergence ratio of 0.5 .....	62
Figure 34: Performance of 10 mm lift-tube airlift pump at different values of submergence ratio .....	63
Figure 35: Performance of 14 mm lift-tube airlift pump at different values of submergence ratio .....	64
Figure 36: Influence of lift-tube diameter on the performance of airlift pump at submergence ratio of 0.3 .....	65
Figure 37: Influence of lift-tube diameter on the performance of airlift pump at submergence ratio of 0.5 .....	66

Figure 38: Influence of lift-tube diameter on the performance of airlift pump at submergence ratio of 0.7 .....	66
Figure 39: Experimental flow regime map .....	68
Figure 40: Schematic of a bubble pump .....	69
Figure 41: Schematic of the quick close valve technique .....	79
Figure 42: Correlation for bubbly flow regime.....	80
Figure 43: Correlation for slug flow regime .....	81
Figure 44: Correlation for churn flow regime.....	81
Figure 45: Correlation for annular flow regime .....	82
Figure 46: Performance comparison for 10 mm lift-tube at 0.7 submergence ratio .....	83
Figure 47: Performance comparison for 14 mm lift-tube at 0.7 submergence ratio .....	84
Figure 48: Performance comparison for 10 mm lift-tube at 0.5 submergence ratio .....	85
Figure 49: Performance comparison for 14 mm lift-tube at 0.5 submergence ratio .....	86
Figure 50: Performance comparison for the submergence ratio of 0.3.....	88
Figure 51: Performance comparison for the submergence ratio of 0.4.....	88
Figure 52: Performance comparison for the submergence ratio of 0.5.....	89
Figure 53: Bubble pump with multiple lift-tube (a) 2 lift-tubes (b) 3 lift-tubes .....	93
Figure 54: Symmetry of the multiple lift-tube in the experimental configuration.....	94
Figure 55: Variable pumping phenomenon in 2 lift-tubes .....	95
Figure 56: Variable pumping phenomenon in 3 lift-tubes .....	95
Figure 57: Slug flow regime in 2 lift-tube configuration at different time intervals .....	96
Figure 58: Slug flow regime in 3 lift-tube configuration at different time intervals .....	97

Figure 59: Churn flow regime in (a) 2 lift-tubes (b) 3 lift-tubes.....	98
Figure 60: Influence of lift-tube quantity at submergence ratio of 0.7 .....	98
Figure 61: Influence of lift-tube quantity at submergence ratio of 0.5 .....	99
Figure 62: Influence of lift-tube quantity at submergence ratio of 0.3 .....	99
Figure 63: Comparison between experiment and model for 2 lift-tube bubble pump ..	102
Figure 64: Comparison between experiment and model for 3 lift-tube bubble pump ..	103
Figure 65: Schematic diagram of a typical artificial neural network.....	105
Figure 66: Determination of the number of neurons in the hidden layer.....	108
Figure 67: MSE versus epoch with 4-24-1 network configuration.....	109
Figure 68: Predicted values from ANN model versus experimental values for all the data sets .....	110
Figure 69: Predicted values of unseen data from ANN model versus experimental values for 2 lift-tubes .....	111
Figure 70: Predicted values of unseen data from ANN model versus experimental values for 3 lift-tubes .....	112
Figure 71: Predicted values for 0.6 submergence ratio from ANN model versus experimental values for 2 lift-tubes.....	112
Figure 72: Predicted values for 0.6 submergence ratio from ANN model versus experimental values for 3 lift-tubes.....	113
Figure 73: Predicted values for 4 lift-tube airlift pump from ANN model.....	114
Figure 74: Comparison between the experimental results of Lin et al. (2016) and ANN predictions for 2 lift-tubes.....	115
Figure 75: Comparison between the experimental results of Lin et al. (2016) and ANN predictions for 3 lift-tubes.....	116
Figure 76: Modelling scheme .....	119
Figure 77: Influence of lift-tube quantity on pumping performance .....	120

Figure 78: Influence of lift-tube quantity on generator temperature.....	121
Figure 79: Influence of lift-tube quantity on cooling effect.....	122
Figure 80: Influence of lift-tube quantity on the performance of DAR system.....	123
Figure 81: Influence of the DAR system with single and multiple lift-tube on the output of the tri-generation system.....	124
Figure 82: Comparison between ANN predictions and Lin et al. (2016) experimental values.....	146
Figure 83: Comparison between experimental results of An et al. (2017) and Lin et al. (2016).....	147
Figure 84: Comparison between results of analytical model and experimental results of An et al. (2017) and Lin et al. (2016).....	148
Figure 85: Comparison between the experimental results of Lin et al. (2016) and ANN predictions for 2 lift-tubes.....	150
Figure 86: Comparison between the experimental results of Lin et al. (2016) and ANN predictions for 3 lift-tubes.....	150



# LIST OF TABLES

Table 1: Operating parameters for model comparison.....	40
Table 2: Comparison between the developed model and Ersoz (2015) model.....	40
Table 3: Input operating parameters for the analysis .....	41
Table 4: Input parameters for DAR model .....	49
Table 5: Superficial velocity of air for different flow regimes .....	69
Table 6: Flow regime specific values of distribution parameter and drift velocity .....	82
Table 7: Parameters for the heat-driven bubble pump model .....	87
Table 8: Percentage of airflow rate in each lift-tube.....	101
Table 9: Experimental configurations used for the design of the network .....	107
Table 10: Performance of ANN model for training, validation, testing and all data sets .....	110
Table 11: Input parameters for the analysis .....	119
Table 12: Estimated volumetric flow rate of vapour .....	145
Table 13: Estimated mass flow rate of vapour.....	149

# NOMENCLATURE

## *Latin symbols*

$A$	Cross sectional area ( $\text{m}^2$ )
$ANN$	Artificial neural network
$B$	Bore of the cylinder (m)
$b_j$	Bias associated with node in hidden or output layer
$CCP$	Combined cooling and power
$CFD$	Computational fluid dynamics
$COP$	Coefficient of performance
$CCHP$	Combined cooling, heating and power
$c_{pw}$	Specific heat of water ( $\text{J/kg.K}$ )
$c_{pex}$	Specific heat of exhaust gas ( $\text{J/kg.K}$ )
$C_o$	Distribution parameter
$D$	Lift-tube diameter
$DAR$	Diffusion absorption refrigeration
$Eff$	Effectiveness
$Exp$	Experiment
$f$	Circulation ratio
$f_{TP}$	Darcy friction factor
$\dot{f}_{TP}$	Fanning friction factor
$g$	Gravitational acceleration ( $\text{m/s}^2$ )
$GHX$	Gas heat exchanger
$h$	Specific enthalpy ( $\text{J/kg}$ )
$h^*$	Convection coefficient ( $\text{W/m}^2.\text{K}$ )
$h_{fg}$	Enthalpy of vaporisation ( $\text{J/kg}$ )
$H$	Liquid height in the lift-tube or reservoir (m)
$i$	Number of nodes
$ICE$	Internal combustion engine
$j$	Node in the hidden or output layer
$J$	Superficial velocity ( $\text{m/s}$ )

$J^*$	Total superficial velocity of liquid and gas mixture (m/s)
$k$	Thermal conductivity (W/m.K)
$L$	Lift-tube length (m)
$L_c$	Characteristic length of the evaporator tube (m)
$L_s$	Stroke of the cylinder (kg/m <sup>3</sup> )
$MSE$	Mean square error
$\bar{M}$	Molar mass (g/mol)
$\dot{m}$	Mass flow rate (kg/s)
$n$	Number of data points
$N$	Engine speed (rev/min)
$Nu$	Nusselt number
$P$	Pressure (Pa)
$Pr$	Prandtl number
$\dot{Q}$	Heat transfer (W)
$Ra$	Rayleigh number
$Re_{TP}$	Two-phase Reynolds number
$R^2$	Coefficient of determination
$S$	Generator height (m)
$sfc$	Specific fuel consumption
$SR$	Submergence ratio
$SHX$	Solution heat exchanger
$S_i$	Net input to node
$T$	Temperature (°C)
$T_c$	Thermocouple
$To$	Torque (N.m)
$\nu$	Kinematic viscosity
$V$	Velocity (m/s)
$Vo$	Volume (m <sup>3</sup> )
$V_d$	Volume displaced in the cylinder (m <sup>3</sup> )
$V_{vj}$	Drift velocity (m/s)
$\dot{V}$	Volume flow rate (m <sup>3</sup> /s)
$W$	Weight (kg)

$\dot{W}$	Engine shaft power output (W)
$w_{ij}$	Strength of the weight connection between nodes
$x$	Refrigerant mass fraction in the liquid phase
$X$	Fluid quality
$x_i$	Input to node in the hidden or output layer
$y$	Refrigerant mass fraction in the vapour phase
$Y$	Value
$Z_0$	Level of the reservoir exit (m)
$Z_{sys}$	Height of the liquid in the reservoir (m)

### *Subscripts*

0, 1, 2, 3...	Location points
<i>a</i>	Air
<i>abs</i>	Absorber
<i>amb</i>	Ambient
<i>bp</i>	Bubble pump
<i>con</i>	Condenser
<i>ct</i>	Connector
<i>evp</i>	Evaporator
<i>evpi</i>	Evaporator inlet
<i>evpo</i>	Evaporator outlet
<i>ex</i>	Exhaust
<i>exi</i>	Exhaust inlet
<i>exo</i>	Exhaust outlet
<i>Exp</i>	Experimental
<i>f</i>	Fuel
<i>fm</i>	Film
<i>gen</i>	Generator
<i>G</i>	Gas
<i>GHX</i>	Gas heat exchanger
<i>h</i>	Homogenous

$hx$	Heat exchanger
$hxi$	Heat exchanger inlet
$hxo$	Heat exchanger outlet
$i$	Inert
$l$	Liquid
$part$	Partial
$Pred$	Predicted
$r$	Refrigerant
$rec$	Rectifier
$sys$	System
$SHX$	Solution heat exchanger
$T$	Total
$TP$	Two-phase
$v$	Vapour
$w$	Water

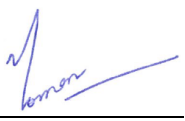
### *Greek symbols*

$\beta$	Coefficient of volume expansion
$\varepsilon$	Void fraction
$\varepsilon_h$	Homogenous void fraction
$\varepsilon_R$	Surface roughness
$\mu$	Viscosity
$\mu_{TP}$	Two-phase viscosity
$\eta_v$	Volumetric efficiency
$\rho$	Density (kg/m <sup>3</sup> )
$\rho_h$	Homogenous density

# ATTESTATION OF AUTHORSHIP

I hereby declare that this submission is my own work and that, to the best of my knowledge and belief, it contains no materials previously published or written by another person (except where explicitly defined in the acknowledgements), nor material which to a substantial extent has been submitted for the award of any other degree or diploma of a university or other institution of higher learning.

Auckland

Signature 

# Chapter 1: Introduction

## 1.1 Overview

Energy has always been an integral part in the daily life of the human being. It is an essential component for the development of the industrial, commercial, domestic, and transportation sectors of society. Due to rapid growth in these sectors, there has been an increase in the demand for energy throughout the world, as shown in Figure 1.

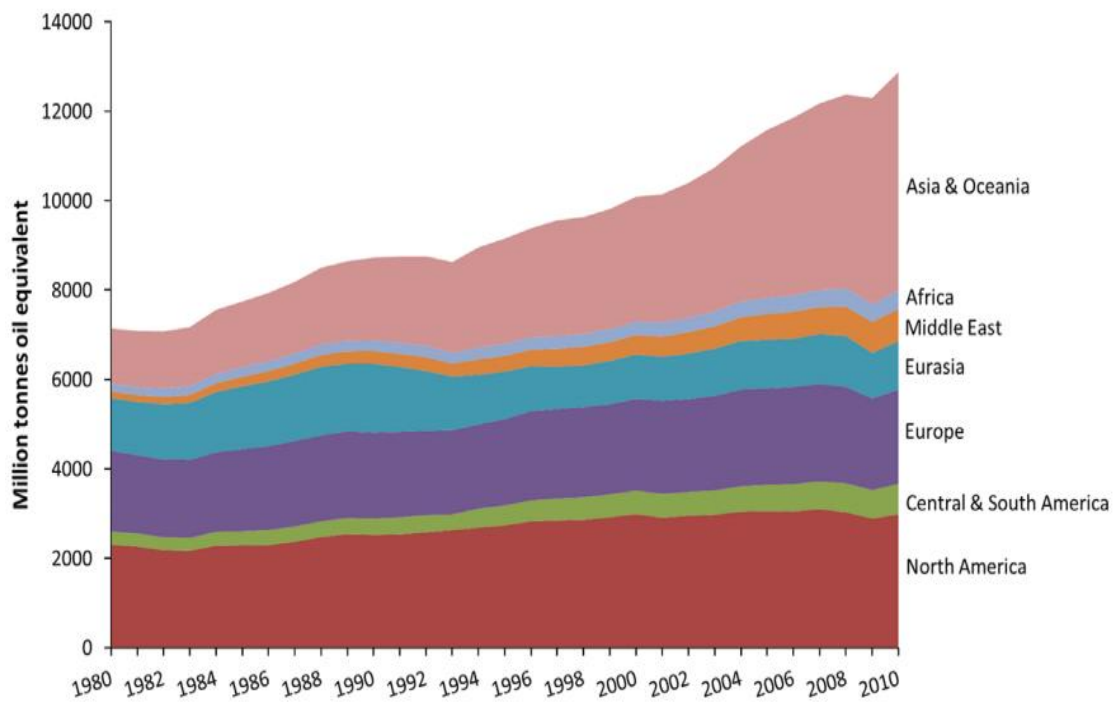


**Figure 1:** Primary energy consumption by region (Jradi and Riffat, 2014)

In the domestic sector, the demand for energy is mostly in the form of electric power, heating, and cooling. According to different surveys highlighting the consumption of energy, the domestic sector consumes 25% of the energy generated in the UK (Wang et al., 2011), while in the USA residential and commercial consumed about 40% of all

primary energy produced in 2013 (Ratner and Glover, 2014). In New Zealand, space heating, hot water, and refrigeration consume around 73% of the total household energy (Isaacs et al., 2010).

Household energy demands are typically met by grid electricity, which is generated by burning fossil fuels, nuclear energy, hydro energy, and renewable energy. However, a large percentage of grid electricity is produced by non-renewable energy sources. Therefore, in order to minimize the dependence on conventional energy sources such as coal and natural gas, a considerable amount of research has been directed towards utilising renewable energy sources (Hussain et al., 2017). In spite of positive developments in the field of renewable energy, still there is strong dependence on conventional fossil fuels as shown in Figure 2.

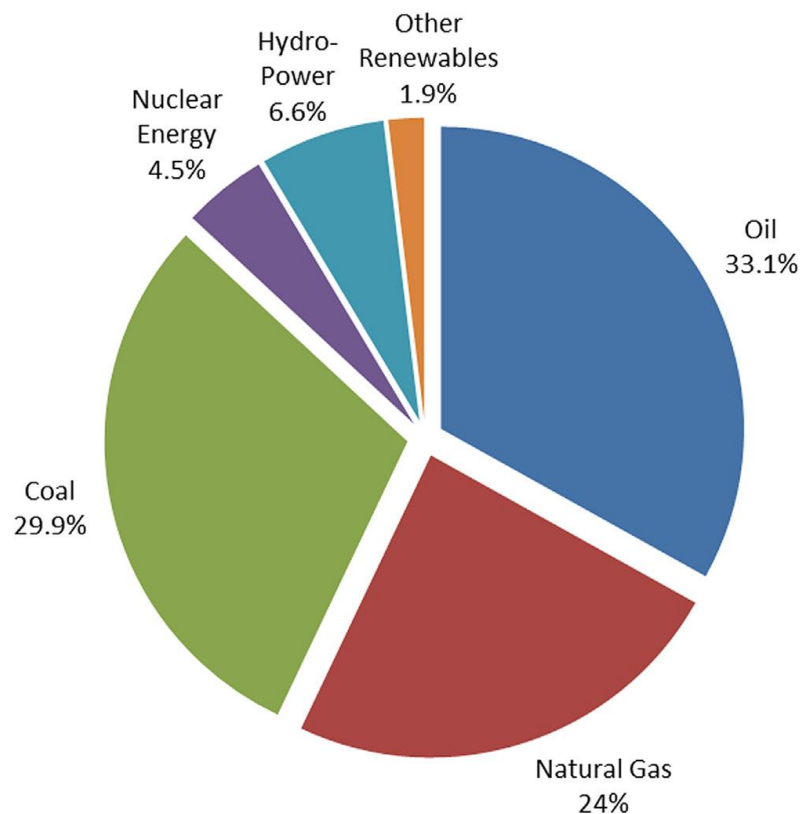


**Figure 2:** Global energy consumption by fuel (Jradi and Riffat, 2014)



Now, due to an increase in world population and industrial growth, the consumption of fossil fuels has resulted in the depletion of these resources. As a result, the past few years have witnessed a significant increase in the price of these fuels. At the same time, the amount of CO<sub>2</sub> and other gases released due to the burning of fossil fuels has raised concerns from many sectors. Furthermore, there has been a growing effort to reduce the energy dependence of countries, which are rich in fossil fuel resources (Chicco and Mancarella, 2007).

## **1.2 Waste heat**

In order to fulfil the energy demand, all thermally driven power systems reject heat as a consequence of nature, which is bound by the second law of thermodynamics. The heat rejected is generally exhausted to the atmosphere without any attempt to utilise it, since the heat released is not being utilised, it is often termed ‘Waste Heat’. It is estimated that two-thirds of the input energy for electricity generation in the USA is ‘wasted’ as heat during the energy conversion process (Rattner and Garimella, 2011).

The temperature of the waste heat determines the quality of this energy, though there is no universally agreed limit for defining the grade of waste heat. That said high-grade waste heat has been categorised as having temperatures higher than 649 °C, medium-grade waste heat as that between 650 °C to 232 °C and low-grade waste heat as that below 232 °C (Johnson et al., 2008).

There are different sources that contribute in wasting the heat, such as internal combustion engines (ICE) of vehicles, power plants, and industrial units. In ICE, this waste heat energy is in the high temperature exhaust gas, cooling water, and residual

heat from the engine surface to the atmosphere. While in power plants and industries, large quantities of waste heat are rejected to the environment by means of hot exhaust gases, cooling media, and heat loss from hot equipment surfaces (Miro et al., 2016).

In order to better utilise fuel resources, the design and development of energy utilisation systems needs to be improved. As such, the utilisation of waste heat is one of the solutions to improving energy usage. In achieving this there are two approaches to make use of waste heat energy: Co-generation and Tri-generation as shown in Figure 3.

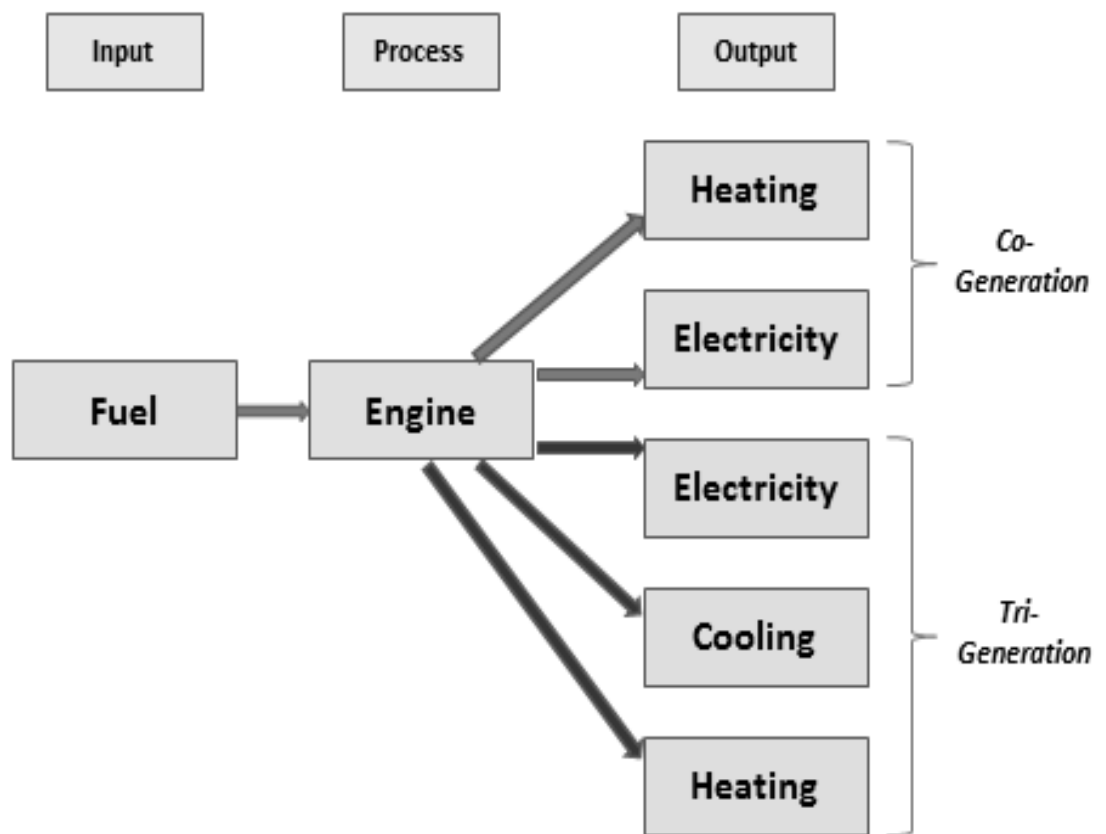


**Figure 3:** Approaches for utilisation of waste heat energy

### **1.3 Co-generation**

Co-generation also termed as CHP (combined heat and power) is the simultaneous generation of electricity and heat. The heating load is satisfied by utilising the waste heat produced from the electricity generation process. Since, two forms of energy are produced in the co-generation process; they provide substantial energy savings relative to conventional separate electric and thermal energy technologies (Raj et al., 2011). Depending upon the co-generation combinations, the typical components of co-generation system may include ICE, gas turbines, steam turbines, heat exchangers, electricity generators, cooling towers, and other components.

Both the electrical and thermal energy produced by the co-generation process can be used onsite or distributed to other facilities (Raj et al., 2011). Although co-generation provides several benefits; however, there application is constrained due to high cost and limited utilisation of the waste heat, especially for the space cooling applications (Gelegenis and Mavrotas, 2017).

### **1.4 Tri-generation**

In order to manage the demand of cooling and to increase the efficiency of primary energy input, the concept of tri-generation or combined cooling, heating and power (CCHP) was developed. Tri-generation involves the production of electricity, heat, and cold in one operation. In CCHP or tri-generation, the thermal energy of exhaust gases is utilised to run thermally activated cooling systems in addition to meeting a heating load (Stojkov et al., 2011). This type of system is characterised by electrical power generation of a few kilowatts to megawatts.

A tri-generation system may be operated in two modes, namely ‘separate’ and ‘simultaneous’ (Angrisani et al., 2012). In the separate mode, the system provides electricity continuously, whereas heating and cooling is provided during the seasonal demand period. In the simultaneous mode, the system satisfies cooling and heating load, as well as the electrical load, which makes them convenient to meet industrial and residential sector.

The important advantages of the tri-generation are higher fuel efficiency, low emissions of CO<sub>2</sub> and other waste gases, and most importantly, the benefit of having three useful outputs. It is estimated that around 10% of economic savings can be achieved by tri-generation system as compared to co-generation system (Hernandez-Santoyo and Sanchez-Cifuentes, 2003).

#### **1.4.1 Components of tri-generation systems**

A tri-generation system consists of a prime mover, an electricity generator, a heat recovery system, cooling equipment, and a control system. Different types of prime movers are used such as ICE, small gas turbines, Stirling engines, and fuel cell systems (Moussawi et al., 2016). Similarly, different types of refrigeration technologies can be integrated into the tri-generation system. These include both alternative thermally activated technologies and traditional vapour compression technology. Some of the main alternative refrigeration technologies that can be integrated into a tri-generation system are absorption cooling, adsorption cooling, desiccant cooling, and ejector cooling (Jradi and Riffat, 2014).

### 1.4.2 ICE based tri-generation system

Due to higher efficiencies relative to cost, the ICE is most commonly used as the prime mover in tri-generation systems (Sonar et al., 2014). As illustrated in Figure 4, the shaft work from the engine drives an electrical generator for producing electricity. The exhaust gases from the engine are used to supply heat to the hot water cycle and drive the thermally activated cooling system.

Traditional vapour compression refrigeration technology can also be integrated into an ICE based tri-generation system, though this is at the expense of shaft power. As such, thermally activated cooling systems, utilising the waste heat are often used to produce cooling (Deng et al., 2011). In remote communities where stationary ICE is used for the generation of electrical power, the exhaust waste heat from such stationary ICE can be utilised to run a tri-generation system.

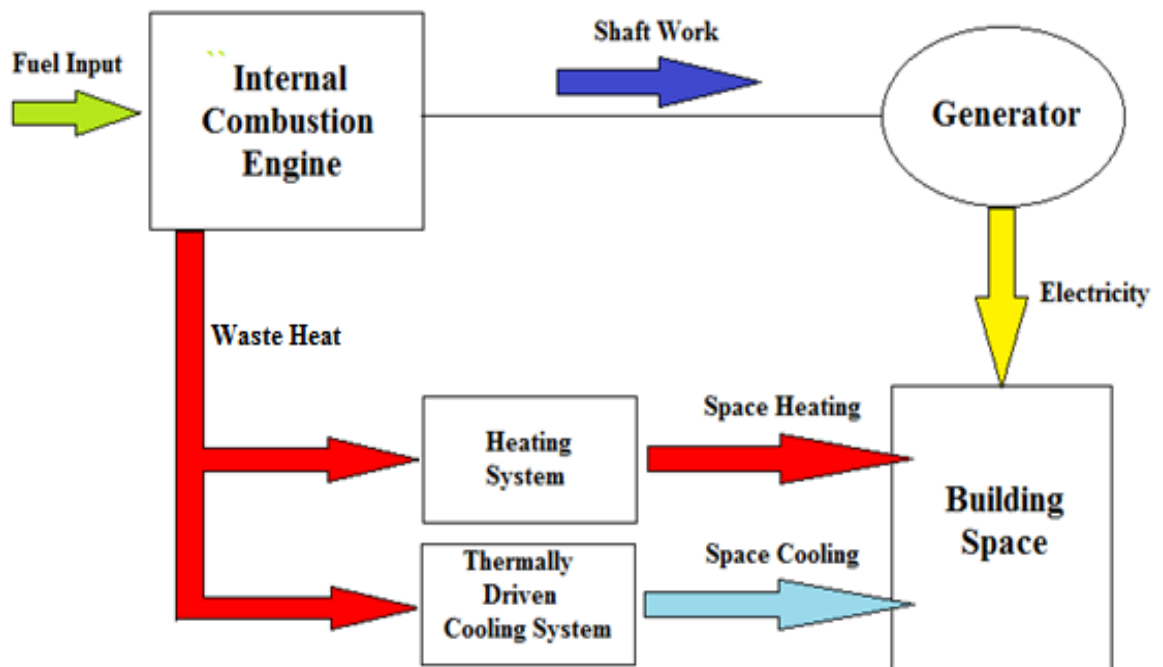


**Figure 4:** Schematic diagram of an ICE based tri-generation system

### **1.4.3 Decentralised tri-generation system**

To effectively use the fuel in the domestic sector, a considerable amount of research has started focussing towards decentralised tri-generation systems. In this type of tri-generation system, all the three forms of energy, i.e. electrical power, heating, and cooling are produced onsite close to the end user. As such, there has been an increasing interest with numerous studies and projects on small-scale tri-generation systems suitable for households where no central power exists (Lin et al. 2007, Sonar et al. 2014).

Since these systems are located near the end user, costly transmission lines can be avoided that account for considerable cost and energy loss. These systems are characterised by delivering electrical power of less than 15 kW (Sonar et al., 2014) and are termed as Micro Tri-generation (m-tri) (Lin et al., 2007). Due to the commercial availability of ICE's over a very large size range, it makes them convenient to be used as the prime mover in small-scale tri-generation systems.

### **1.4.4 Studies on decentralised tri-generation systems**

Numerous studies have been performed to effectively use the ICE as a prime mover in a small-scale tri-generation system. Miguez et al. (2004) studied the feasibility of a domestic CHP system with a heat pump. The system consisted of a 9.6 kW water-cooled Honda gas engine, an electric generator, and a heat recovery system. Simultaneously the engine drives a heat pump, which is reversible and meets the summer refrigeration load and winter thermal load. It was found that in single generation when only electricity is generated, the amount of heat rejected reaches up to

80% of the total energy consumption. In co-generation, they found that heat recovery at high engine speed leads to slightly higher COP at the same electric output. In the case of tri-generation, they showed an increase in overall efficiency of the system and concluded that the role of the heat pump is crucial for the enhancement of a system's overall efficiency.

Lin et al. (2007) performed their study on a household-size micro tri-generation system. The experimental setup consisted of a 9.5 kW air-cooled diesel generator, a heat exchanger for heat recovery, and an absorption refrigerator, which was driven by waste heat. They concluded that it is feasible to run the system in tri-generation mode when the engine load is greater than 50% and the exhaust temperature is greater than 200 °C. At low load, the temperature of the exhaust gas is too low to activate the cooling system. Under different load conditions, the total thermal efficiencies of tri-generation are from 205% to 438% higher than that of single generation.

In order to utilise a low temperature heat source, Godefroy et al. (2007) performed their design and analysis on a tri-generation system with a 5.5 kW gas engine and an ejector cooling system. They found that by using some of the electrical production for the cooling cycle boosts the cooling capacity, however; it does not improve the overall efficiency of the system as the gain in the cooling capacity is balanced by a loss in the net electrical output.

Huangfu et al. (2007) studied the performance of a micro-scale combined cooling heating and power (MCCHP) system. The system consisted of a 12 kW reciprocating ICE generator set and an adsorption chiller. They concluded that the performance of the system improves as the load is increased greater than half load.

Khatri et al. (2010) investigated the performance of a compression ignition (CI) engine driving a micro tri-generation system. A 3.7 kW water-cooled diesel engine generator set was used to perform the experiments. They found that at full load the useful energy output from the tri-generation was 158.69% greater than that of a single generation system.

In order to develop further understanding of the operational characteristics of small-scale ICE based tri-generation systems, Goyal et al. (2015) investigated the feasibility of a 3.7 kW capacity agricultural diesel engine based tri-generation system. Four units of commercially available Electrolux absorption system, each with a capacity of 51 litres were used for space cooling. They concluded that the performance of the engine generator is not affected by running the system in tri-generation mode. In addition, the tri-generation mode results in low specific fuel consumption as compared to single generation.

Cacua et al. (2016) studied the feasibility of diesel-biogas as an alternative energy source for their micro-trigeneration system. The system consists of a 14.8 kW compression ignition engine, vapour absorption refrigerator for space cooling, and a counter flow heat exchanger for heating and drying purposes. They concluded that by using diesel-biogas as an energy source, the exhaust gas temperature of the engine increases. As such, the temperature of the cooling system drops faster with the same refrigeration load as compared to using conventional diesel as an energy source.

From the studies performed on small-scale tri-generation system it can be seen that most of the studies were based on utilising commercially available equipment, where the researchers combined different configurations of the equipment to study the



performance of a small-scale tri-generation system. All studies have shown the effectiveness of tri-generation. However, most of the researchers (Goyal et al. 2015, Khatri et al. 2010, Huangfu et al. 2007, Lin et al. 2007) in their studies have reported the results for engine operating at half to full load conditions, suggesting that at low engine load, the performance of the small-scale tri-generation system may not be feasible. Lin et al. (2007) mentioned that the temperature of the exhaust gas should be higher than 200 °C for the cooling system to activate. In addition, Cacua et al. (2016) mentioned a very interesting point in their study that the best refrigeration output was achieved when the temperature of the engine exhaust gas is higher.

## **1.5 Research Question**

The literature suggests that the probable factors influencing the performance of an ICE based tri-generation system are engine load, exhaust gas temperature, and cooling system. It was found that the activation of the cooling system depends upon the temperature of the exhaust gas, which varies with engine load. At certain engine load conditions, the cooling system was unable to activate, thus limiting the performance of a small-scale ICE based tri-generation systems. This suggests that there is an opportunity for improving the performance of the small-scale ICE based tri-generation system. In addressing this, the central question for this work is:

*How can the performance of a small-scale ICE based tri-generation system be improved?*

## **Chapter 2: Preliminary experimental investigation**

From the literature review, it was found that several factors affect the performance of a small-scale ICE based tri-generation system, this presents several challenges in designing an efficient ICE based tri-generation system. To understand this, it was decided to perform a preliminary experimental investigation of an ICE based tri-generation system. This will provide useful insights in understanding the behaviour of the tri-generation system and identify the areas that need more detailed investigation.

### **2.1 Selection of tri-generation components**

In designing an ICE based tri-generation system, an appropriate ICE and refrigeration technology were selected for this study.

#### **2.1.1 Selection of an ICE**

ICE are available in two types, which are spark ignition engine and compression ignition engine. Spark ignition engines are mostly fuelled by gasoline, whereas compression ignition engines are operated by using diesel as fuel. Wang et al. 2014 suggests that for exhaust energy recovery systems diesel engines provides better economical applicability in terms of cost effectiveness and payback period. As such, it was decided to use a diesel engine for this study.

The engine selected for this study was a 5.2 kW Robin DY41 4-stroke, overhead valve, air-cooled single cylinder stationary diesel engine. It was selected as its size makes it a possible prime mover for any micro tri-generation system.

### 2.1.2 Selection of refrigeration technology

As mentioned in Chapter 1, thermally activated cooling methods are commonly used for producing cooling, in which absorption cooling systems as shown in Figure 5 are dominant (Deng et al., 2011).

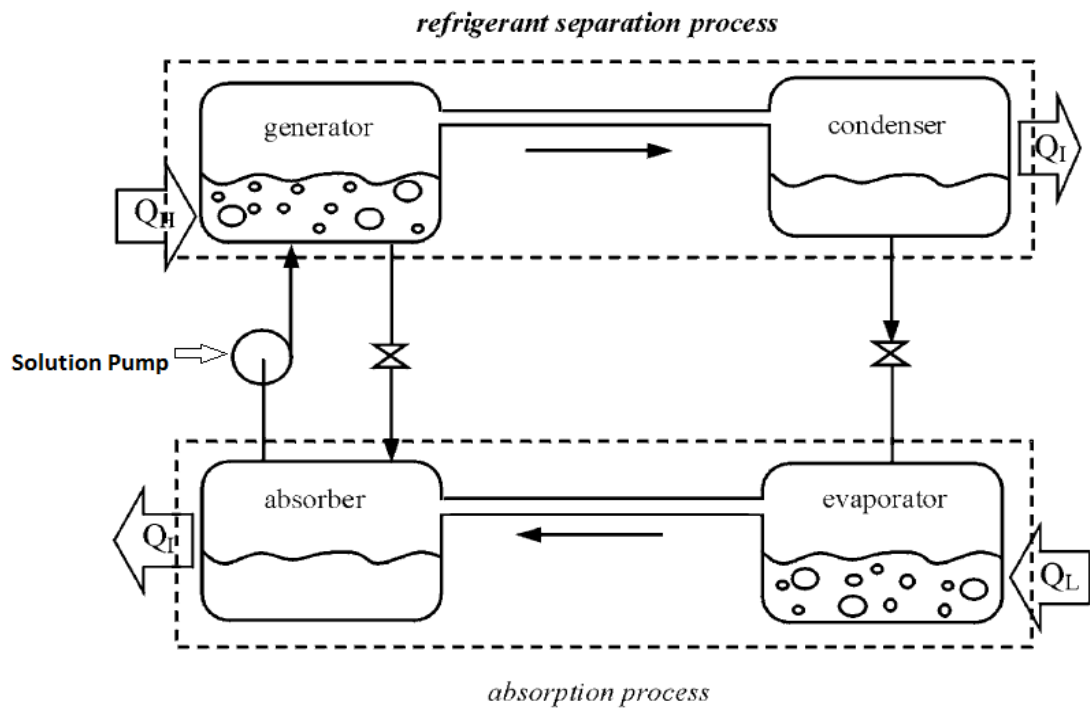


**Figure 5:** Absorption cooling system (Srikhirin and Aphornratna, 2002)

A typical absorption cooling system consists of four main components: Generator, Condenser, Evaporator, and Absorber. Two different working fluids are used in the absorption cooling system: a refrigerant and an absorbent. Heat is applied to the generator, which contains the solution of the refrigerant and the absorbent. The addition of the heat generates refrigerant vapour, which separates it from the solution and the refrigerant flows to the condenser. In the condenser, the vapour refrigerant is condensed to liquid phase and flows to the evaporator via an expansion valve where it absorbs heat energy and generates cooling effect. The refrigerant vapour leaves the evaporator and

enters the absorber where it is absorbed by the absorbent. Using a solution pump the solution of the refrigerant and absorbent is pumped to the generator to restart the cycle.

However, the use of the solution pump in the absorption technology, shown as electricity usage in Figure 6, makes these cooling systems dependant on power other than waste heat.

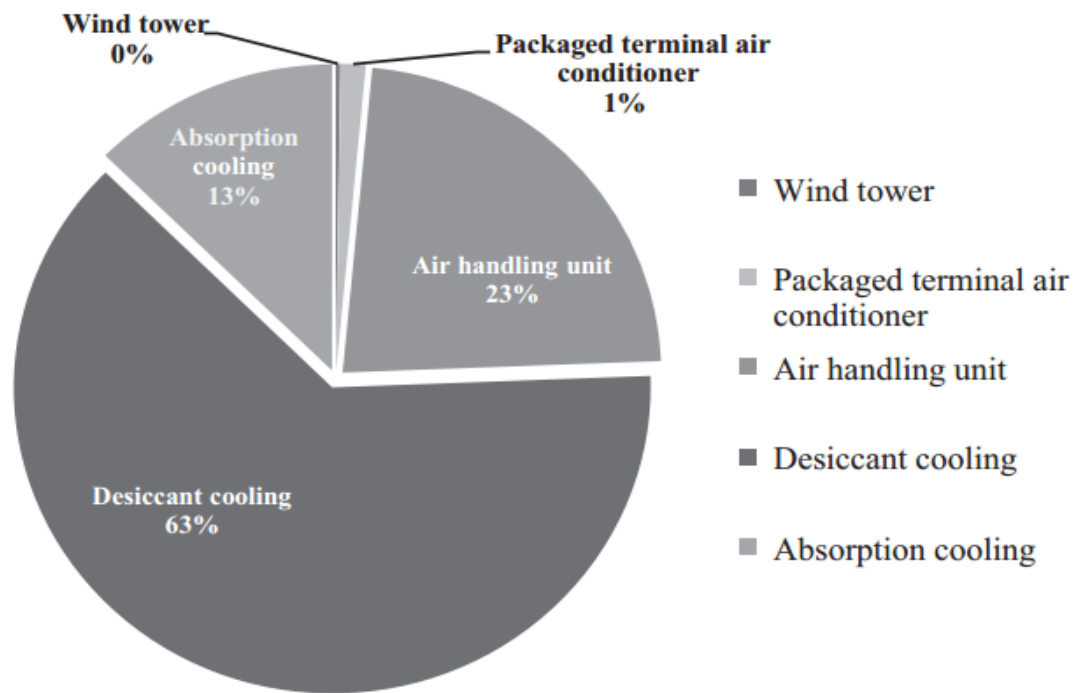


**Figure 6:** Electricity utilisation for alternative cooling technology (Hughes et al., 2011)

Therefore, diffusion absorption refrigeration (DAR) (Von Platen and Munters, 1928), a cooling system that does not require any work input from an external source was chosen as the basis of this preliminary investigation. The DAR system works on the same principle, as an absorption cooling system, but does not require any external work input.

Figure 7 shows the schematic of a typical DAR system. The difference between a conventional absorption cooling system and DAR system is that instead of a solution pump, the DAR cycle utilises a heat driven bubble pump to circulate the working fluid. In addition to a refrigerant and an absorbent as the working fluids, the DAR system consists of an inert gas for maintaining the total pressure in the system.

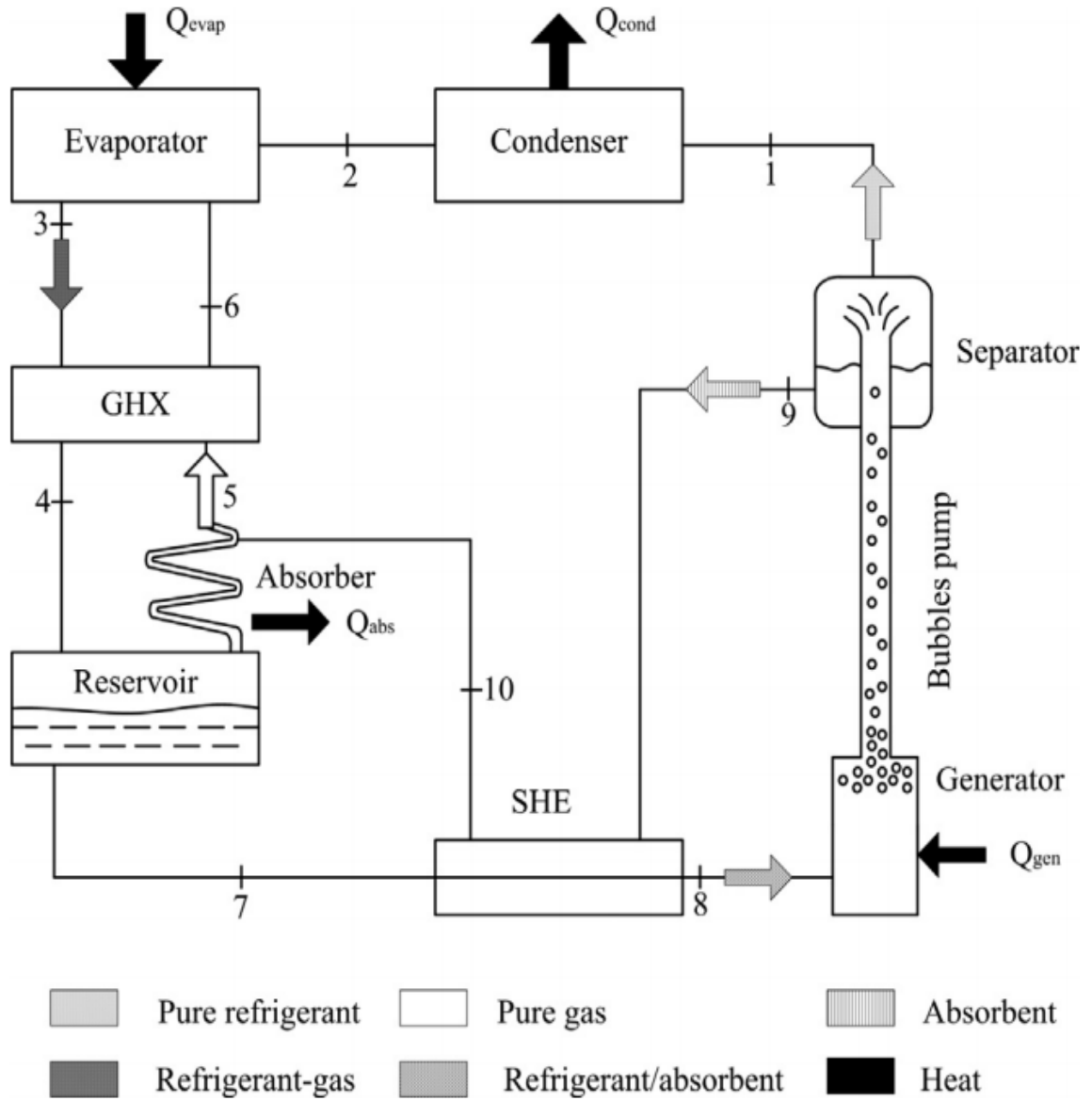


**Figure 7:** Diffusion absorption refrigeration system (Rodriguez-Munoz and Belman-Flores, 2014)

## 2.2 Experimental method

After selecting the necessary components, a small tri-generation system was developed using a stationary diesel engine coupled to an exhaust gas heat exchanger and a small DAR system (GLACIER, 2014).

Figure 8 shows the schematic layout of the experimental setup. The system consisted of a test bed with diesel engine coupled to hydraulic brake dynamometer, exhaust heat-driven DAR system, heat exchanger for hot water, and control system.

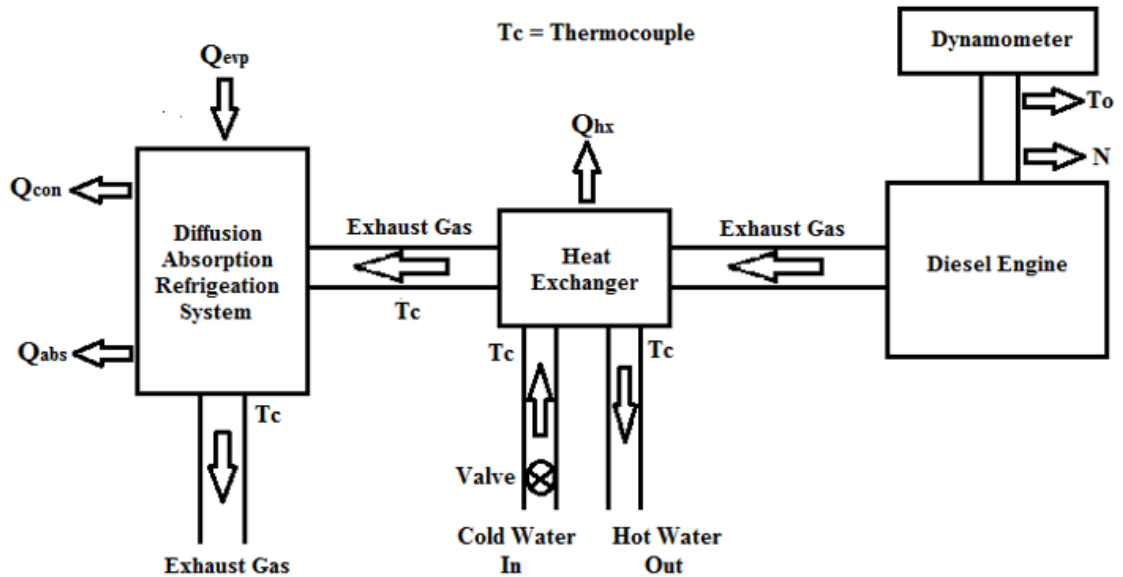


**Figure 8:** Schematic of the experimental tri-generation setup

The engine was coupled to a Go-Power Systems water brake dynamometer that was used to vary the shaft load on the engine, thus acting in the same manner as an electric generator. The generator of the DAR system was modified to capture the waste heat of the exhaust gases. For this purpose, a co-current heat exchanger was fabricated such that the exhaust gas entered at the bottom of the generator and flowed up exiting from the top of the generator.

To complete the tri-generation objective, another heat exchanger was fabricated in order to capture the waste heat from the exhaust gases to produce hot water. The heat exchanger built was a tube-in-tube counter-flow type and made of stainless steel with baffles to direct the flow. The heat exchanger was placed before the DAR system in order to control the temperature of the exhaust gas going into the DAR system. All piping was insulated to minimise the heat loss and gain.

For this study, it was decided to run the system in combined cooling and power (CCP) and combined cooling, heating, and power (CCHP) modes. In CCP mode, the water heater was deactivated and the exhaust gas was delivered to the DAR system directly. As such, the exhaust gas entered the generator of the DAR system where it transferred its energy to the working fluid of the refrigeration cycle. The exhaust gas then exited the DAR system and was released into the environment. In CCHP mode, the water heater was activated such that the exhaust gas transferred some part of its energy to the cold water, thus generating hot water. After exiting the water heater, the exhaust gas passed through the generator of the DAR system to activate the refrigerating system and then released to the atmosphere.

The rate of heat transferred from the exhaust gas in the water heat exchanger was determined by measuring the flow rate of the water in the heat exchanger and its change in temperature measured using T-type thermocouples at the inlet and outlet of the heat exchanger. In order to assess the performance of the cooling system, the temperatures at various points of the DAR system were measured. T-type thermocouples were mounted on the inlet and outlet of the evaporator ( $T_{evpi}$  and  $T_{evpo}$ ), the condenser ( $T_{con}$ ), the absorber ( $T_{abs}$ ), and the ambient conditions ( $T_{amb}$ ). Since J-type thermocouples are

more suitable for measuring high temperatures, therefore they were used to measure the temperature ( $T_{exi}$  and  $T_{exo}$ ) of the exhaust gas entering and leaving the generator of the DAR system. The measured exhaust temperatures determine the rate of heat transfer to the DAR system.

In undertaking testing in both CCP and CCHP modes, the load on the engine was varied to 0, 25, 50, 75, and 100 percent, while the speed of the engine varied between 1700 to 1900 rpm. Finally, the torque produced by the engine at a measured speed was recorded in order to determine the brake power produced by the engine. The sum of the refrigerating effect, water heating, and brake power gave the total output for the tri-generation system

## 2.3 Energy analysis

To evaluate the performance of the DAR system under the different operational modes, the refrigerating effect ( $\dot{Q}_{evp}$ ) produced by the DAR system was calculated using Equation 1 (Appendix A) :

$$\dot{Q}_{evp} = h^* A_{evp} \left[ \left( \frac{T_{evpi} + T_{evpo}}{2} \right) - T_{amb} \right] \quad (1)$$

Where  $h^*$  is the convection heat transfer coefficient on the evaporator,  $A_{evp}$  is the surface area of the evaporator,  $T_{evpi}$  and  $T_{evpo}$  are the inlet and outlet temperatures at the evaporator,  $T_{amb}$  is the ambient temperature. For the production of the hot water, the heat transfer rate from the exhaust gas to the water in the water heat exchanger can be evaluated using Equation 2:

$$\dot{Q}_w = \dot{m}_w c_{pw} (T_{hxo} - T_{hxi}) \quad (2)$$



Where  $\dot{Q}_w$  is the heat input to the water,  $\dot{m}_w$  is the mass flow rate of water,  $c_{pw}$  is the specific heat of water,  $T_{hxi}$  and  $T_{hxo}$  are the temperatures of water entering and leaving the heat exchanger.

## 2.4 Results and discussion

Having run the experiments on different operational modes, the following observations were made. In CCP mode, when the engine was run at idle and 25% load conditions and at a speed of 1700 rpm, it was observed that no refrigerating effect was produced by the DAR system. At an engine load and speed of 50% and 1900 rpm respectively, it was observed that as the temperature of the exhaust gas entering the DAR system exceeded 190 °C, the temperature at the evaporator dropped below the ambient and a steady cooling period was achieved as shown in Figure 9.

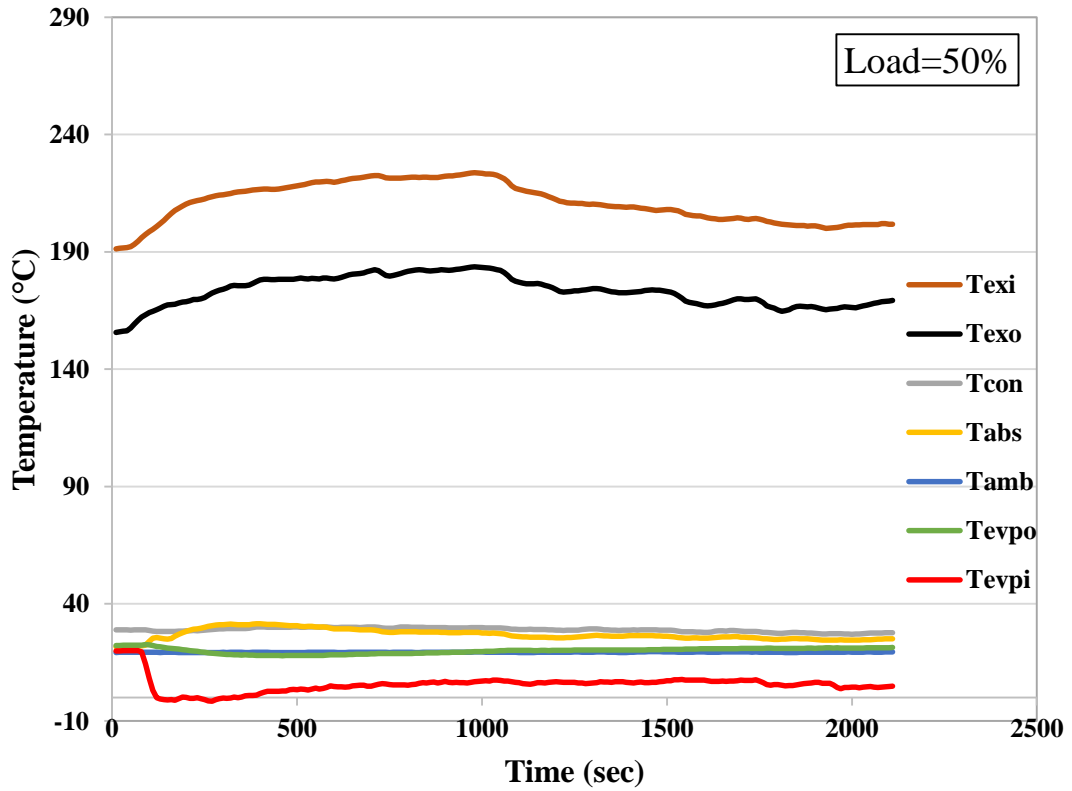


**Figure 9:** Temperature profile at 50% CCP mode

At 75% engine load and 1800 rpm engine speed, Figure 10 shows the temperatures recorded at different points of the experimental system. By increasing the load on the engine to 75%, a steady state period of cooling was again achieved (The minimum evaporator temperature recorded was 0 °C). At this load condition, the temperature of the exhaust gas entering the DAR system was between 200-240 °C.

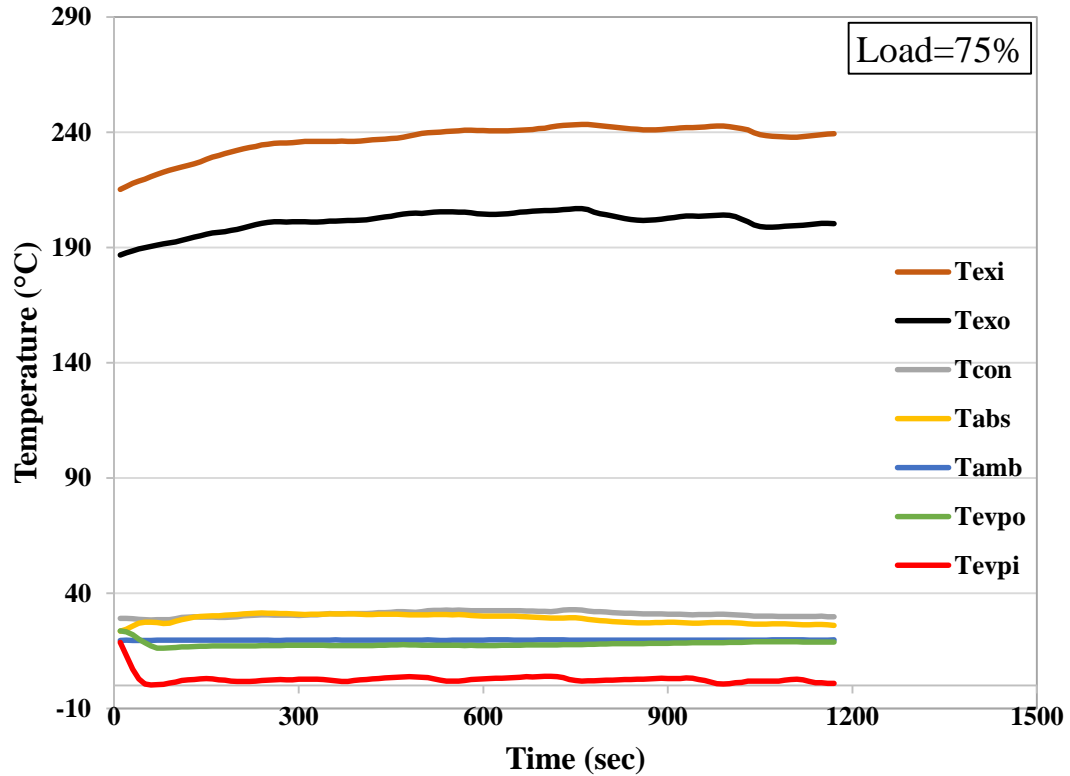


**Figure 10:** Temperature profile at 75% CCP mode

At 100% load conditions and 1800 rpm engine speed, it was observed that as the temperature of the exhaust gas increased beyond 300 °C no refrigerating effect was produced by the DAR system as shown in Figure 11. This result indicates an upper limit to the exhaust gas temperature on the operation of the DAR system. After running the experiments in CCP mode, experiments were performed by running the system on CCHP mode.

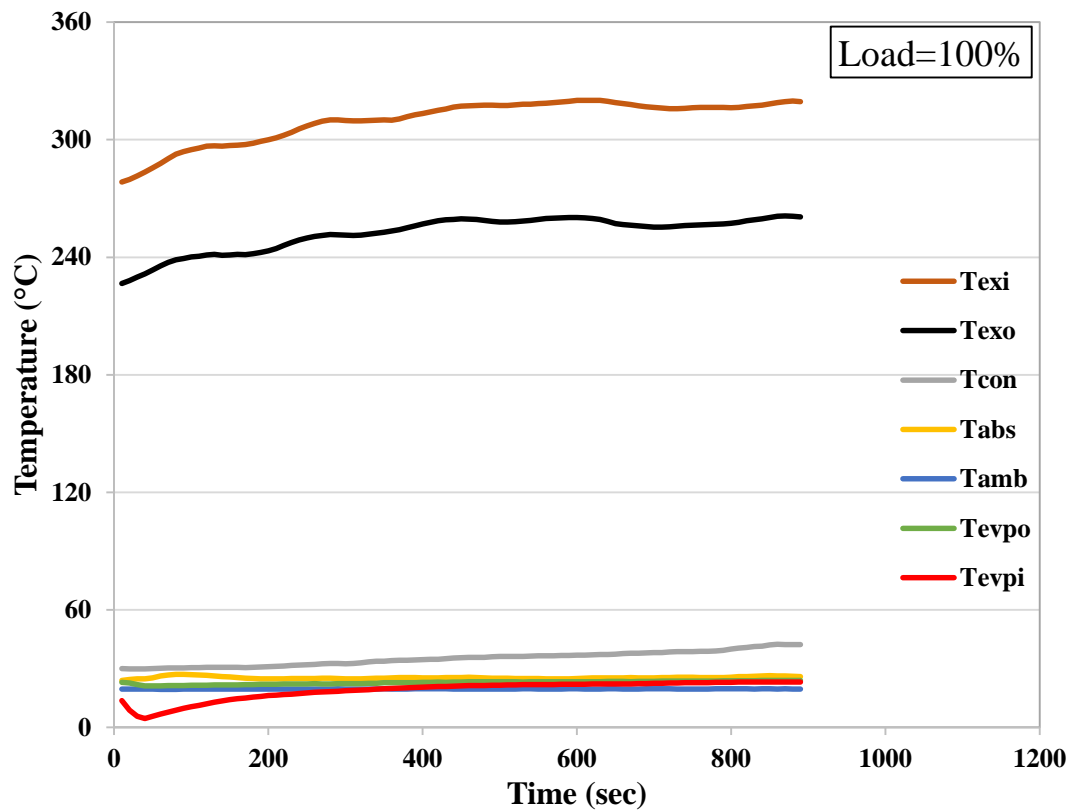


**Figure 11:** Temperature profile at 100% CCP mode

While running the system in CCHP mode, it was found that at idle, 25%, 50%, and 75% engine load, the DAR system was not able to produce any refrigerating effect. This was due to the low temperature of the exhaust gas leaving the water heat exchanger. The temperature of the exhaust gas entering the DAR system at these load conditions was less than 150 °C.

At 100% engine load and 1800 rpm engine speed, cooling was observed when the temperature of the exhaust gas leaving the water heat exchanger was between 180-190 °C as shown in Figure 12.

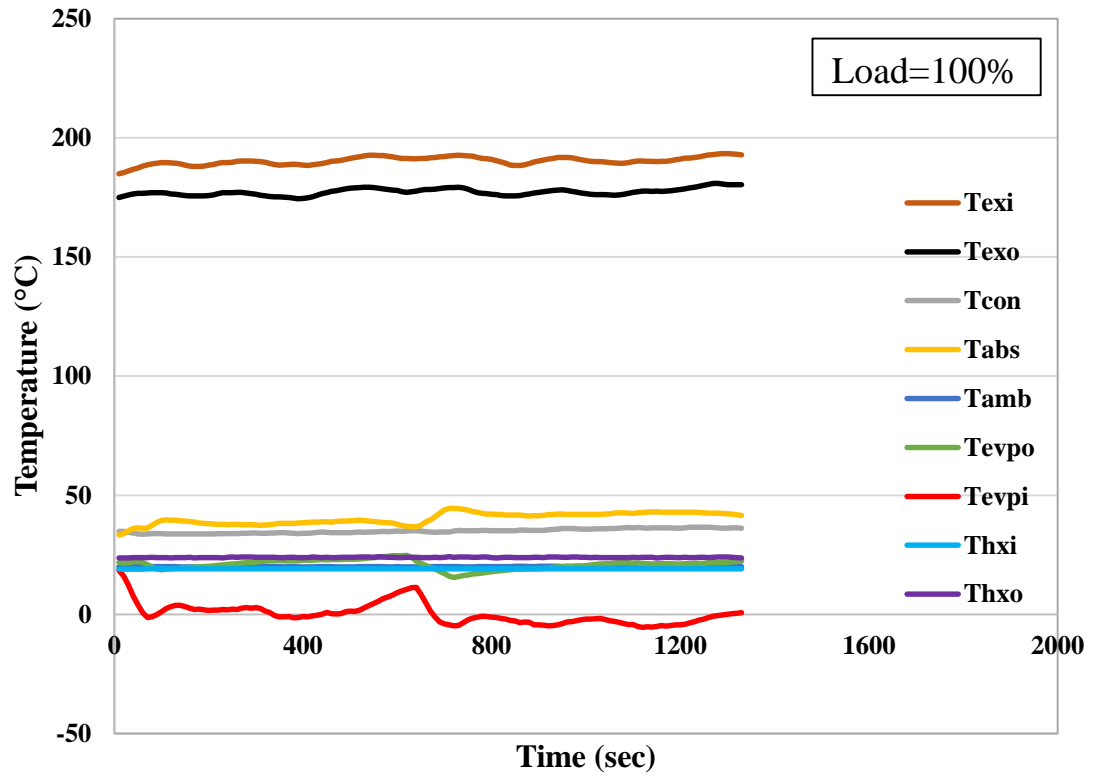


**Figure 12:** Temperature profile at 100% CCHP mode

After gathering the experimental results, the influence of the operational modes on the performance of the DAR system was evaluated as shown in Figure 13. The coefficient of performance (COP) of the DAR system was calculated using Equation 3:

$$COP = \frac{\dot{Q}_{evp}}{\dot{Q}_{gen}} \quad (3)$$

Where  $\dot{Q}_{evp}$  is the refrigerating effect and  $\dot{Q}_{gen}$  is the heat supplied to the DAR system. The maximum coefficient of performance was approximately 4% for the system operating in CCHP mode condition. For CCP mode, the performance at 75% engine load was better than other load conditions. Since the cooling effect produced by the DAR system at each operational mode was calculated using relationships based on natural convection, therefore the values of the COP obtained were low.

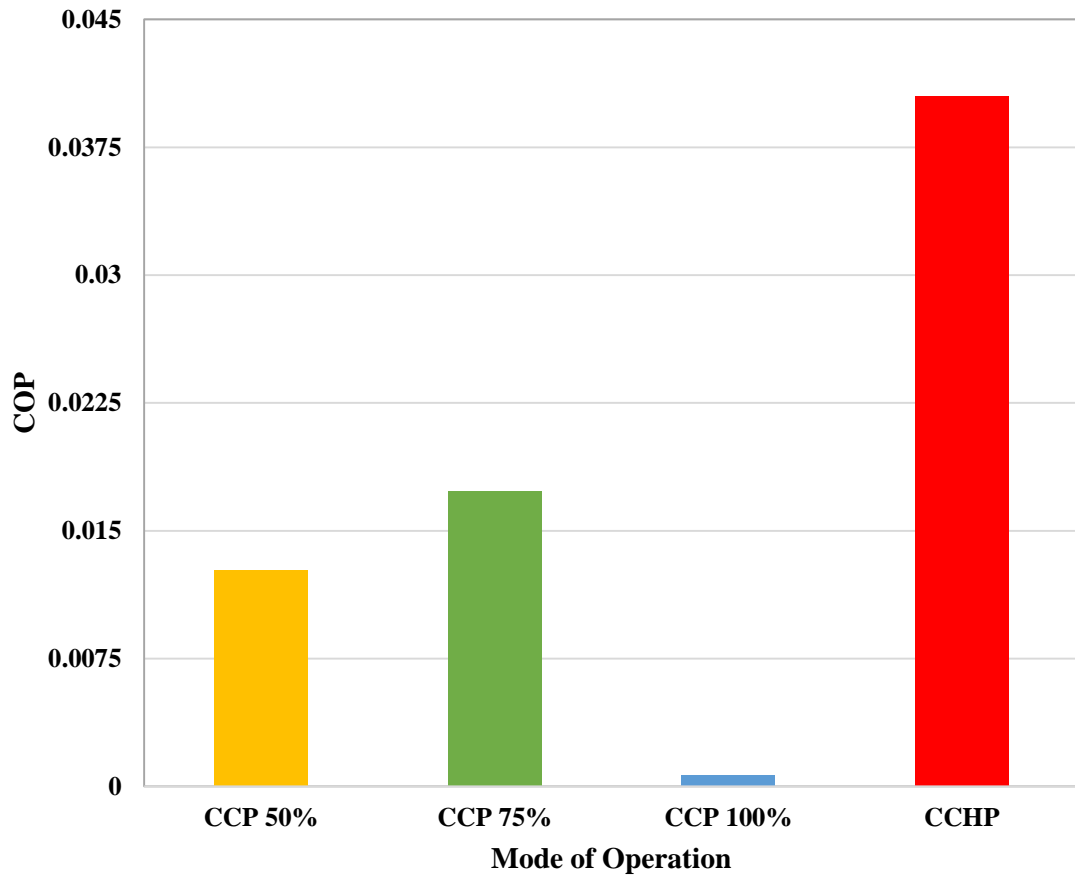


**Figure 13:** Performance of the DAR system at different operating modes

Furthermore, the useful output energy (consisting of the brake power, cooling, and heating for both CCP and CCHP mode) was also evaluated, as shown in Figure 14. It can be seen that during CCHP mode, the performance of the system was higher as compared to CCP modes. In the case of the CCHP mode since there is an additional output energy in form of hot water, therefore the amount of output energy captured is significantly more than in CCP mode.

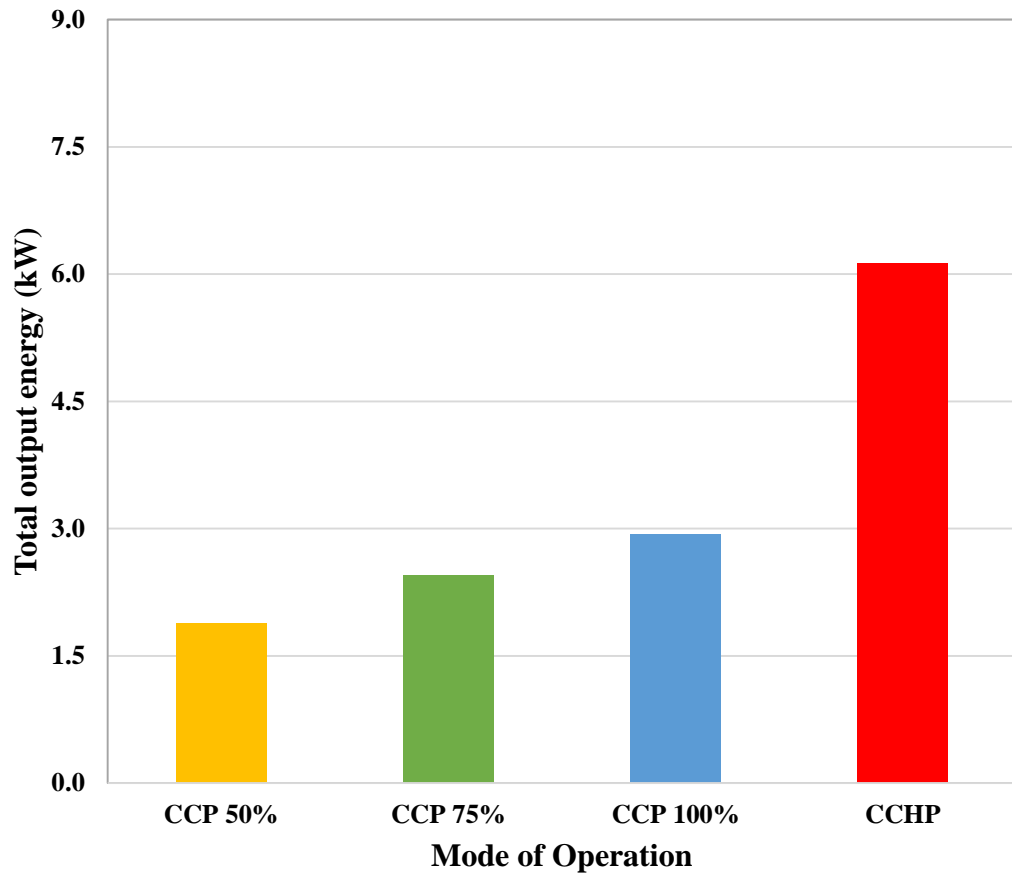


**Figure 14:** Useful output energy at different operating modes

## 2.5 Conclusion

From the preliminary investigation, it was possible to conclude that the exhaust waste heat from an ICE can be effectively utilised to run a tri-generation system. However, the performance of the ICE based tri-generation system was influenced by several factors such as engine load, exhaust gas temperature, and the refrigerating effect produced by the refrigeration system.

The fact that the temperature of the exhaust gas depends upon engine load, influences the activation of the cooling system and limits both the operating range and refrigerating

capacity of the DAR system. It was found that the DAR system would activate when the temperature of the exhaust gas entering the DAR system was between 180 °C to 240 °C.

This suggested that the performance of the ICE base tri-generation system could be improved by extending the operating range and increasing the refrigerating capacity of the DAR system. As such, it was decided to perform a detailed investigation on the operation of the DAR system and to understand the factors that influence its performance.

# **Chapter 3: Modelling the performance of a diffusion absorption refrigeration system**

## **3.1 Introduction**

In Chapter 2, it was shown that for an ICE based tri-generation system; the exhaust waste heat of an ICE could be used to activate a DAR system to provide cooling. However, it was found that the DAR system would activate when the temperature of the exhaust temperature was in the range of 180 °C to 240 °C.

This seems to limit both the operating range and the refrigerating capacity of the DAR systems. Hence, it affects the overall performance of the ICE based tri-generation system. Therefore, there is a need to better understand the factors that affect the performance of the DAR system for steady state operating conditions.

## **3.2 Working principle**

Before examining the influence of system components and operating parameters on the performance of the DAR system, it is important to understand the working principle of the DAR system. A typical DAR system shown in Figure 15 consists of a generator, bubble pump, rectifier, condenser, evaporator, absorber, gas heat exchanger (GHX) and solution heat exchanger (SHX). Typically, the working fluid consists of ammonia ( $\text{NH}_3$ ) as the refrigerant, water ( $\text{H}_2\text{O}$ ) as an absorbent and hydrogen ( $\text{H}_2$ ) as an inert gas used to maintain the total pressure in the system. As such, these fluids have been selected to explain the working of the DAR cycle.



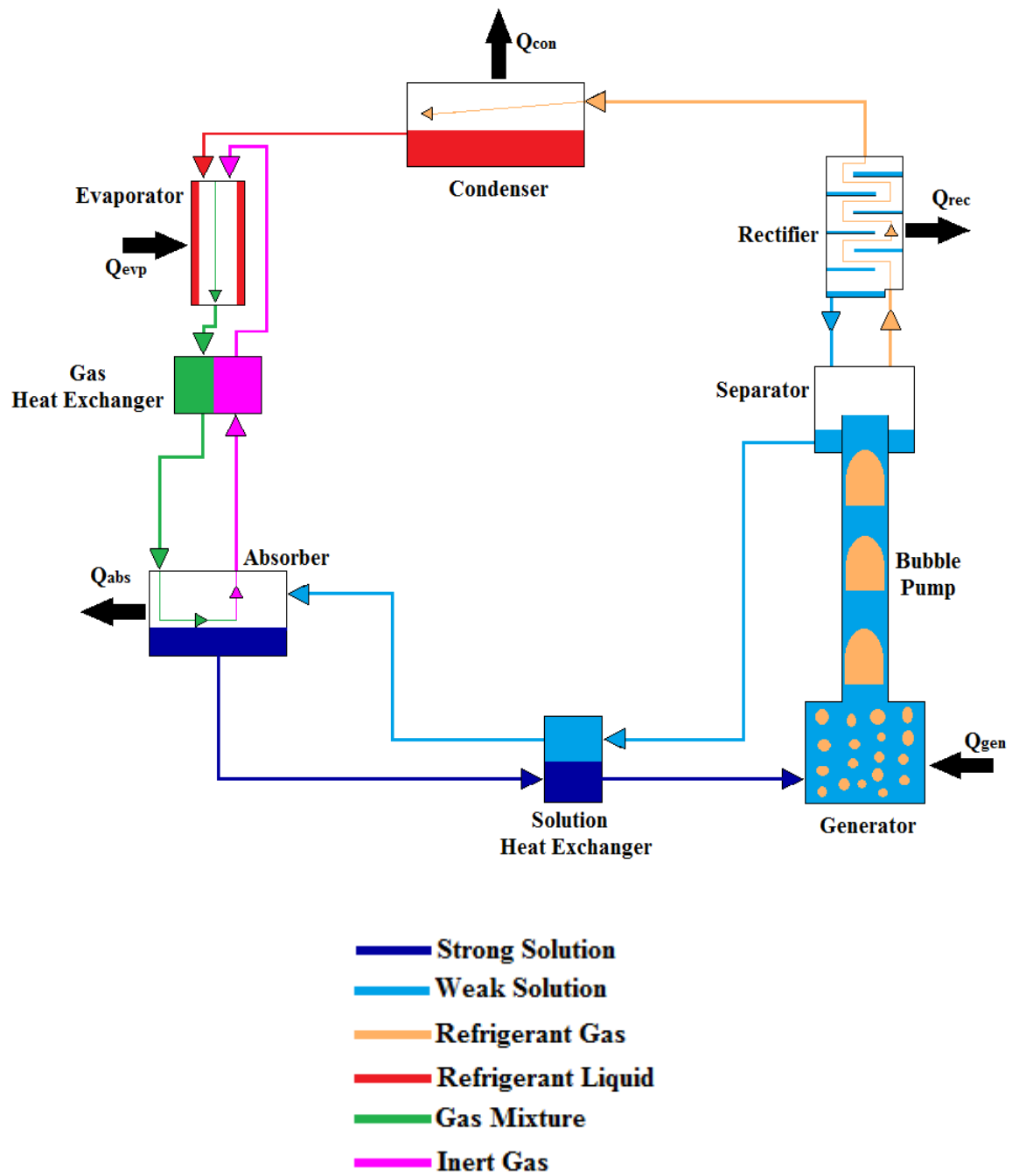


**Figure 15:** Schematic of a diffusion absorption refrigeration cycle

In the generator, heat is supplied to the strong solution (high ammonia content solution) of ammonia and water in order to drive off the refrigerant and circulate the fluid. As heat is supplied, from a source such as waste heat, the solution boils and generates vapour bubbles of refrigerant. These bubbles coalesce forming gas plugs (Taylor

bubbles) that act as pistons driven by buoyancy, lifting liquid slugs in the bubble pump. This action circulates the liquid in the DAR system to a separator.

At the separator, the weak solution (low ammonia content solution) leaving the bubble pump flows back to the absorber via a SHX, allowing heat to be recovered from the solution. The vapour leaving the bubble pump continues to the rectifier where any residual water is condensed to join the weak solution. As such, pure refrigerant (ammonia) leaves the rectifier and flows to the condenser where it condenses by releasing heat to the atmosphere. The condensed refrigerant liquid leaves the condenser and flows into the evaporator.

Since the evaporator is charged with the hydrogen, the partial pressure of the ammonia decreases as it enters the evaporator and starts to boil at low temperature in the presence of the hydrogen. In doing this, the heat of vaporisation of the refrigerant provides the refrigerating capacity of the DAR system. The gaseous mixture of ammonia and hydrogen leaves the evaporator due to the density difference between the ammonia-hydrogen mixture and the pure hydrogen entering the evaporator. As the gaseous mixture flows to the absorber, it passes through the GHX, which recovers heat from hydrogen returning to the evaporator. When the mixture reaches the absorber, the ammonia is absorbed by the weak solution converting it to a strong solution. The hydrogen, which is non-absorbable, flows back to the evaporator via the GHX.

Finally, the strong solution exiting the absorber flows back to the generator via the SHX. In the SHX, the strong solution is preheated by the weak solution flowing towards the absorber. The preheating of the strong solution is used to improve the performance of the system, as less heat is required to regenerate the strong solution.

### 3.3 Previous studies on DAR systems

Even though the DAR system was introduced nearly a century ago, the system has suffered from a major disadvantage of being limited to small refrigerating capacity. Many studies have been performed with a view to improve the performance of the DAR system (Rodriguez-Munoz and Belman-Flores, 2014). In their study, Chen et al. (1996) demonstrated that an increase in COP of up to 50% could be achieved by designing a generator that utilises the waste heat from the rectifier to heat the weak absorbent from the absorber.

Later, instead of a single component, Srihirin and Aphornratana (2002) experimentally investigated the performance of all the components of the DAR system using a mixture of  $\text{NH}_3\text{-H}_2\text{O-He}$ . They concluded that the bubble pump is an important component as it governs the circulation of the working fluid in the DAR system. However, the performance of the cycle is strongly dependent upon the wetted surface area in the evaporator and absorber. Since a greater wetted surface area would increase the evaporation of the refrigerant resulting in an increase in cooling effect.

Realising the need for increasing the cooling capacity of the DAR cycles, Jakob et al. (2008) performed their study on DAR systems having cooling capacity of 2.5 kW. They concluded that using coaxial solution heat exchanger as compared to plate heat exchanger improves the performance of the DAR system.

Most of the DAR models that have been developed were based on the assumption that pure refrigerant (i.e. without absorbent) enters the evaporator from the condenser; however, Starace and De Pascalis (2012) modelled a DAR system by considering

impure refrigerant entering the evaporator using  $\text{NH}_3\text{-H}_2\text{O}$  as the working fluid. They found that in the case where the refrigerant is not pure the COP of the system increases. However, the presence of water in refrigerants may cause freezing in the evaporator. They also concluded that the performance of the system depends upon the absorption temperature and the heat supplied to the generator. An increase in the absorption temperature lowers the absorption rate of the refrigerant in the weak solution resulting in the low performance of the DAR system. In addition, at low heat inputs the amount of heat loss from the bubble pump increases, which decreases the COP of the DAR system.

Yıldız and Ersoz (2013) experimentally investigated the amount of energy loss from the DAR system. They found that most of the energy was lost in the solution heat exchanger. Belman-Flores et al. (2014) compared the predictions of their numerical model with experimental results. They concluded that the factors that had the greatest influence on the performance of the system were the bubble pump length and its diameter.

Sozen et al. (2012) installed an ejector on the inlet line of the gas side of the absorber. They reported that by installing the ejector, the system pressure was raised, which increased the circulation rate of the refrigerant and gave a considerable reduction in the evaporator temperature.

Jelinek et al. (2016) used their model to examine performance of the DAR system under three levels of sub cooling, which were full, partial, and no. They concluded that for the same amount of heat input partial sub cooling of the refrigerant at the evaporator inlet resulted in the highest cooling effect and COP.

Based on the studies performed on the DAR system, it can be concluded that there are number of factors that influence the performance of the DAR system such as the generator temperature, the evaporation process, the rectification process, and the absorption process in the absorber. However, few available literature has discussed the narrow operating range of the DAR system as studied in Chapter 2. Hence, to develop a better understanding of the operational behaviour of the DAR system, it was decided to perform a sensitivity analysis to understand the factors that influence the performance of the DAR system.

### **3.4 Thermodynamic analysis of diffusion absorption refrigeration system**

In this analysis, the mass and the energy balance equations for each component of the system were developed, under the following assumptions and with reference to Figure 16. The assumptions of the model are:

- Steady state conditions;
- Hydrostatic pressure is neglected and there is no pressure and heat loss in the pipes connecting the system components;
- The temperature of the liquid and vapour leaving the generator are equal;
- No temperature drop in the bubble pump, i.e.  $T_{gen} = T_{13} = T_1$ ;
- The vapour leaving the rectifier from point (2) and evaporator from point (4) are saturated;
- The condenser and the absorber use the same cooling medium, i.e.  $T_3 = T_6$  (Starace and Pascallis, 2012);

- The effectiveness of both the heat exchangers is taken as one, i.e.  
 $Eff_{SHX} = Eff_{GHX} = 1$ .
- The heat released from the rectifier ( $\dot{Q}_{rec}$ ), condenser ( $\dot{Q}_{con}$ ), and absorber ( $\dot{Q}_{abs}$ ) flows to the ambient.

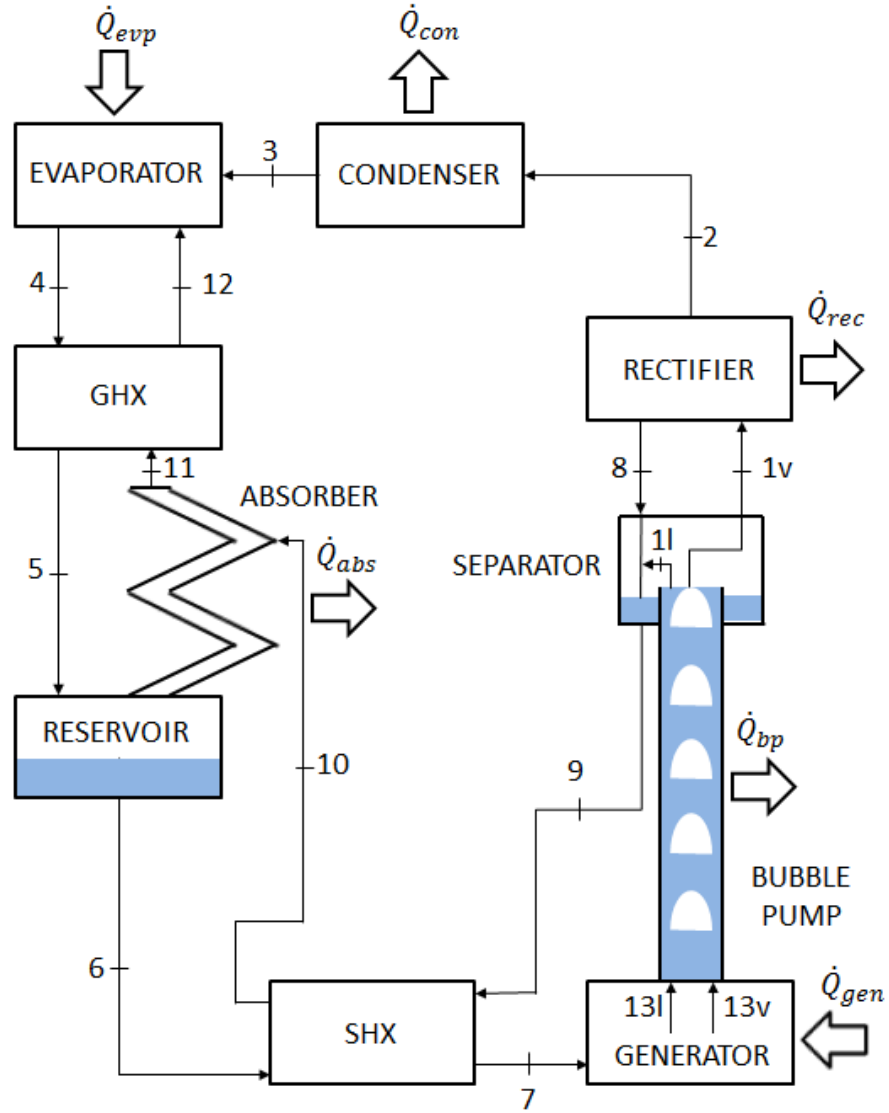


**Figure 16:** Schematic of the diffusion absorption refrigeration system

The corresponding mass and energy balance for each component of the DAR system are described as:

### 3.4.1 Generator

The strong solution ( $\dot{m}_7$ ) entering the generator from SHX leaves for the bubble pump in the form of refrigerant vapour ( $\dot{m}_{13v}$ ) and weak liquid solution ( $\dot{m}_{13l}$ ). As such, the mass balance across the generator is given by Equation 4:

$$\dot{m}_7 = \dot{m}_{13v} + \dot{m}_{13l} \quad (4)$$

In the generator, heat ( $\dot{Q}_{gen}$ ) is added to the strong solution, which boils the strong solution and converts it into a two-phase working fluid. Therefore, the energy balance across the generator is given by Equation 5:

$$h_7\dot{m}_7 + \dot{Q}_{gen} = h_{13v}\dot{m}_{13v} + h_{13l}\dot{m}_{13l} \quad (5)$$

The liquid phase leaving the generator is now weak in refrigerant concentration ( $x_{13}$ ), whereas the vapour phase leaving the generator is rich in refrigerant concentration ( $y_{13}$ ). The concentration of the working fluid across the generator can be obtained by using the component balance given by Equation 6:

$$x_7\dot{m}_7 = y_{13}\dot{m}_{13v} + x_{13}\dot{m}_{13l} \quad (6)$$

### 3.4.2 Bubble pump

The vapour bubbles ( $\dot{m}_{13v}$ ) along with the liquid ( $\dot{m}_{13l}$ ) enter the bubble pump from the generator and leave for the separator as liquid solution ( $\dot{m}_{1l}$ ) weak in refrigerant concentration and vapour ( $\dot{m}_{1v}$ ) rich in refrigerant concentration. The mass balance for the bubble pump is given by Equation 7:

$$\dot{m}_{13v} + \dot{m}_{13l} = \dot{m}_{1v} + \dot{m}_{1l} \quad (7)$$

The energy balance across the bubble pump is given by Equation 8:

$$h_{13v}\dot{m}_{13v} + h_{13l}\dot{m}_{13l} = h_{1v}\dot{m}_{1v} + h_{1l}\dot{m}_{1l} \quad (8)$$

The concentration of the working fluid across the bubble pump can be calculated using the component balance given by Equation 9:

$$y_{13}\dot{m}_{13v} + x_{13}\dot{m}_{13l} = y_1\dot{m}_{1v} + x_1\dot{m}_{1l} \quad (9)$$

### 3.4.3 Separator

In the separator, the two-phases of the working fluid coming from the bubble pump are separated from each other. The refrigerant vapour ( $\dot{m}_{1v}$ ) together with some liquid carryover flows to the rectifier. The weak solution ( $\dot{m}_{1l}$ ) combined with the absorbent rich solution ( $\dot{m}_8$ ) exits the rectifier and this mixture ( $\dot{m}_9$ ) then flows to the SHX. The mass balance of the working fluid across the separator is determined using Equation 10:

$$\dot{m}_8 + \dot{m}_{1l} + \dot{m}_{1v} = \dot{m}_9 + \dot{m}_{1v} \quad (10)$$

Now, due to mixing of the two liquids i.e. the weak liquid solution ( $\dot{m}_{1l}$ ) and the absorbent liquid ( $\dot{m}_8$ ), the refrigerant concentration ( $x_9$ ) of the solution ( $\dot{m}_9$ ) changes.

The component balance across the separator is given by Equation 11:

$$x_8\dot{m}_8 + x_1\dot{m}_{1l} = x_9\dot{m}_9 \quad (11)$$

The energy balance across the separator is given by Equation 12:

$$h_8\dot{m}_8 + h_{1l}\dot{m}_{1l} = h_9\dot{m}_9 \quad (12)$$

### 3.4.4 Rectifier

In the rectifier, any residual absorbent is removed from the refrigerant vapour. The pure refrigerant vapour ( $\dot{m}_2$ ) flows to the condenser whereas the residual absorbent ( $\dot{m}_8$ ) flows back to the separator. As such, the mass balance across the rectifier is given by Equation 13:

$$\dot{m}_{1v} = \dot{m}_2 + \dot{m}_8 \quad (13)$$



The removal of the residual absorbent from the refrigerant vapour changes the concentration ( $y_1$ ) of the refrigerant in the vapour and converts it into a near pure refrigerant vapour ( $y_2$ ). As such, the concentration of the working fluids across the rectifier can be obtained from the component balance using Equation 14:

$$y_1 \dot{m}_{1v} = y_2 \dot{m}_2 + x_8 \dot{m}_8 \quad (14)$$

In the rectifier, the residual absorbent is condensed from the refrigerant vapour by the removal of heat ( $\dot{Q}_{rec}$ ). As such, the energy balance across the rectifier is given by Equation 15:

$$h_{1v} \dot{m}_{1v} = h_2 \dot{m}_2 + h_8 \dot{m}_8 + \dot{Q}_{rec} \quad (15)$$

### 3.4.5 Condenser

In the condenser, the refrigerant vapour condenses while releasing heat ( $\dot{Q}_{con}$ ). The condensed refrigerant leaves the condenser and flows to the evaporator. The energy balance across the condenser is given by Equation 16:

$$h_2 \dot{m}_2 = h_3 \dot{m}_3 + \dot{Q}_{con} \quad (16)$$

As there is a single inlet and outlet to the condenser, the mass flow of the refrigerant is conserved. Therefore:  $\dot{m}_2 = \dot{m}_3$ , and  $y_2 = x_3$ .

### 3.4.6 Evaporator

In the evaporator, the liquid refrigerant ( $\dot{m}_3$ ) is mixed with the auxiliary inert gas ( $\dot{m}_{12i}$ ). The vapour mixture of refrigerant ( $\dot{m}_4$ ) and auxiliary inert gas ( $\dot{m}_{4i}$ ) leaves the evaporator and flows to the GHX. The mass balance across the evaporator can be evaluated using Equation 17:

$$\dot{m}_3 + \dot{m}_{12} + \dot{m}_{12i} = \dot{m}_4 + \dot{m}_{4i} \quad (17)$$

In the evaporator, heat is transferred from the refrigeration load ( $\dot{Q}_{evp}$ ), causing the refrigerant to evaporate. Therefore, the energy balance across the evaporator is given by Equation 18:

$$h_3\dot{m}_3 + h_{12}\dot{m}_{12} + h_{12i}\dot{m}_{12i} + \dot{Q}_{evp} = h_4\dot{m}_4 + h_{4i}\dot{m}_{4i} \quad (18)$$

The concentration of the working fluid at the inlet and exit of the evaporator can be calculated from the component balance using Equation 19:

$$x_3\dot{m}_3 + y_{12}\dot{m}_{12} = y_4\dot{m}_4 \quad (19)$$

In the evaporator, the partial pressure of the refrigerant drops, causing it to boil. The partial pressure ( $P_{part}$ ) of the refrigerant at the exit (4) and inlet (12) can be determined from Dalton's Law, which is given by Equation 20 (Ben Ezzine et al., 2010):

$$P_{part} = \frac{\dot{m}_r/\bar{M}_r}{\dot{m}_r/\bar{M}_r + \dot{m}_i/\bar{M}_i} P_{sys} \quad (20)$$

Where  $\dot{m}_r$  is the mass flow rate of the refrigerant,  $P_{sys}$  is the system pressure,  $\bar{M}_r$  is the molar mass of the refrigerant, and  $\bar{M}_i$  is the molar mass of the inert gas.

### 3.4.7 Gas heat exchanger

The gas heat exchanger acts as a regenerator where the gas and vapour coming from the evaporator and the absorber exchange heat with each other. The energy balance across the GHX is given by Equation 21:

$$\begin{aligned} & h_4\dot{m}_4 + h_{4i}\dot{m}_{4i} + h_{11}\dot{m}_{11} + h_{11i}\dot{m}_{11i} \\ & = h_5\dot{m}_5 + h_{5i}\dot{m}_{5i} + h_{12}\dot{m}_{12} + h_{12i}\dot{m}_{12i} \end{aligned} \quad (21)$$

Since there is no mixing of working fluids in the GHX, the mass flow rate and the concentration of the constituents at the inlet and exit of the GHX remain the same i.e.  $\dot{m}_4 = \dot{m}_5$ ,  $\dot{m}_{11} = \dot{m}_{12}$ ,  $\dot{m}_{4i} = \dot{m}_{5i}$ ,  $\dot{m}_{11i} = \dot{m}_{12i}$ ,  $y_4 = y_5$ , and  $y_{11} = y_{12}$ . Additionally, the effectiveness of the heat exchanger ( $Eff_{GHX}$ ) can be calculated using Equation 22:

$$Eff_{GHX} = \frac{(T_{11} - T_{12})}{(T_{11} - T_4)} \quad (22)$$

### 3.4.8 Absorber

The gaseous mixture of refrigerant ( $\dot{m}_5$ ) and auxiliary inert gas ( $\dot{m}_{5i}$ ) coming from the GHX enter the absorber, where the refrigerant is absorbed by the weak solution ( $\dot{m}_{10}$ ) coming from the SHX to form a strong solution ( $\dot{m}_6$ ) with the aid of heat rejection ( $\dot{Q}_{abs}$ ). The auxiliary inert gas ( $\dot{m}_{11i}$ ), along with the small amount of unabsorbed refrigerant ( $\dot{m}_{11}$ ), flows back to the evaporator through the GHX, while the strong liquid solution flows to the generator through the SHX. As such, the mass balance across the absorber is given by Equation 23:

$$\dot{m}_5 + \dot{m}_{5i} + \dot{m}_{10} = \dot{m}_6 + \dot{m}_{11} + \dot{m}_{11i} \quad (23)$$

As the absorption process is exothermic, heat ( $\dot{Q}_{abs}$ ) is transferred from the absorber. As such, the energy balance across the absorber can be evaluated using Equation 24:

$$h_5\dot{m}_5 + h_{5i}\dot{m}_{5i} + h_{10}\dot{m}_{10} = h_6\dot{m}_6 + h_{11}\dot{m}_{11} + h_{11i}\dot{m}_{11i} + \dot{Q}_{abs} \quad (24)$$

Also, due to the transformation of the weak liquid solution into the strong liquid solution, the concentration of the refrigerant ( $x_6$ ) in the strong liquid solution changes and can be calculated from the component balance using Equation 25:

$$y_5\dot{m}_5 + x_{10}\dot{m}_{10} = x_6\dot{m}_6 + y_{11}\dot{m}_{11} \quad (25)$$

### 3.4.9 Solution heat exchanger

The SHX acts as another regenerator where both the weak and strong liquid solutions exchange heat. The energy balance across the SHX is given by Equation 26:

$$h_6\dot{m}_6 + h_9\dot{m}_9 = h_7\dot{m}_7 + h_{10}\dot{m}_{10} \quad (26)$$

Since there is no mixing of the working fluids in the SHX, the mass flow rate and the concentration of the working fluids at the inlet and exit of the SHX remain the same.

Therefore:  $\dot{m}_6 = \dot{m}_7$ ,  $\dot{m}_9 = \dot{m}_{10}$ ,  $x_6 = x_7$ , and  $x_9 = x_{10}$ . Additionally, the effectiveness of the heat exchanger ( $Eff_{SHX}$ ) can be calculated using Equation 27:

$$Eff_{SHX} = \frac{T_9 - T_{10}}{T_9 - T_6} \quad (27)$$

### 3.4.10 Performance parameters

For this work, the performance of the DAR system was evaluated in terms of the Coefficient of Performance (COP) and the circulation ratio ( $f$ ). The COP of the DAR system was calculated using Equation 28:

$$COP = \frac{\dot{Q}_{evp}}{\dot{Q}_{gen}} \quad (28)$$

The other important parameter, which is the circulation ratio, is defined as the ratio of the mass flow rate of the strong solution ( $\dot{m}_7$ ) and that of the refrigerant ( $\dot{m}_2$ ). In the DAR system, the primary purpose of the bubble pump is the circulation of the working fluid; however, the other purpose of the bubble pump is to desorb the refrigerant from the rich solution (Koyfman et al., 2003). As such, the amount of refrigerant desorbed from the rich solution is estimated using the circulation ratio.

Long et al. (2013) and Ben Ezzine et al. (2010) suggest that for higher operation efficiencies it is essential to operate the DAR system at low circulation ratio, as less strong solution has to be circulated to generate more refrigerant. The circulation ratio can be determined using Equation 29:

$$f = \frac{\dot{m}_7}{\dot{m}_2} \quad (29)$$

Having outlined the mass and energy balances and other relationships for the DAR system, a model was developed using the software package Engineering Equation Solver (EES) (version V9.722, 2014) which contains the thermodynamic properties of various working fluids to determine the performance of the system. In this respect, the properties of ammonia vapour and water vapour were calculated from the EES database, whereas the properties of the ammonia-water solution at various points of the system were calculated using the correlations given by Patek and Klomfar (1995) and Bourseau and Bugarel (1986).

### **3.5 Solution verification of the model**

To verify the solutions of the DAR model, the model was compared with the model results of Ersoz (2015). In their model, Ersoz used ammonia as the refrigerant, water as absorbent, and helium as the inert gas. As such, the same working fluid combination and the same operating conditions were selected, as shown in Table 1.

**Table 1:** Operating parameters for model comparison

<b>Parameter</b>	<b>Value</b>
Operating pressure (bar)	14.92
Heat input to generator (W)	115
Generator temperature (°C)	149.87
Bubble pump outlet temperature (°C)	128.39
Rectifier outlet temperature (°C)	69.32
Condenser outlet temperature (°C)	28.07
Absorber liquid side outlet temperature (°C)	23.67
Mass flow rate of rich solution (g/s)	0.157

The results, shown in Table 2 showed good agreement with the results of the Ersoz (2015) model, thus suggesting the model is suitable for analysing DAR systems.

**Table 2:** Comparison between the developed model and Ersoz (2015) model

<b>Parameter</b>	<b>This Model</b>	<b>Ersoz (2011) Model</b>
Refrigerating Effect (W)	31.33	32.79
Ammonia concentration in rich solution	0.34	0.32
Heat loss from condenser (W)	26.38	23.00
Heat loss from absorber (W)	23.61	21.85
Circulation ratio	6.24	6.50
Mass flow rate of refrigerant (g/s)	0.025	0.024

### 3.6 Influence of system parameters and components

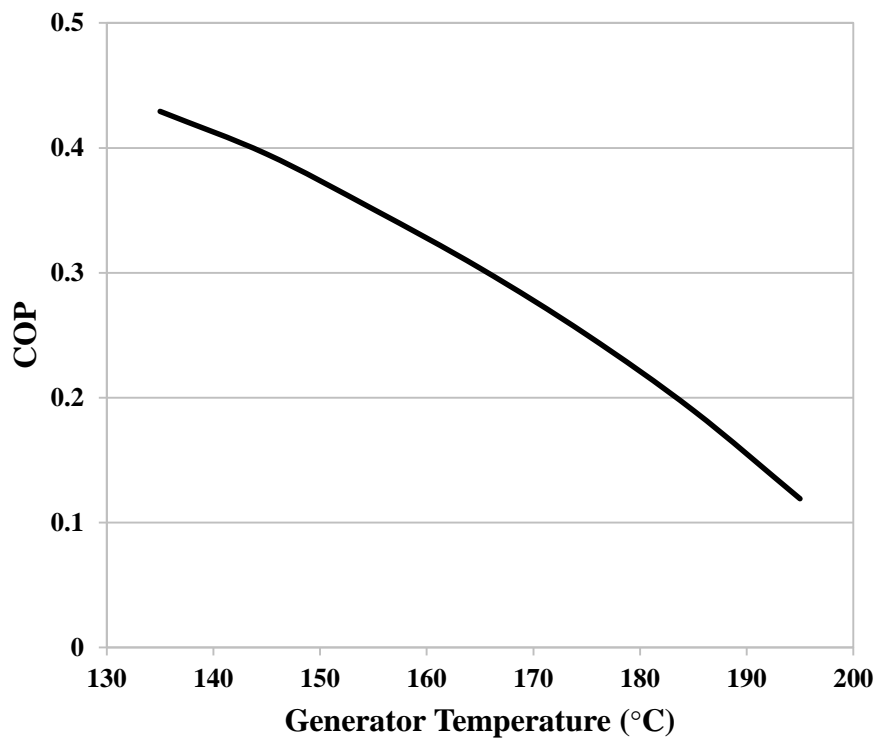
Having verified the predictions of the model, it was used to study the influence of the DAR system parameters and components. The input parameters required for the analysis are given in Table 3.

**Table 3:** Input operating parameters for the analysis

Parameter	Value
Generator temperature range (°C)	130 - 200
Condenser temperature (°C)	50
Evaporator exit temperature (°C)	10
Heat Input (W)	2500
Ammonia mass fraction of strong solution	0.3
Effectiveness of heat exchangers	1

### 3.6.1 Influence of generator temperature on performance

The experimental results discussed in Chapter 2 suggest that at high exhaust temperatures the DAR system was not able to produce any cooling effect. Now, any variation in the exhaust temperature can influence the temperature of the working fluid in the generator of the DAR system. Figure 17 shows the effect of the generator temperature ( $T_{gen}$ ) on COP. It can be seen that with the increase in generator temperature the COP tends to decrease.

**Figure 17:** Influence of generator temperature on COP

This is due to a reduction in the ammonia mass fraction of the vapour ( $y_{13}$ ) generated with increased generator temperature, as shown in Figure 18. The reason behind the drop in the ammonia mass fraction of vapour at higher generator temperatures is due to the boiling point of ammonia being lower than that of water.

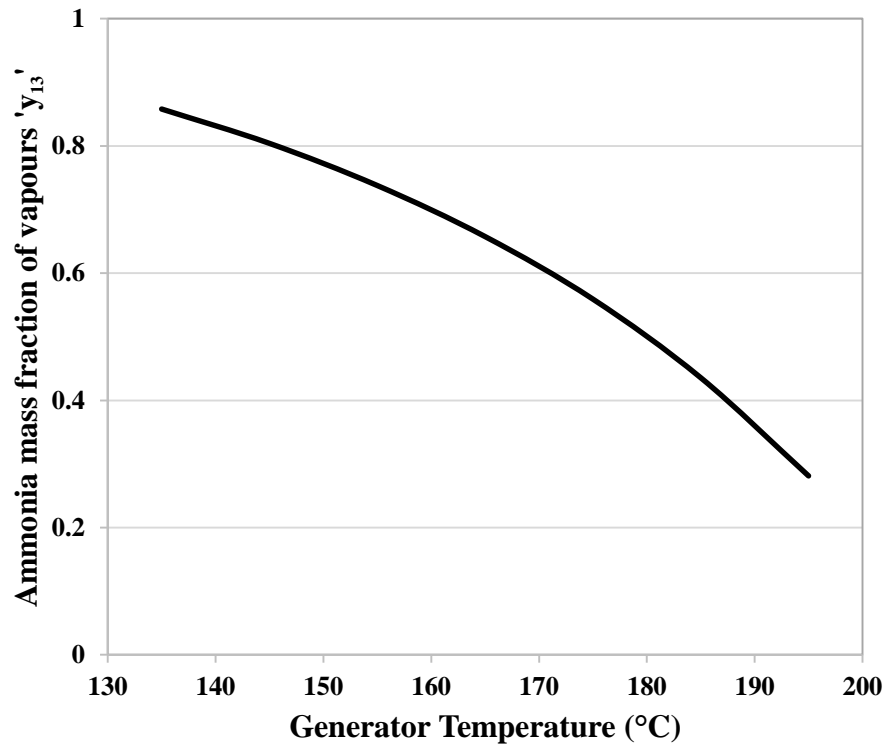


**Figure 18:** Influence of generator temperature on ammonia mass fraction of vapours leaving generator

At low generator temperatures the ammonia liquid starts evaporating first, resulting in vapour with a high concentration of ammonia; however, as the generator temperature is increased the water starts evaporating thus forming vapour rich in water. In order to have high concentrated ammonia refrigerant at the inlet of the condenser, the residual water present in the vapour refrigerant is removed in the rectifier. This results in a lower mass flow of refrigerant to the evaporator and eventually a decrease in the performance. This helps to explain why the cooling effect stopped at high exhaust temperatures in the preliminary experimental investigation.



### 3.6.2 Influence of generator temperature on circulation ratio

As mentioned earlier the circulation ratio is an important parameter for evaluating the performance of the DAR system. Figure 19 shows the influence of the generator temperature on the circulation ratio of the DAR cycle.

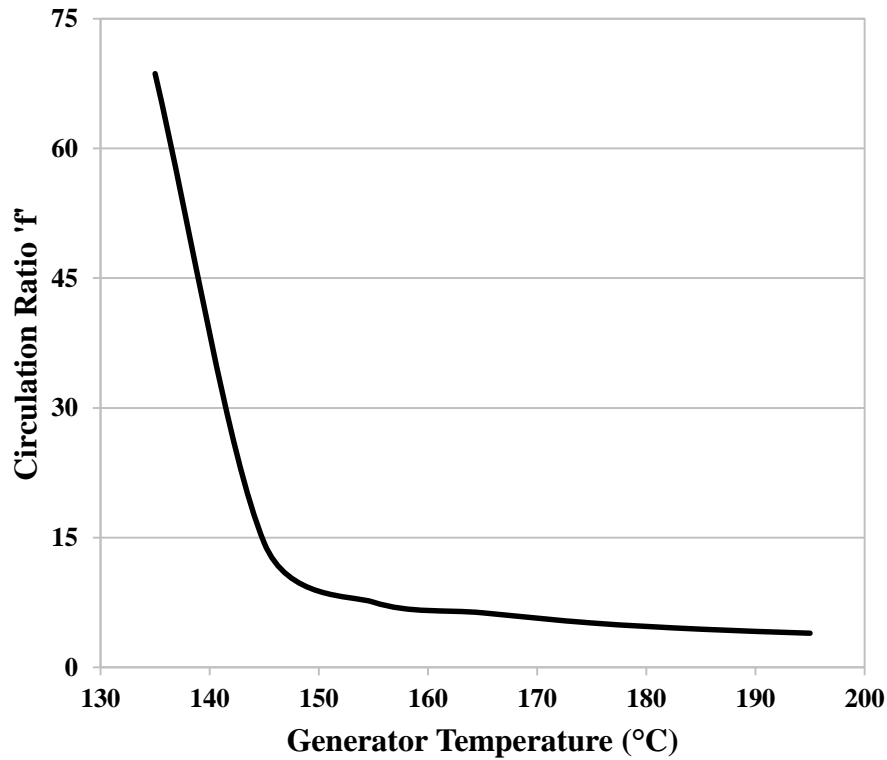


**Figure 19:** Influence of generator temperature on circulation ratio

The circulation ratio is high at low generator temperatures and decreases gradually as the generator temperature increases. This suggests that at low generator temperature the percentage of the ammonia refrigerant ( $\dot{m}_{13v}$ ) desorbed from the rich solution is low as compared to high generator temperature. Even though the performance of the DAR system is better at low generator temperature as shown in Figure 17; however, it requires a large quantity of the strong solution to be circulated in the DAR system. This

also serves to explain the lack of cooling at low exhaust temperatures in the preliminary experimental investigation.

### 3.6.3 Influence of strong solution mass fraction on COP

Figure 20 shows the effect of the ammonia mass fraction on the COP of the system. At a fixed generator temperature, the COP rises with an increase in ammonia mass fraction. This is because the refrigerant vapour produced in the generator is rich in ammonia concentration, resulting in an increase in the cooling effect.

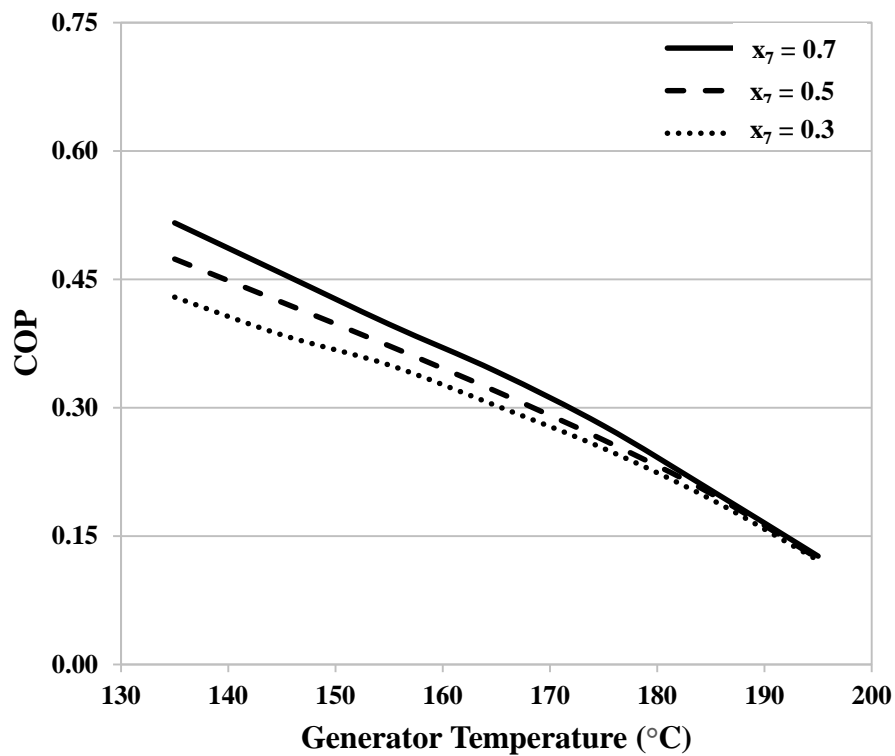


**Figure 20:** Influence of ammonia mass fraction of strong solution on COP

### 3.6.4 Influence of rectifier

In the rectifier, the residual water is removed from the refrigerant before flowing to the condenser. The removal of the residual water is achieved by the difference in the

saturation temperature of ammonia and water. In the rectifier, some heat is lost from the refrigerant vapour ( $\dot{m}_{1v}$ ) resulting in a drop in the temperature of the refrigerant and water vapour. Due to this temperature drop, the water content present in the refrigerant condenses due to its high saturation temperature compared to ammonia. The effect of the rectification can be seen in Figure 21, which shows the performance of the system with different ammonia mass fractions ( $y_2$ ) at the entrance of the condenser.

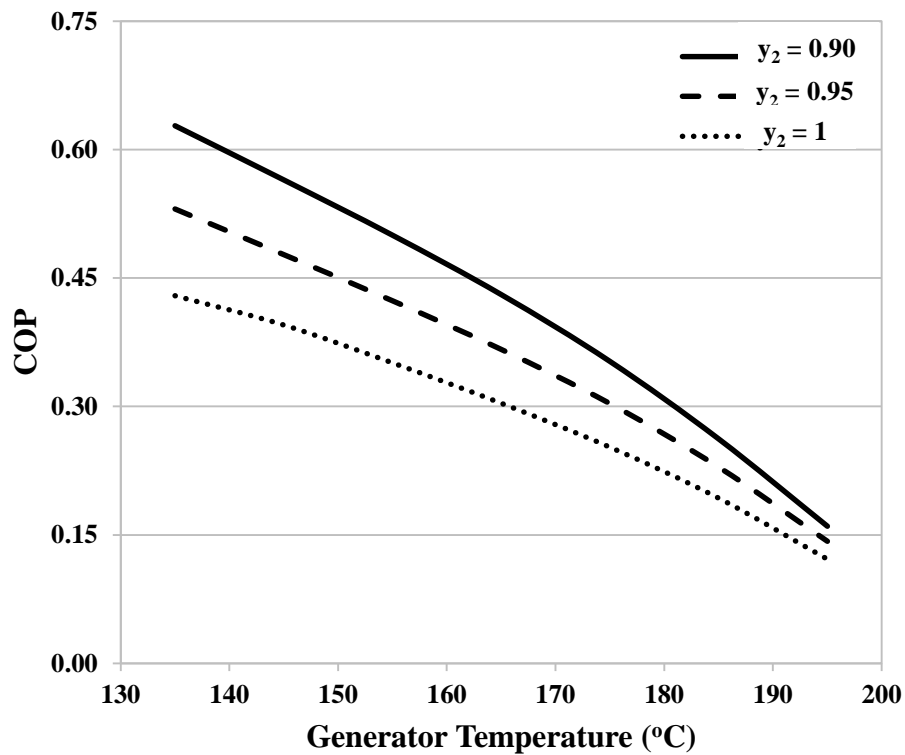


**Figure 21:** Influence of mass fraction of ammonia vapour entering condenser on COP

It can be seen that the COP increases with the reduction in the ammonia mass fraction of the refrigerant at the condenser inlet. The increase in water vapour content in the refrigerant increases the refrigeration capacity due to the higher heat of vaporisation of water. However, the presence of water vapour would cause ice formation at low evaporator temperatures, which may cause damage in the evaporator.

### 3.6.5 Influence of evaporator temperature on COP

In order to evaluate the influence of the evaporator temperature on the performance of the DAR system. Figure 22 shows that a change in the evaporator temperature does not significantly influences its COP.

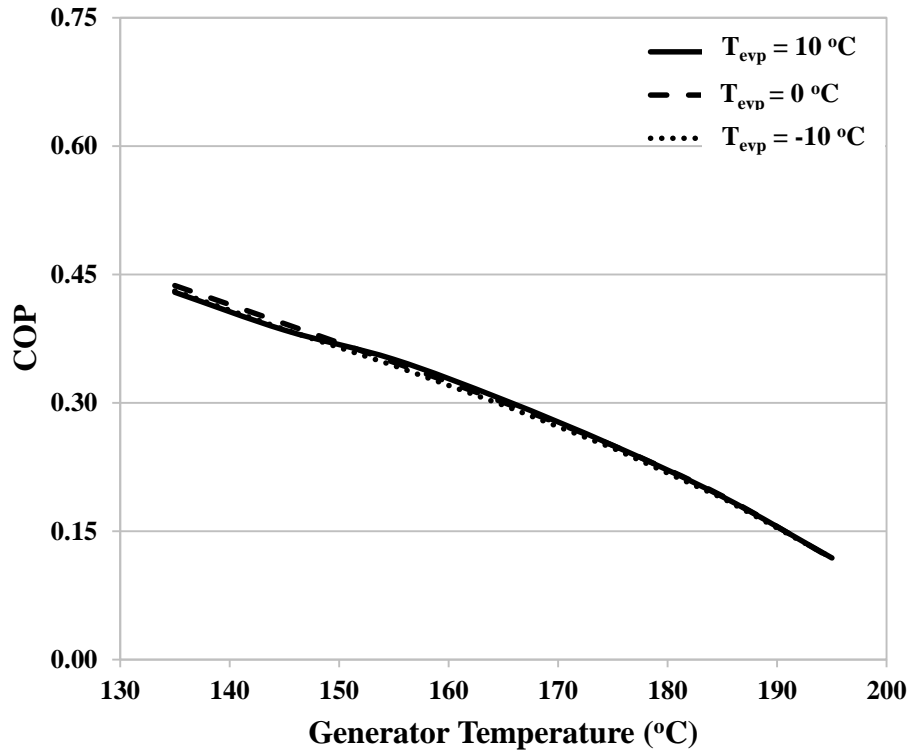


**Figure 22:** Influence of evaporator temperature on COP

However, in order to lower the pressure of the refrigerant and thus achieve low evaporator temperatures, more inert gas is needed, as shown in Figure 23.

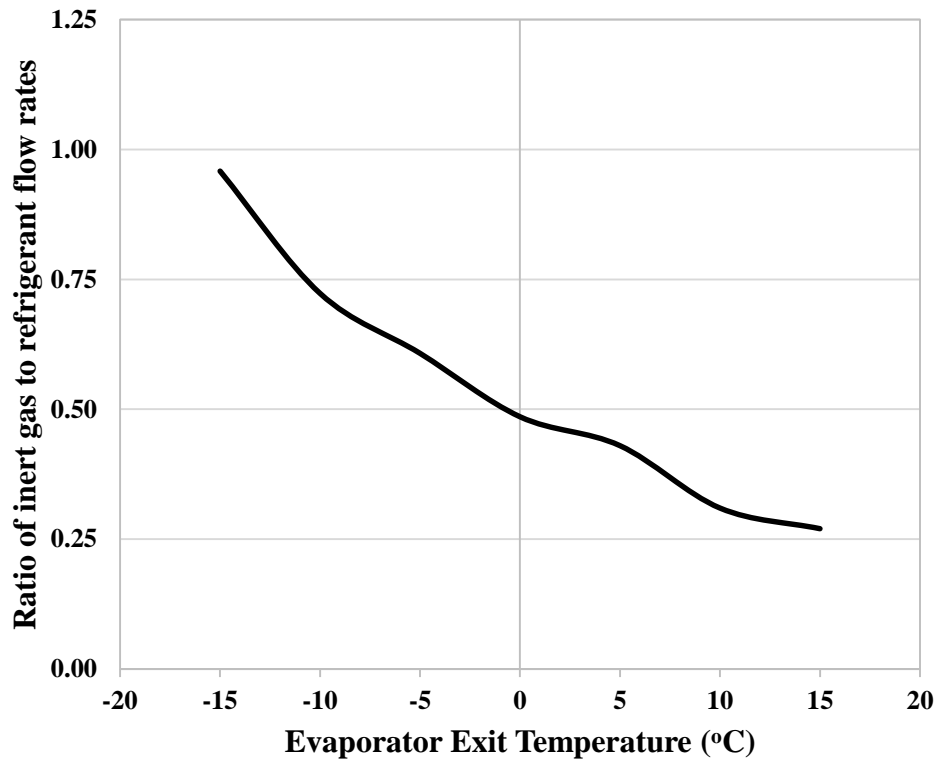


**Figure 23:** Ratio of inert gas flow rate to refrigerant flow rate

### 3.6.6 Influence of condenser temperature on COP

Moving from the evaporator to the condenser, at a given evaporator temperature, an increase in the condenser temperature reduces the performance of the DAR as shown in Figure 24. An increase in the condenser temperature increases the enthalpy of the working fluid entering the evaporator. As such, the thermal load on the evaporator increases, which results in a reduction in the performance of the DAR system.

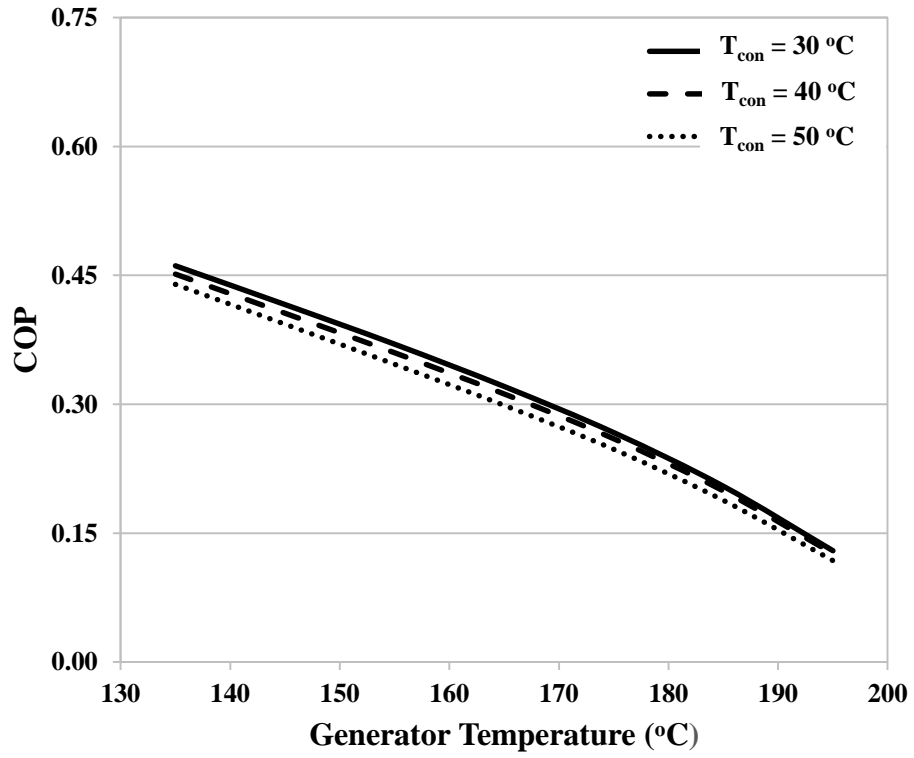


**Figure 24:** Influence of condenser temperature on COP

### 3.7 Comparison between DAR model and preliminary experiment

Having analysed the influence of different operating parameters on the performance of the DAR system through the developed thermodynamic model, it was decided to use this model in predicting the behaviour of the DAR system discussed in Chapter 2. In the experimental investigation, it was noted that the minimum temperature achieved at the evaporator was when the DAR system was running at CCHP mode. As such, the average temperature values at different points of the DAR system in CCHP mode were used as input parameters for the DAR model, as shown in Table 4.

**Table 4:** Input parameters for DAR model

Parameter	Value
Heat input (W)	126
Generator temperature (°C)	177
Condenser outlet temperature (°C)	34
Absorber outlet temperature (°C)	40
Evaporator temperature (°C)	11

For estimating the performance of the DAR system using the developed model, the concentration of the ammonia in the rich solution is required. Since, the experimental DAR system was completely sealed; it was not possible to determine the exact ammonia-water concentration of the rich solution. In other experimental studies of the DAR system, a typical value in the range of 0.25 – 0.32 has been proposed for the concentration of the ammonia in the rich solution (Yildiz et al., 2014, Yildiz and Ersoz, 2013). As such, a value of 0.3 was used for the concentration of ammonia in the rich solution. On this basis, the cooling load estimated by the model was 9.26 W and that in the experiment was  $6.81 \pm 0.8$  W (Appendix B).

### 3.8 Conclusion

In this study, a thermodynamic model for a DAR was developed and verified using existing literature and validated against the experimental data from Chapter 2. A parametric sensitivity analysis of the DAR system showed that with an increase in generator temperature, the performance of the DAR system decreases. However, at low generator temperature the value of the circulation ratio is high suggesting that more

working fluid needs to be circulated by the bubble pump of the DAR system. Furthermore, the performance of the DAR system is influenced by several other factors notably the condenser temperature, rectification process, and the ammonia mass fraction of the strong solution.

Now, in the preliminary investigation of the ICE based tri-generation system (Chapter 2), it was found that the DAR system was not able to activate at low generator temperature, hence resulting in no refrigerating effect. This suggests that in the preliminary investigation, the DAR system was not able to achieve the required circulation ratio at low generator temperature. Hence, it was hypothesised, that this could be a limitation of the bubble pump not being able to pump the required quantity of the working fluid. As such, it is important to investigate the operation of a bubble pump and to determine the factors influencing the pumping performance of the bubble pump.



# Chapter 4: Performance analysis of a bubble pump

## 4.1 Overview

In Chapter 2 and 3, it was noted that the generator temperature influences the performance of the DAR system. It was hypothesised that the variations in the generator temperature may influence the amount of the working fluid pumped by the bubble pump. As the bubble pump is the most important component of the DAR system, it was decided to investigate the operation of the bubble pump. A bubble pump as shown in Figure 25 is a vertical tube that uses thermal energy to pump liquid from a lower level to higher level.

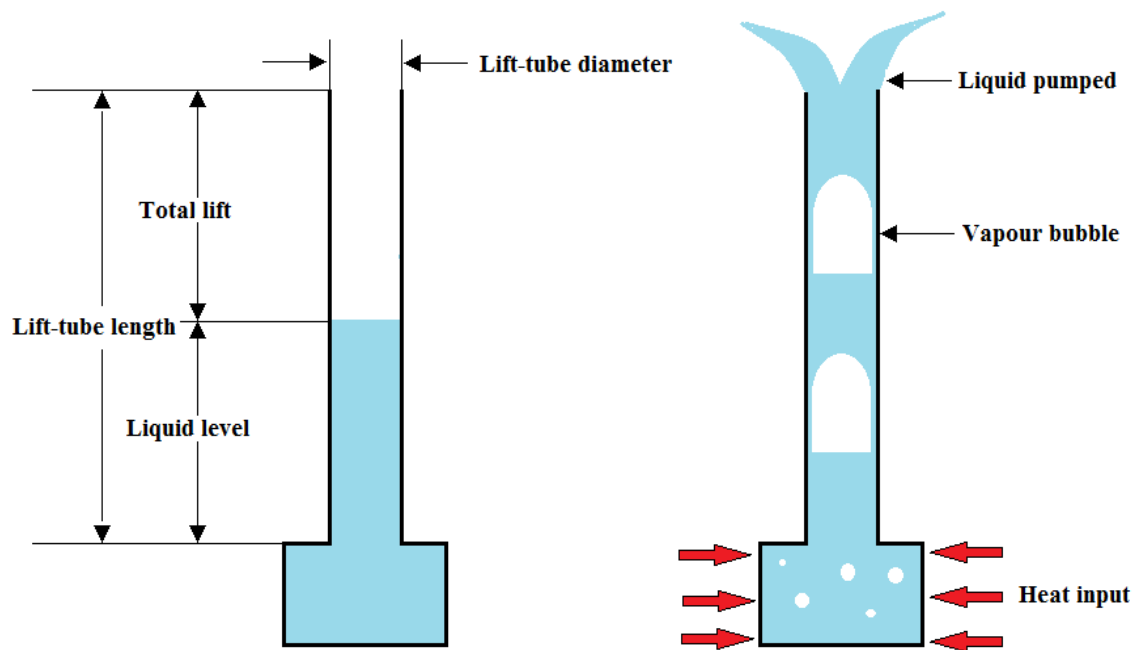


**Figure 25:** Schematic of a bubble pump

As heat is supplied, the liquid boils forming vapour bubbles, which lift the liquid along the tube length. The boiling of the liquid results in the formation of four basic two-phase flow regimes named as bubbly, slug, churn, and annular as shown in Figure 26.

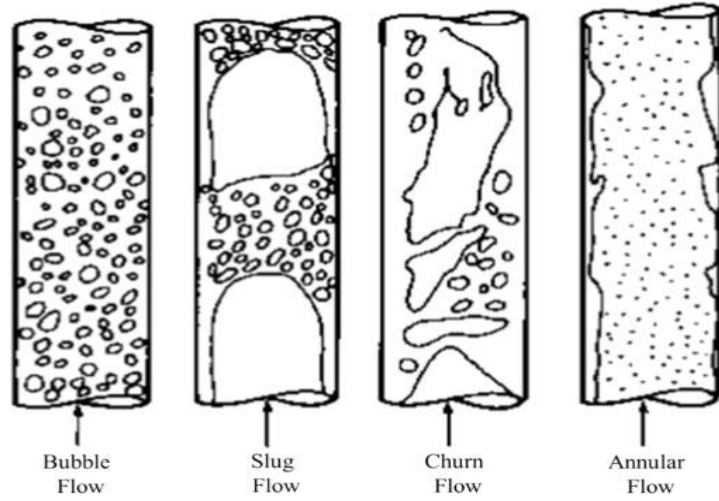


**Figure 26:** Vertical two-phase flow regimes (Montoya et al. 2016)

In bubbly flow regime, the bubbles do not interact with each other and move separately as individual bubbles within the liquid. However, as the velocity of the gas is increased the individual bubbles interact with each other forming bullet shaped bubbles, which give rise to slug flow regime (Morgado et al., 2016). As the velocity of the gas is increased the bullet shaped bubbles break leading to an unstable churn flow regime. Further increasing the gas velocity, both the gas and the liquid flows separately. As such, this flow regime is termed as annular flow regime, in which the liquid flows along the inner wall of the lift-tube, while the gas flows in the centre carrying very small droplets of liquid.

The amount of the liquid pumped by the bubble pump depends upon several parameters. These include the flow regime, forces acting on the two-phase mixture, lift-tube diameter, lift-tube length, and the submergence ratio, defined as the ratio between the liquid level in the lift-tube to the total lift-tube length and is given by Equation 30:

$$\text{Submergence Ratio (SR)} = \frac{\text{Liquid level in the lift-tube}}{\text{Total lift-tube length}} \quad (30)$$

The principal forces acting on a two-phase vertical flow of the bubble pump are buoyancy, gravitational, and inertia forces in which the buoyancy and the inertia forces acts as the lifting force, while the gravitational force acts as an opposing force (Hanafizadeh et al., 2011a). The performance of the bubble pump is also affected by the fluid properties such as viscosity of the liquid. Kim et al. 2014 mentions that the bubble flow patterns depend strongly on liquid viscosity. A decrease in the liquid viscosity delays the transition of the flow regime (Furukawa and Fukano, 2001).

Several studies have been conducted to identify the factors influencing the operation of the bubble pump and its impact on the performance of the DAR system. Pfaff et al. (1998) investigated both analytically and experimentally the performance of the bubble pump. They found that the pumping ratio, the ratio between the flow rates of the strong solution and the refrigerant, increases with a decrease in the lift-tube diameter. Increasing the lift-tube diameter changes the flow regime inside the lift-tube, eventually decreasing the pumping ratio.

White (2001) used mass and momentum conservation equations to model the performance of the bubble pump. The model developed was verified through experiments performed on an air-lift bubble pump using water as a working fluid. White found that the performance of the bubble pump was highly dependent on the submergence ratio as well as on the flow regime. The peak performance of the bubble pump lies at the transition from slug to churn flow regime. Furthermore, White used the developed model to successfully predict the performance of a heat driven  $\text{NH}_3\text{-H}_2\text{O}$  bubble pump.

Zohar et al. (2008) investigated the influence of the concentric tube bubble pump on the performance of the DAR system. The inner tube acted as a bubble pump and the weak solution flows back through the insulated outer tube. The liquid present in the inner tube transfers some of its heat to the weak solution in the outer tube. It was found that using concentric tube bubble pump, the amount of refrigerant desorbed from the strong solution improves, resulting in an increase in the cooling effect.

Benhmidene et al. (2011) numerically investigated the optimum heat flux required for the efficient operation of the bubble pump. Based on the lift-tube diameter, they derived an empirical relation to calculate the optimum and minimum heat flux required for pumping the liquid.

Chan and McCulloch (2013) developed a model based on the model developed by Pfaff et al. (1998), assuming heat loss from the bubble pump. Chan and McCulloch verified their model by performing an experiment and found that the loss of heat from the bubble pump changes the amount of liquid pumped by the bubble pump. Furthermore, they found that the performance of the bubble pump increased with a decrease in the lift-tube diameter.

Using a commercial CFD code FLUENT, Garma et al. (2014) simulated the influence of the heat distribution on the flow behaviour of the bubble pump. Two cases of heat distribution on the bubble pump were investigated. In the first case, heat was uniformly distributed along the length of the lift-tube, while in the second case heat was supplied to a small region at the bottom of the lift-tube. It was found that the bubble pump operates more efficiently when the heat was distributed along the lift-tube length.

Instead of analysing the performance of the bubble pump as an individual component, Belman-Flores et al. (2014) studied the performance of the DAR system by varying the geometrical parameters of the bubble pump. They concluded that the factors that most influence the performance of the DAR system are the lift-tube length and its diameter. Han et al. (2015) experimentally studied the performance of a bubble pump. They found that the pumping ratio reduced with a decrease in the lift-tube diameter and increase in the vapour flow rate.

The studies performed suggest that the performance of the bubble pump is influenced by geometric parameters and the flow regime inside the lift-tube. However, limited literature is available describing the flow behaviour inside the tube. As several other factors may influence the operation of the bubble pump such as formation of bubbles, buoyancy forces, viscous forces, drag forces, bubble-bubble and bubble-liquid interaction. Therefore, in order to understand this, a more detailed analysis on the operation of the bubble pump was undertaken.

## **4.2 Experimental method**

In order to understand the pumping phenomena of the bubble pump an experimental investigation was performed. The experimental system was based on an airlift pump, which operates in a mechanistically similar manner to a heat driven bubble pump (Chan and McCulloch, 2013). In a heat-driven bubble pump, bubbles are formed due to liquid vaporisation whereas in the case of airlift pumps air is injected to produce the bubbles. For this experiment, air and water were used as the working fluid. All the tests were performed at ambient conditions.

The experimental setup, as shown in Figure 27, consists of a lift-tube having its lower end placed at the centre of the lower tank. The upper end of the lift-tube was connected to a separator tank from where the pumped liquid was directed towards the measuring cylinder to measure the flow rate of the liquid pumped. In order to observe the two-phase flow, the lift-tube along with the lower and separator tank were made of transparent acrylic plastic. The vapour bubbles were produced using compressed air supplied to the sparger. One of three rotameters were used to cover a wide range of airflow rates. After lifting the liquid, the compressed air was released through a small opening provided at the top of the separator tank. A constant level of the water was maintained in the reservoir tank by a separate water supply together with an overflow drainage. The reservoir tank was placed on an adjustable stand that could be fixed at different vertical positions to provide a variable and controllable submergence ratio. The flow regimes were observed and recorded by a high-speed digital camera.

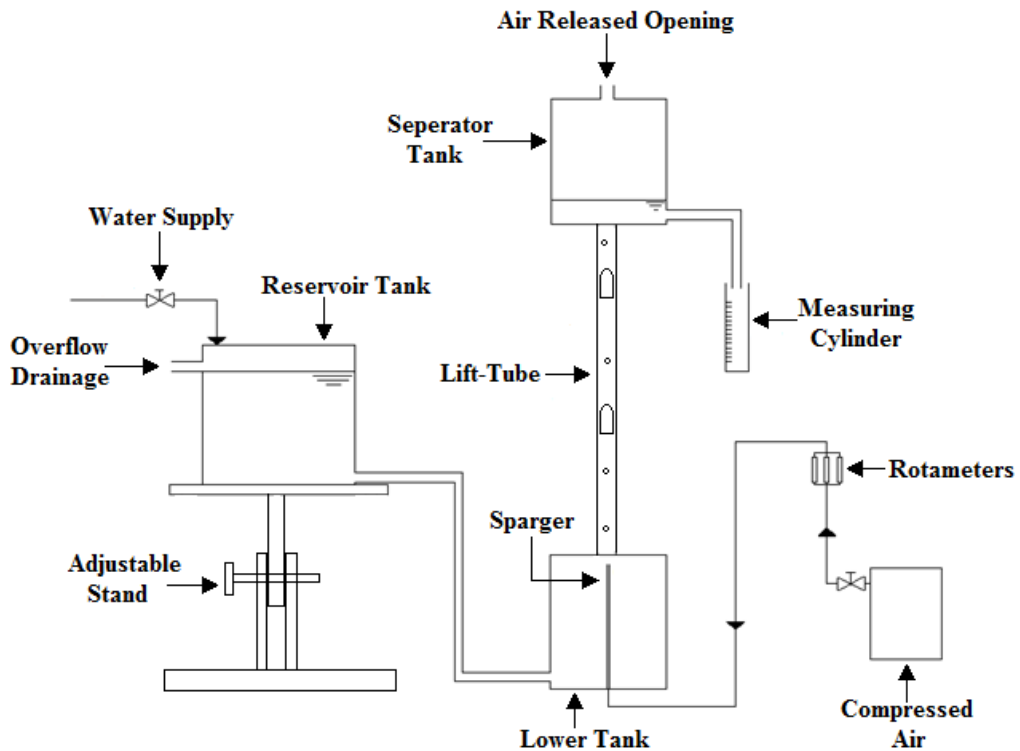


**Figure 27:** Schematic of the experimental setup

For this experimental study, 500 mm long lift-tubes were used, with inner diameters of 10 and 14 mm. These were tested separately in order to analyse the influence of the lift-tube diameter on the performance of the bubble pump. In order to analyse the formation of different flow regimes, the airflow rate was varied between 0.05 to 50 litre/min and the submergence ratios were set at 0.3, 0.5, and 0.7.

## 4.3 Experimental results

### 4.3.1 Flow visualization

The experiment started by investigating the flow characteristics and types of flow regimes in an airlift pump. The initial choice of parameters included a lift-tube diameter of 10 mm and submergence ratio of 0.5. It was observed that for very low airflow rates (0.05 to 0.4 litre/min); discrete spherical shaped vapour bubbles are dispersed in the liquid phase as shown in Figure 28. As such, this flow regime is termed as a bubbly flow regime (Samaras and Margaris, 2005).

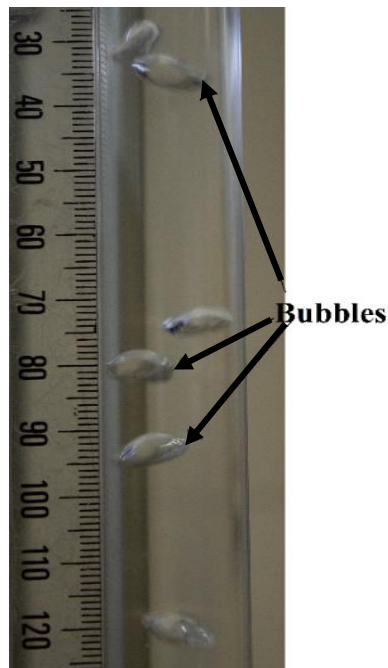


**Figure 28:** Bubbly flow regime

During this flow regime, the individual bubbles rise to the top of the liquid surface; however, no liquid was lifted at this flow regime, as the drag force of the bubbles on the liquid was not enough to move the liquid. As the airflow rate was increased (greater than 0.4 litre/min), the vapour bubbles start to combine and result in small cap-shaped bubbles appearing, indicating a transition of the flow regime.

As shown in Figure 29, these cap-shaped bubbles move upward forming a train of bubbles, which were able to move the liquid. However, to initiate the flow of the liquid, the train bubbles were not able to lift the liquid to the required lift height. Further increasing the airflow rate (0.5 to 4.8 litre/min), the small cap-shaped bubbles coalesce forming bullet-shape bubbles called Taylor bubbles (Pringle et al. 2015), which lift the liquid upwards to the required lift height.



**Figure 29:** Bubble train comprising of small air slugs



These Taylor bubbles as shown in Figure 30 are characterised by a hemi-spherical nose and a cylindrical tail and are essentially axi-symmetric. The diameter of these bubbles almost equals the lift-tube diameter, while their length varies depending upon the vapour flow rate. In between the Taylor bubbles is the liquid mass, known as liquid-slug. Since both phases move as individual slugs, this flow regime is termed slug flow.

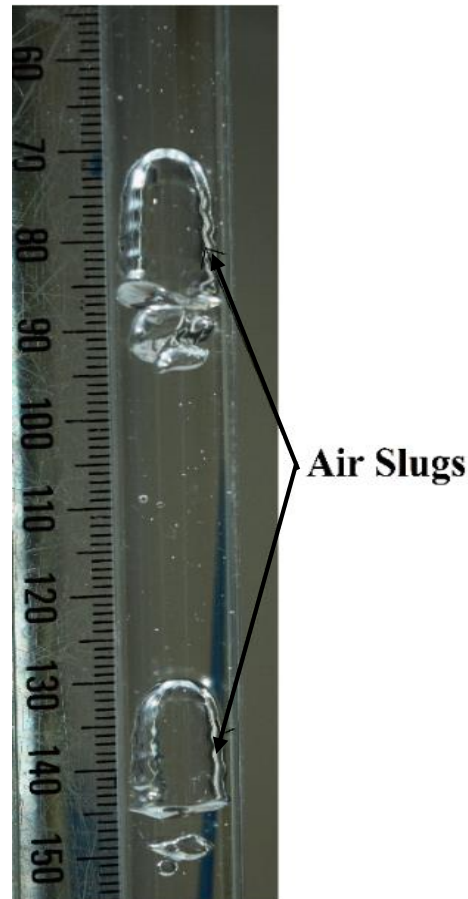


**Figure 30:** Taylor bubbles in a slug flow regime

In the slug flow regime, liquid moves by buoyancy forces acting on the liquid trapped between successive Taylor bubbles. It was observed that the operation of the slug flow regime involves a cyclic phenomenon of small air-slugs followed by a big air-slug carrying slugs of liquid as they move upwards. This observation agrees with the results reported by Kassab et al. (2009).

During the lifting of the liquid-slugs a small portion of the liquid-slug flows downwards as a continuous film between the bubble surface and the lift-tube wall. As the liquid flows down, it meets with the downward liquid-slug and leads to increased vorticity (Delfos et al., 2001). Due to this vorticity, some air is sheared away from the bottom surface of the bubble, which tends to aerate the downstream liquid slug. As the airflow rate was increased beyond a critical value (in this case 4.8 litre/min), the air-slugs became elongated and are sheared. As such, the air-slugs failed to maintain their shape and stability, resulting in the destruction of the air-slugs as shown in Figure 31. This represented the transition of the flow from the slug to churn flow regime.

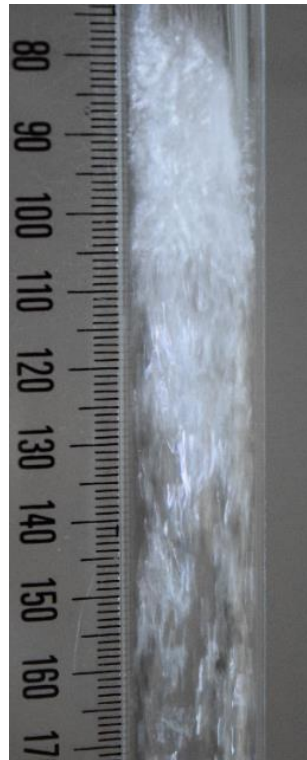


**Figure 31:** Unstable churn flow regime

As the air-slug breaks, the liquid on top of the air-slug falls, and is lifted again by the next air-slug. This causes repeated oscillation of large liquid lumps inside the lift-tube.

As such, churn flow regimes can be characterised as being highly chaotic where the flow seen to move up and down at different intervals (Shaban and Tavoularis, 2014).

Now, at very high airflow rates (greater than 10 litre/min), it was observed that the air starts to form a column through the centre of the lift-tube from top to the bottom. As such, a thin liquid film was formed between the inner lift-tube wall and the air column. This caused the formation of the annular flow regime (Kim et al. 2014) as shown in Figure 32. In the annular flow regime, the vapour velocity is greater than the liquid phase velocity. Due to this, the air tends to shear the liquid film resulting in the entrainment of very small liquid droplets within the vapour core. It was found that a very small amount of liquid was pumped when the bubble pump was operating in the annular flow regime.

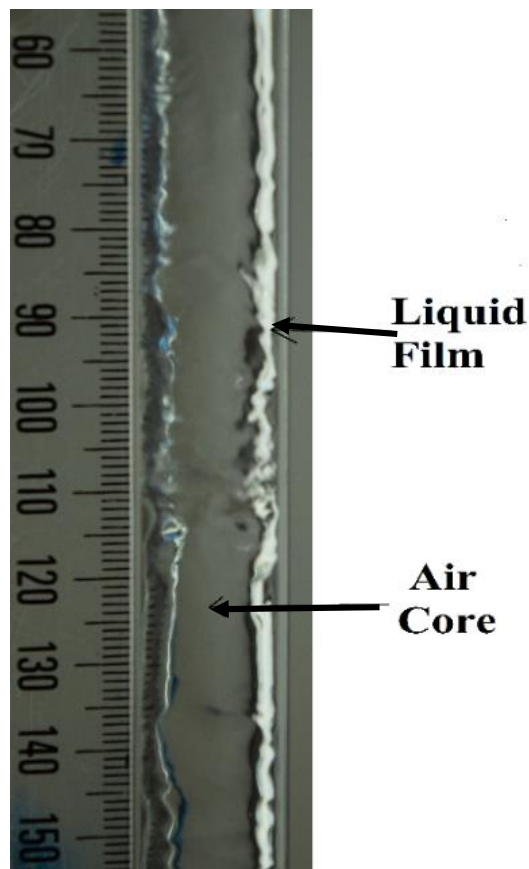


**Figure 32:** Annular flow regime

Based on the observations, the performance of the bubble pump and the boundaries between the flow regimes are shown in Figure 33.

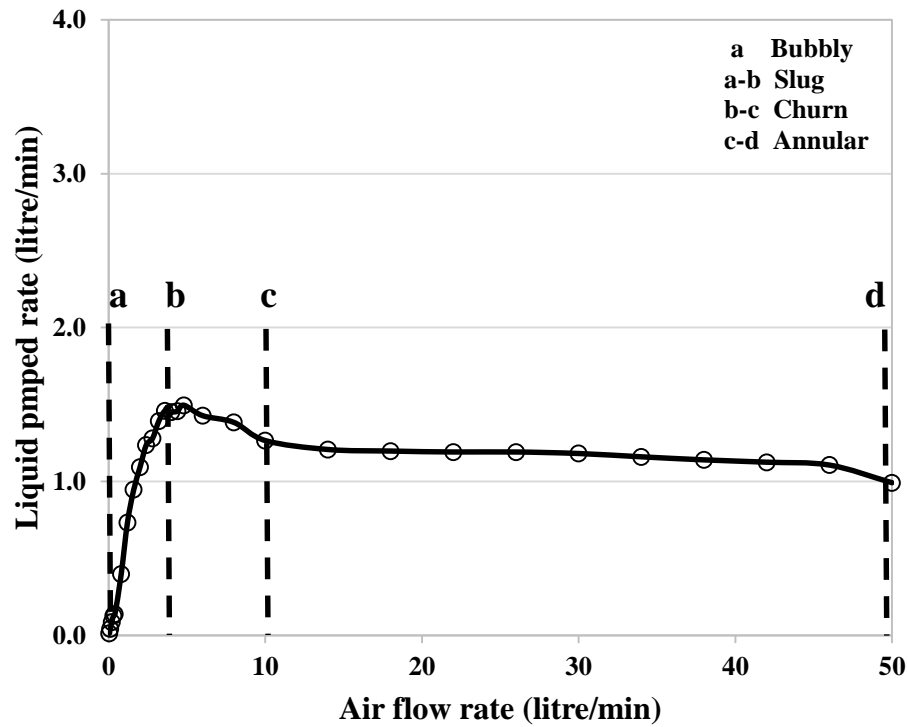


**Figure 33:** Flow regime visualisation and performance of a 10 mm lift-tube airlift pump at submergence ratio of 0.5

It can be seen that no liquid was pumped during the bubbly flow regime (Point a). As the flow regime changes from bubbly to slug, the performance of the bubble pump continuously improves until it reaches its maximum at the transition region (Point b) of slug to churn flow regime. It was found that at the transition from slug to churn flow regime, the maximum amount of the liquid was pumped. Due to the chaotic nature of the churn flow regime, the performance of the bubble pump decreases with an increase in the airflow rate. Further increasing the airflow rate (Point c), the flow regime changes to annular flow regime and the amount of the liquid pumped by the bubble pump tends to remain constant. This is similar to the observations of Tighzert et al. (2013).

### 4.3.2 Influence of the submergence ratio

The performance of the pump was evaluated at submergence ratios of 0.3, 0.5, and 0.7. For this, tests were conducted on lift-tubes having diameters of 10 mm and 14 mm respectively. As such, Figure 34 shows the influence of the submergence ratio on the performance of the bubble pump having lift-tube diameter of 10 mm.

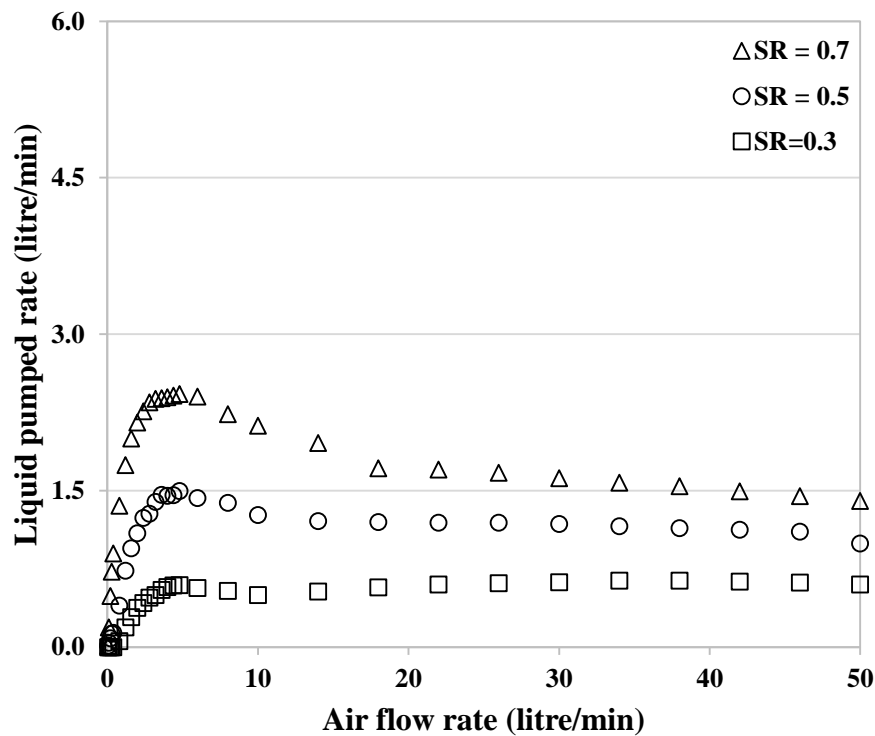


**Figure 34:** Performance of 10 mm lift-tube airlift pump at different values of submergence ratio

Increasing the submergence ratio reduces the lift height required to pump the liquid. It was found that by increasing the submergence ratio more liquid was pumped by the bubble pump. At low values of submergence ratio, i.e. 0.3, the bubble pump was not able to pump the liquid at very low airflow rates (0.05 to 1 litre/min), as the buoyancy force exerted by the bubbles was not enough to lift the liquid to the required liquid height.

The influence of the submergence ratio was also examined by increasing the diameter of the lift-tube to 14 mm as shown in Figure 35. It was found that both the 10 mm and 14 mm lift-tube diameter bubble pump follow the same trend i.e. increasing the submergence ratio improves the pumping performance.

However, for both 10 mm and 14 mm lift-tube diameters, it was found that at low submergence ratios the performance of the bubble pump improved at high airflow rates. This is due to the presence of the annular flow regime in which a thin film of liquid surrounds the inner wall of the lift-tube. As the airflow rate is increased, more water is sheared away from the thin film resulting in the improved performance.

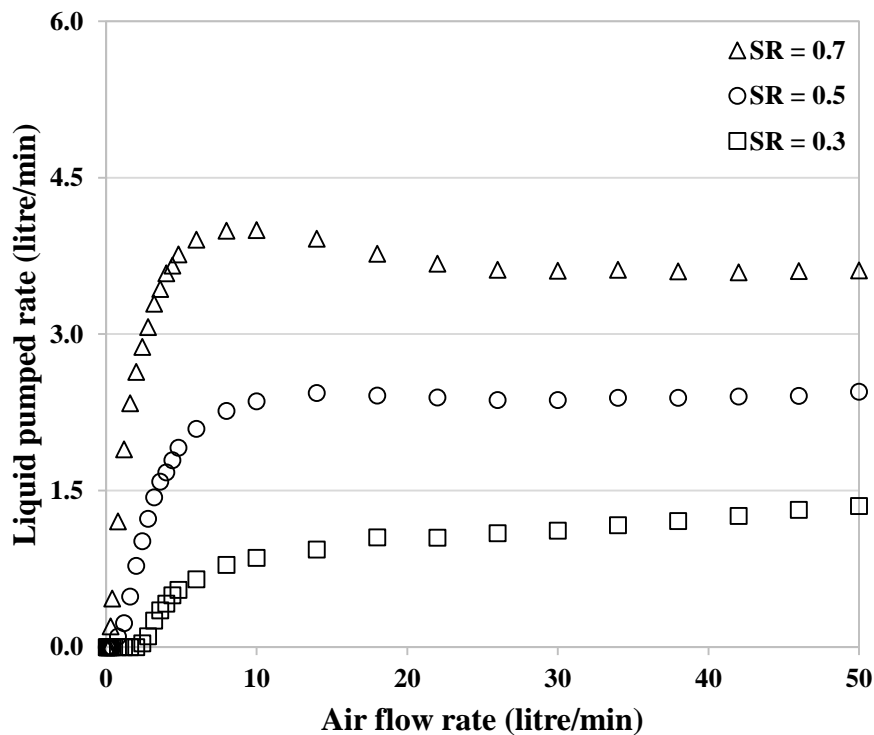


**Figure 35:** Performance of 14 mm lift-tube airlift pump at different values of submergence ratio

### 4.3.3 Influence of the lift-tube diameter

Figures 36 to 38 shows the effect of the lift-tube diameter on the performance of bubble pump operating at submergence ratio of 0.3, 0.5 and 0.7. It was found that for all the values of the submergence ratio, the pumping capacity of the 10 mm diameter lift-tube was found to be higher at low airflow rates; however, the pumping capacity of the 14 mm diameter lift-tube improves significantly, as the pumping capacity of the 10 mm diameter lift-tube drops. At low airflow rates the slug flow regime forms early in the 10 mm diameter lift-tube as compared to 14 mm lift-tube diameter this results in a higher pumping capacity of the 10 mm lift-tube bubble pump.

Also, in order to initiate the pumping effect in a 14 mm diameter lift-tube, more airflow rate was required. This is because gravitational forces increase with the lift-tube diameter. To overcome this, the bubbles will exert more buoyancy force, which is achieved by increasing the airflow rate.

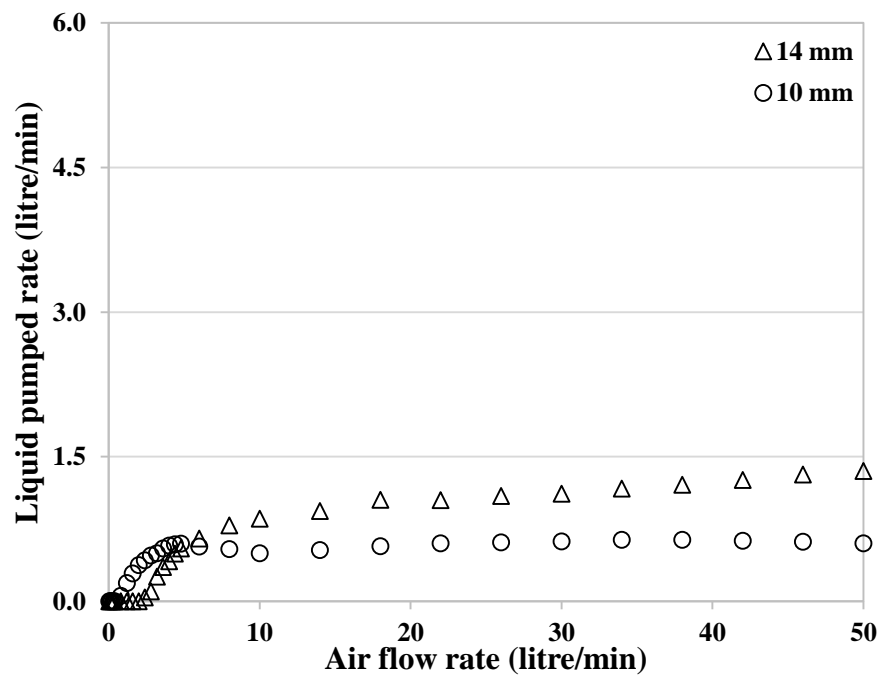


**Figure 36:** Influence of lift-tube diameter on the performance of airlift pump at submergence ratio of 0.3

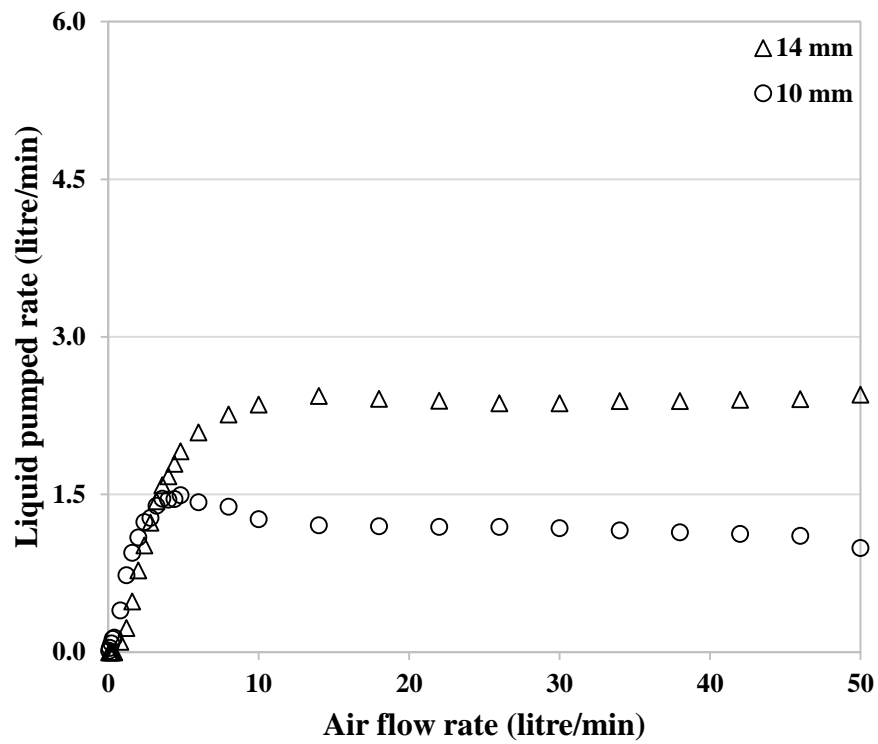


**Figure 37:** Influence of lift-tube diameter on the performance of airlift pump at submergence ratio of 0.5

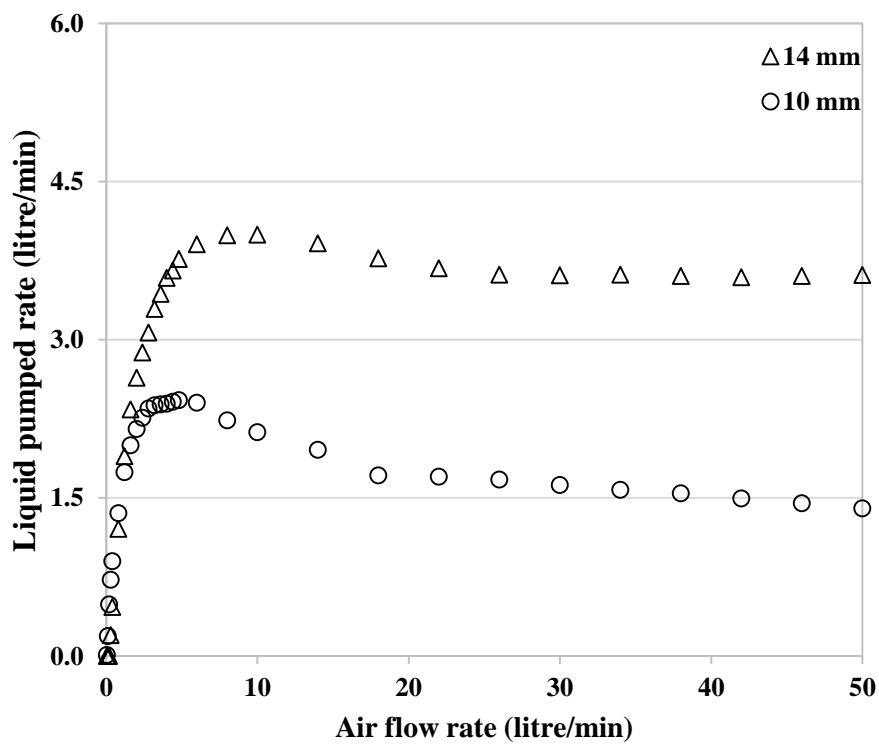


**Figure 38:** Influence of lift-tube diameter on the performance of airlift pump at submergence ratio of 0.7



In addition, the occurrence of the slug flow regime, which is the most efficient flow regime, is extended in the 14 mm lift-tube as compared to 10 mm lift-tube. This extended occurrence of slug flow regime in the 14 mm lift-tube delays the emergence of the churn flow regime, which results in an improved pumping performance in 14 mm lift-tube as compared to the 10 mm lift-tube.

#### 4.4 Flow regime map

In the experimental investigation, different distributions of two-phase flow regime were observed inside the lift-tube. As such, it is important to know which distribution will exist under a particular operating condition. The conventional way of representing the range of the flow regimes under a wide variety of operating conditions is by a flow regime map.

In order to build a flow regime map, it is necessary to choose the coordinates of the flow regime map. In this regard, a large number of coordinates have been proposed. In their study, Taitel and Bornea (1980) mention two basic types of coordinate systems, dimensional and dimensionless. Taitel and Bornea (1980) mentioned that the most common dimensional coordinates that have been used are superficial velocities  $J_G$  and  $J_L$  (Sterling 1965, Wallis 1969, Hanafizadeh et al. 2011a), or superficial momentum flux  $\rho_G J_G^2$  and  $\rho_L J_L^2$  (Hewitt and Roberts, 1969). That said, Griffith and Wallis (1961) have used  $J^2/gD$  and  $J_G/J_L$  as the dimensionless coordinates in their study. However, most researchers (Hanafizadeh et al. 2011b, Situ et al. 2011, Schlegel et al. 2009, Chen et al. 2005) have used dimensional coordinates to build their flow regime map.

The most common dimensional coordinates for gas liquid two-phase flow are the superficial velocities of the two-phases, which was adopted for this study, in order to build a flow regime map. The superficial velocity of a particular phase is the ratio between the flow rate of the particular phase and the area of the lift-tube.

Figure 39 shows the flow regime map and the flow regime transitions observed during the experimental study. The four main types of the flow regimes i.e. bubbly, slug, churn, and annular are depicted in the proposed flow regime map.

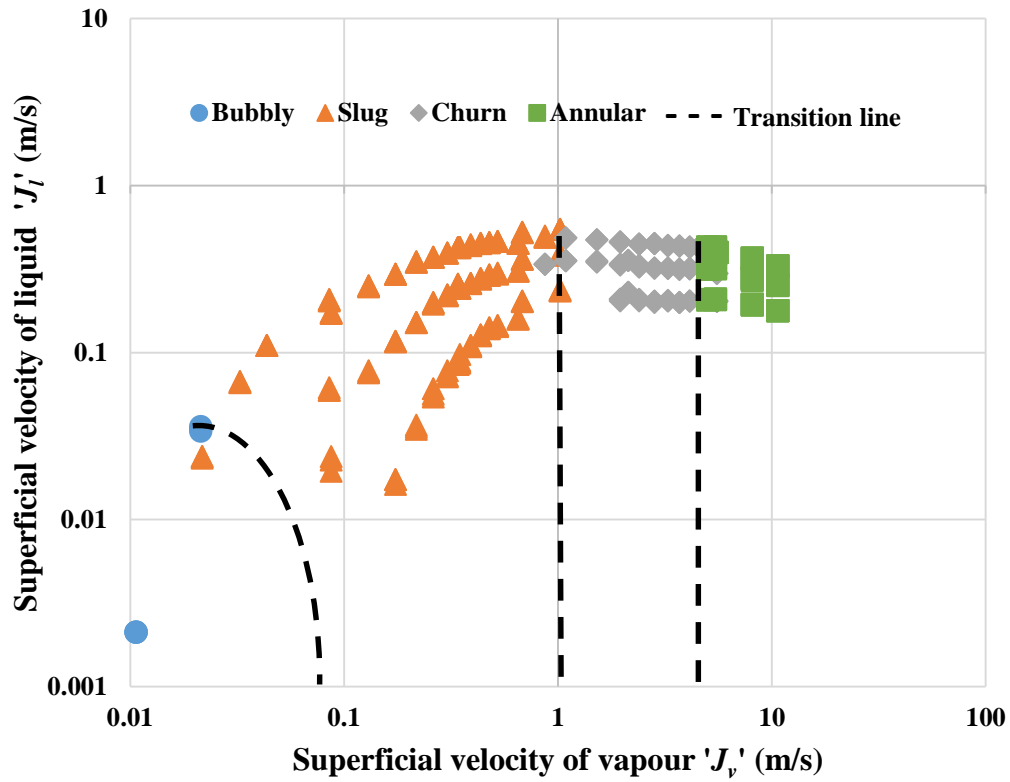


**Figure 39:** Experimental flow regime map

It was found that a particular flow regime occurs under a certain range of the superficial velocity of the air as shown in Table 5, which provides a good estimation to predict the flow regimes in the lift-tube.

**Table 5:** Superficial velocity of air for different flow regimes

Flow Regime	Superficial velocity of air ' $J_v$ ' (m/s)
Bubbly	Up till 0.05
Slug	0.05 – 1.00
Churn	1.00 – 7.00
Annular	7.00 and onwards

## 4.5 Bubble pump model

Having analysed the pumping phenomena of the airlift pump and the boundaries for different flow regimes, a model of the bubble pump based on momentum and continuity equation was developed. The theoretical method of White (2001) was used as a starting point to setup the relationships between the model parameters.

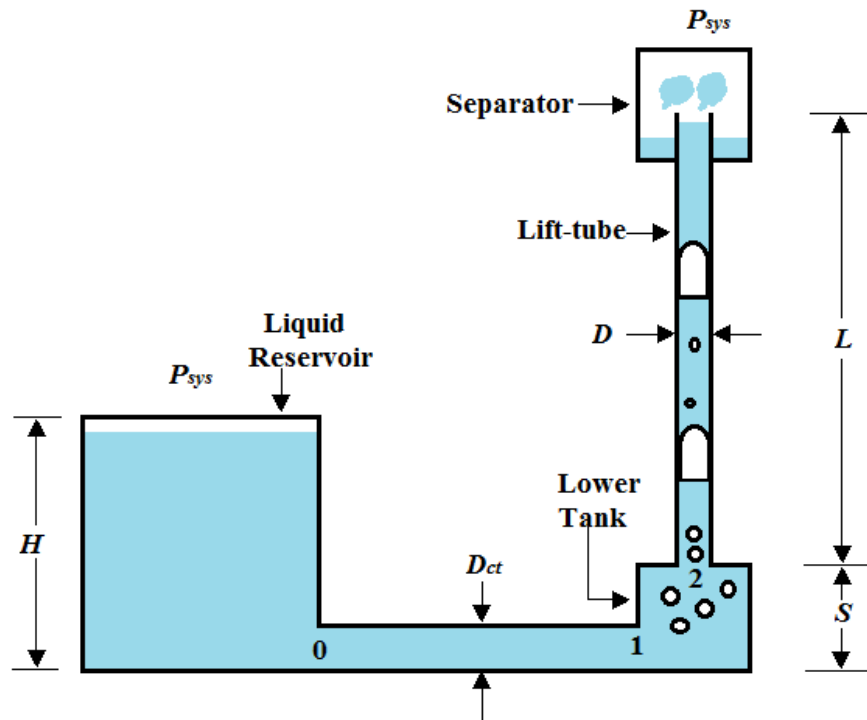
**Figure 40:** Schematic of a bubble pump

Figure 40 shows a schematic of the bubble pump consisting of a vertical lift-tube, lower tank, separator and a liquid reservoir. Initially, with no pumping, the height of the liquid

in the lift-tube is equal to that of the liquid in the reservoir. Since a DAR system is a single pressure system, therefore the pressures at the surface of the liquid in the reservoir and at the exit of the bubble pump were taken as constant. The relationship between the fluid pressure and the velocity at the exit of the liquid reservoir i.e. at point 0 can be determined by applying Bernoulli's equation from  $P_{sys}$  to 0 and is given by Equation 31:

$$\frac{P_{sys}}{\rho_l g} + \frac{V_{sys}^2}{2g} + Z_{sys} = \frac{P_0}{\rho_l g} + \frac{V_0^2}{2g} + Z_0 \quad (31)$$

In Equation 31,  $P_{sys}$ ,  $P_0$ ,  $V_{sys}$  and  $V_0$  are the pressures and velocities at the liquid surface and at the exit of the liquid reservoir,  $Z_{sys}$  is the height of the liquid in the reservoir which is equal to  $H$ ,  $Z_0$  is the level of the reservoir exit which is taken as zero,  $\rho_l$  is the density of the liquid, and  $g$  is the acceleration due to gravity. Since in the DAR system the submergence ratio of the bubble pump remains constant, therefore in the model the liquid level in the reservoir was kept constant. The velocity of the liquid at the reservoir level is very small and is assumed to be zero. This results in Equation 32:

$$P_0 = P_{sys} + H\rho_l g - \frac{V_0^2 \rho_l}{2} \quad (32)$$

By applying the rate of change of momentum from 0 to 1, Equation 33 is derived and is given by:

$$P_1 = P_{sys} + H\rho_l g - \frac{V_0^2 \rho_l}{2} - \rho_l V_1 (V_1 - V_0) \quad (33)$$

Since the mass flow rate of the liquid from point 0 to 1 is constant, the liquid velocity at these points is same and is given by Equation 34:

$$V_0 = V_1 \quad (34)$$

The constant liquid velocity results in Equation 35:

$$P_1 = P_{sys} + H\rho_l g - \frac{V_0^2 \rho_l}{2} \quad (35)$$

The conservation of momentum is applied in the lower tank, which yields Equation 36:

$$P_2 = P_1 - \rho_l V_1 (V_2 - V_1) - \rho_l g S \quad (36)$$

In Equation 36,  $P_2$  and  $V_2$  are the pressure and velocity at the exit of the lower tank, while  $S$  is the height of the lower tank.

Combining Equation 35 and Equation 36, results in Equation 37:

$$P_2 = P_{sys} + H\rho_l g - \frac{V_1^2 \rho_l}{2} - \rho_l V_1 (V_2 - V_1) - \rho_l g S \quad (37)$$

The pressure loss in the lift-tube can be determined by applying the momentum equation from point 2 to  $P_{sys}$  as shown in Equation 38:

$$P_2 = P_{sys} + \frac{f_{TP} \rho_h V_2^2}{2} \left( \frac{L}{D} \right) + \frac{W_l}{A} \quad (38)$$

In Equation 38,  $\rho_h$  is the homogenous density of the two-phase flow inside the lift-tube,  $L$  is the length of the lift-tube,  $D$  is the diameter of the lift-tube,  $A$  is the area of the lift-tube,  $W_l$  is the weight of the liquid inside the lift-tube, and  $f_{TP}$  is the two-phase friction factor. The homogenous density ( $\rho_h$ ) can be obtained by applying the continuity equation between point 1 and 2, as shown in Equation 39:

$$\rho_l A_1 V_1 = \rho_h A_2 V_2 \quad (39)$$

Rearranging Equation 39 yields Equation 40:

$$\rho_h = \frac{\rho_l A_1 V_1}{A_2 V_2} \quad (40)$$

In Equation 40,  $\rho_l$  is the density of the liquid at point 1,  $\rho_h$  is the homogenous density of the two-phase flow at point 2,  $A_1$  is the inlet area of the lower tank, and  $A_2$  is the exit area of the lower tank. The weight of the liquid ( $W_l$ ) inside the lift-tube is given by Equation 41:

$$W_l = \rho_l A_l L g \quad (41)$$

In Equation 41,  $A_l$  is the cross-sectional area of the liquid inside the lift-tube. By putting the relationship for  $W_l$  in to Equation 38 results in Equation 42:

$$P_2 = P_{sys} + \frac{f_{TP} \rho_h V_2^2}{2} \left( \frac{L}{D} \right) + \frac{\rho_l A_l L g}{A} \quad (42)$$

Combining Equations 38 and 42 and solving yields Equation 43:

$$\frac{H - S}{L} = \frac{f_{TP} V_2^2 \rho_h}{2 g D \rho_l} + \frac{V_1^2}{2 g L} + \frac{V_1 (V_2 - V_1)}{g L} + \frac{A_l}{A} \quad (43)$$

The total inlet area of the lift-tube is occupied both by the liquid and vapour phases. As such, the total inlet area of the lift-tube is given by Equation 44:

$$A = A_l + A_v \quad (44)$$

In Equation 44,  $A_v$  is the area occupied by the vapour in the lift-tube. Dividing Equation 44 by the total area ( $A$ ), results in Equation 45:

$$1 = \frac{A_l}{A} + \frac{A_v}{A} \quad (45)$$

For a two-phase flow inside a lift-tube, the ratio of the area occupied by the gas to the total area is termed the void fraction ( $\varepsilon$ ), which is given by Equation 46:

$$\varepsilon = \frac{A_v}{A} \quad (46)$$

Therefore, by putting the relationship for the void fraction in Equation 45, results in Equation 47:

$$\frac{A_l}{A} = 1 - \varepsilon \quad (47)$$

The velocity of a two-phase flow at point 2 can be estimated by dividing the total flow rate with the total area and is given by Equation 48:

$$V_2 = \frac{\dot{V}_l + \dot{V}_v}{A} \quad (48)$$

In Equation 48,  $\dot{V}_l$  and  $\dot{V}_v$  are the volume flow rate of liquid and vapour at point 2. Now, in two-phase flow it is difficult to estimate the area occupied by each phase as it depends upon their interfacial distribution, which is difficult to estimate. As such, the velocities of each phase in the two-phase flow can be defined in terms of a superficial velocity, which is the ratio between the flow rate of the particular phase and the total area of the lift-tube. Therefore, the superficial velocity of liquid ( $J_l$ ) and vapour ( $J_v$ ) phase are given by Equations 49 and 50 respectively:

$$J_l = \frac{\dot{V}_l}{A} \quad (49)$$

$$J_v = \frac{\dot{V}_v}{A} \quad (50)$$

The total superficial velocity ( $J^*$ ) of both the phases is the sum of their individual superficial velocity and is given by Equation 51:

$$J^* = J_l + J_v \quad (51)$$

Putting the expressions of the superficial velocities of the liquid and vapour phase in Equation 51 yields Equation 52:

$$J^* = \frac{\dot{V}_l + \dot{V}_v}{A} \quad (52)$$

Comparing Equations 48 and 52 yields Equation 53:

$$V_2 = J^* \quad (53)$$

The velocity of liquid at point 1 is given by Equation 54:

$$V_1 = \frac{\dot{V}_l}{A_0} \quad (54)$$

Also, the velocity of the liquid at point 1 in terms of the superficial velocity is given by Equation 55:

$$V_1 = J_l \left( \frac{A}{A_0} \right) \quad (55)$$

By putting the relationship of Equations 47, 53 and 55 into Equation 43 gives the average pressure gradient along the lift-tube and is given by Equation 56:

$$\frac{H - S}{L} = \frac{f_{TP} J^{*2} \rho_h}{2gD\rho_l} + \frac{J_l^2 \left( \frac{A}{A_0} \right)^2}{2gL} + \frac{J_l \left( \frac{A}{A_0} \right) U^* - J_l \left( \frac{A}{A_0} \right)}{gL} + (1 - \varepsilon) \quad (56)$$

In order to evaluate the friction factor ( $f_{TP}$ ), Beattie and Whalley (1982) recommended the use of the Colebrook equation given by Equation 57:

$$\frac{1}{\sqrt{\dot{f}_{TP}}} = 3.48 - 4 \log_{10} \left[ 2 \frac{\varepsilon_R}{D} + \frac{9.35}{Re_{TP} \sqrt{\dot{f}_{TP}}} \right] \quad (57)$$



In Equation 57,  $D$  is the diameter of the lift-tube,  $\varepsilon_R$  is the roughness of the inner surface of the lift-tube,  $\dot{f}_{TP}$  is the fanning friction factor, and  $Re_{TP}$  is the two-phase Reynolds number.

The two-phase Reynolds number can be estimated using Equation 58(White, 2001):

$$Re_{TP} = \frac{(\rho_v J_v + \rho_l J_l)D}{\mu_{TP}} \quad (58)$$

In Equation 58,  $\mu_{TP}$  is the two-phase viscosity and can be estimated using Equation 59 (Starace and De Pascalis, 2013):

$$\mu_{TP} = \varepsilon_h \mu_v + \mu_l (1 - \varepsilon_h) (1 + 2.5 \varepsilon_h) \quad (59)$$

In Equation 59,  $\mu_v$  and  $\mu_l$  are the viscosities of the vapour and liquid phase and  $\varepsilon_h$  is the homogenous void fraction, which can be estimated using Equation 60 (Starace and De Pascalis, 2013):

$$\varepsilon_h = \frac{X}{X + \frac{\rho_l}{\rho_v} (1 - X)} \quad (60)$$

The fluid quality ( $X$ ), can be estimated using Equation 61:

$$X = \frac{\dot{m}_v}{\dot{m}_v + \dot{m}_l} \quad (61)$$

In Equation 61,  $\dot{m}_v$  and  $\dot{m}_l$  are the mass flow rates of the liquid and vapour phase. The Fanning friction factor  $\dot{f}_{TP}$  can be estimated using Equation 62:

$$\dot{f}_{TP} = \frac{f_{TP}}{4} \quad (62)$$

In Equation 62,  $f_{TP}$  is the Darcy friction factor.

## 4.6 Void fraction models

Now, in order to determine the pressure gradient across the lift-tube using Equation 56, the void fraction ( $\varepsilon$ ) needs to be estimated. In two-phase flow, the void fraction is an important parameter for understanding the dynamics of the flow as it describes the composition of the two-phases inside the lift-tube. The void fraction depends upon several factors such as the distribution of the two-phases, the flow rate of the two-phases, the physical properties of the two-phases, and the geometrical parameters of the lift-tube. In order to estimate the void fraction, several analytical models can be used (Kazi, 2012):

- Homogenous flow model
- Separated flow model
- Drift flux model

### 4.6.1 Homogenous flow model

In the homogenous flow model, it is assumed that the two-phases are mixed intimately with each other and are moving with the same velocity. As such, there is no slip between the two-phases and the entire flow manifests itself as a mixture with suitable average properties of both the phases (Awad and Muzychka, 2008). Hence, for a homogenous model the continuity, momentum, and energy equations of a single-phase model can be used and the properties of the single-phase be replaced with the mixture property.

However, due to the density difference, there will be a relative velocity between the two-phases. As such, the application of the homogenous flow model is limited to the

cases where the phase velocities are very high such as in the case of annular flow regime. At low phase velocities, such as in the cases of bubbly, slug, and churn flow regime, the predictions of the model will not be accurate if the effect of the relative velocities is not included in the homogenous flow model. Hence, it was decided not to use the homogenous flow model for predicting the void fraction.

#### **4.6.2 Separate flow model**

In a separate flow model, the two-phases are considered flowing individually, as such, the two-phases have separate continuity, momentum, and energy equations (Richter, 1983). Even though the two-phases are considered separately, interactions between the two-phases at the interface are considered, while estimating the void fraction. However, refined models are required to determine the interfacial properties (Ahn et al. 2015), which makes it difficult to accurately predict the void fraction using a separate flow model. As such, it was decided not to use the separate flow model for this study

#### **4.6.3 Drift flux model**

In order to improve the predictions of the homogenous model, the effect of the relative velocities is included by incorporating their effect in the homogenous model. Therefore, this improvement of the homogenous model is called the drift flux model, which incorporates the relative motion between the two-phases. Zuber and Findlay (1965) first proposed the drift flux model; however, many other authors such as Wallis (1969) and Ishii (1977) have contributed in the development of this model. Ishii (1977) reported that the drift flux model is most appropriate when there is a strong relative motion between the two-phases.

However, several other researchers (Hibiki and Ishii 2003, Woldesemayat and Ghajar 2007) suggest that the drift flux model could successfully predict the void fraction for the annular flow regime, if the effect of the change in flow regime is incorporated in the model. Due to the applicability of the drift flux model for all the flow regimes, it was decided to use the drift flux model for estimating the void fraction.

## 4.7 Estimation of the parameters of drift flux model

In order to estimate the void fraction, the drift flux model is given by Equation 63 (Bhagwat and Ghajar (2014)):

$$\varepsilon = \frac{J_v}{C_o(J_l + J_v) + V_{Vj}} \quad (63)$$

In Equation 63,  $C_o$  is the distribution parameter, which accounts for the non-uniformity of the flow and serves as a correction factor for the homogenous flow. The use of the distribution parameter recognizes the fact that there is a slip between the two-phases.  $J_l$  and  $J_v$  are the superficial velocities of the liquid and vapour phase respectively.  $V_{Vj}$  is the drift velocity and is defined as the difference between the vapour-phase velocity ( $V_v$ ) and the two-phase mixture superficial velocity ( $J^*$ ) and is given by Equation 64:

$$V_{Vj} = V_v - J^* \quad (64)$$

In order to determine the drift flux variables  $C_o$  and  $V_{Vj}$  a straight-line relationship is plotted between  $(J_v/\varepsilon)$  and  $(J_l + J_v)$ . As such, the slope of the line represents the distribution parameter and the y-intercept determines the drift velocity (Hibiki and Ishii, 2002). However, this method requires experimental determination of the void fraction.

## 4.8 Experimental method

Volume measurement is a standard method of determining the void fraction in which the volume occupied by each phase is determined. The most common and accurate technique of measuring the volume is the quick-close valve technique. As shown in Figure 41, in this technique a valve is placed on the lift-tube section in which the void fraction is to be measured. As the two-phase mixture flows through the lift-tube, the valve is quickly closed to isolate the section for which the void fraction is to be determined. Due to high density, the liquid phase settles and its volume is measured, while the remaining volume comprises the vapour phase.

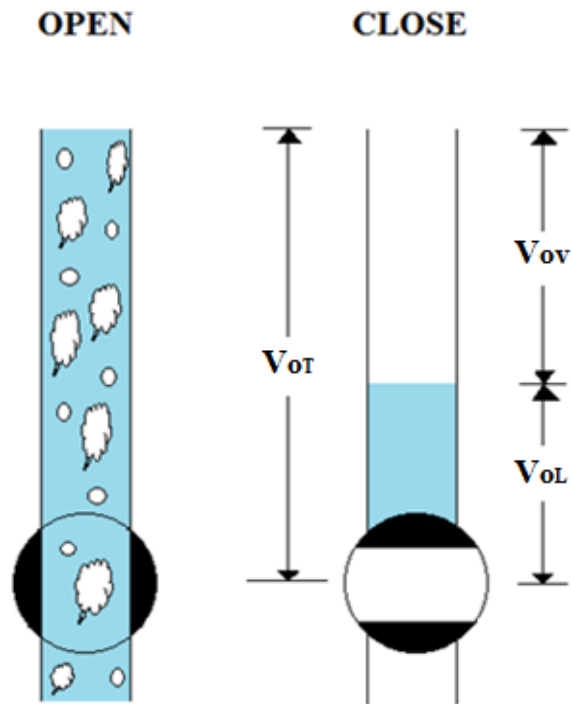


**Figure 41:** Schematic of the quick close valve technique

The void fraction is then calculated using Equation 65:

$$\varepsilon = \frac{V_{ov}}{V_{ov} + V_{oL}} \quad (65)$$

In Equation 65,  $Vo_v$  and  $Vo_l$  are the volumes of the gas and liquid in the lift-tube section, needed for the estimation of the void fraction.

Using the quick-closing valve technique, experiments were carried out for both the 10 mm and 14 mm lift-tubes under the submergence ratios of 0.3, 0.5, and 0.7. The experimental setup was same as described in Section 4.2. A valve was installed in the section of the lift-tube to estimate the void fraction. The airflow rate was varied between 0.05 to 50 litre/min to cover the wide range of the operating conditions. After obtaining the results, correlations were developed for the distribution parameter and drift velocity, based on the observed flow regimes as shown by Figures 42 to 45.

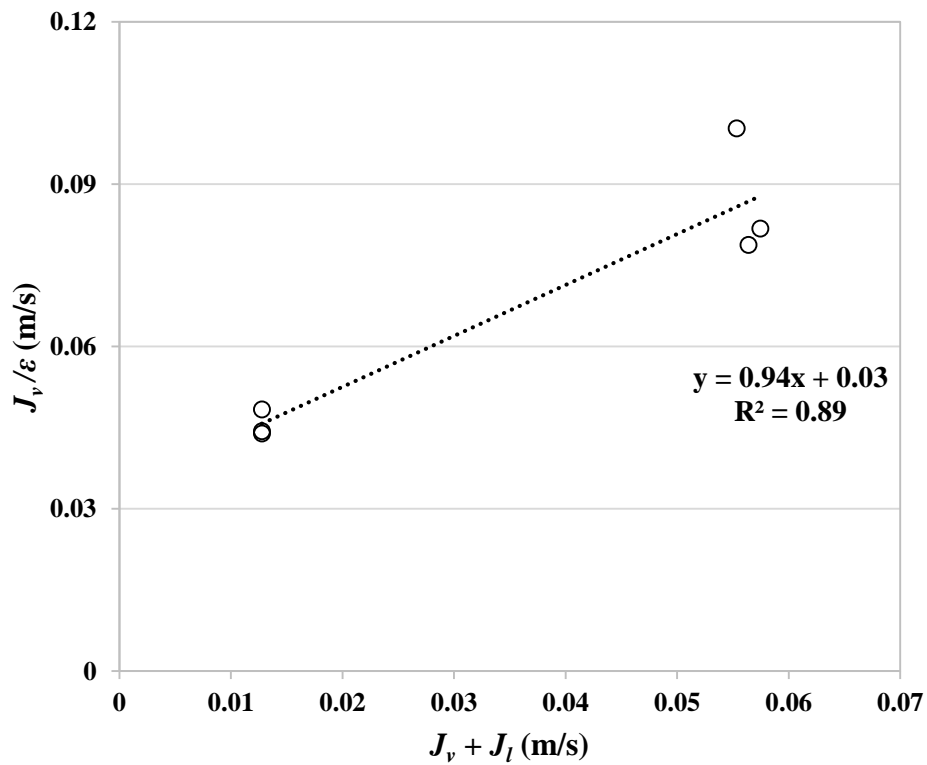


**Figure 42:** Correlation for bubbly flow regime

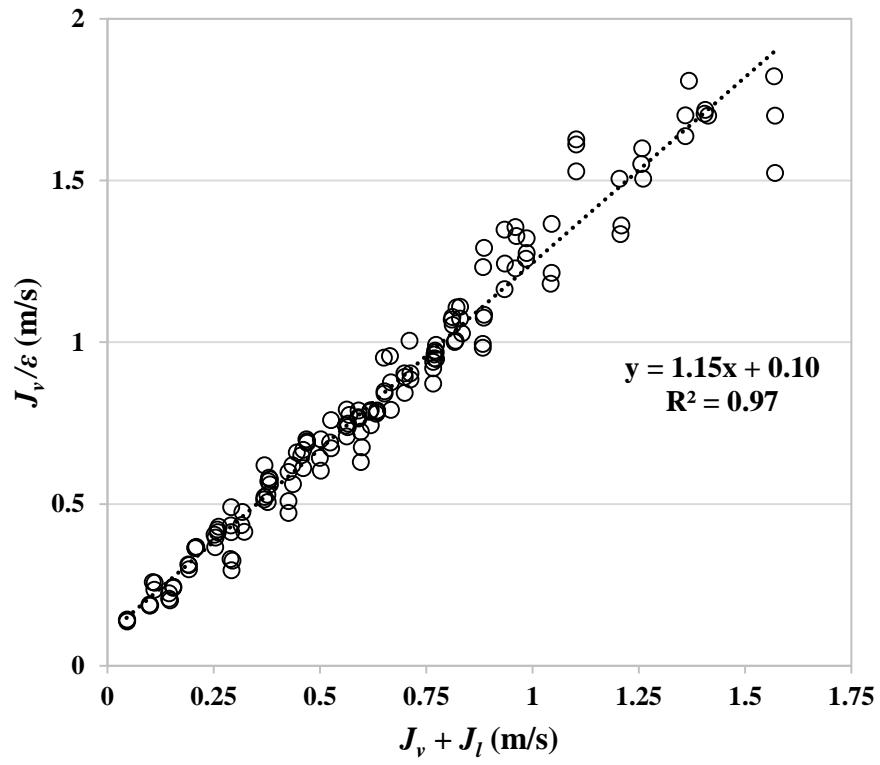


**Figure 43:** Correlation for slug flow regime

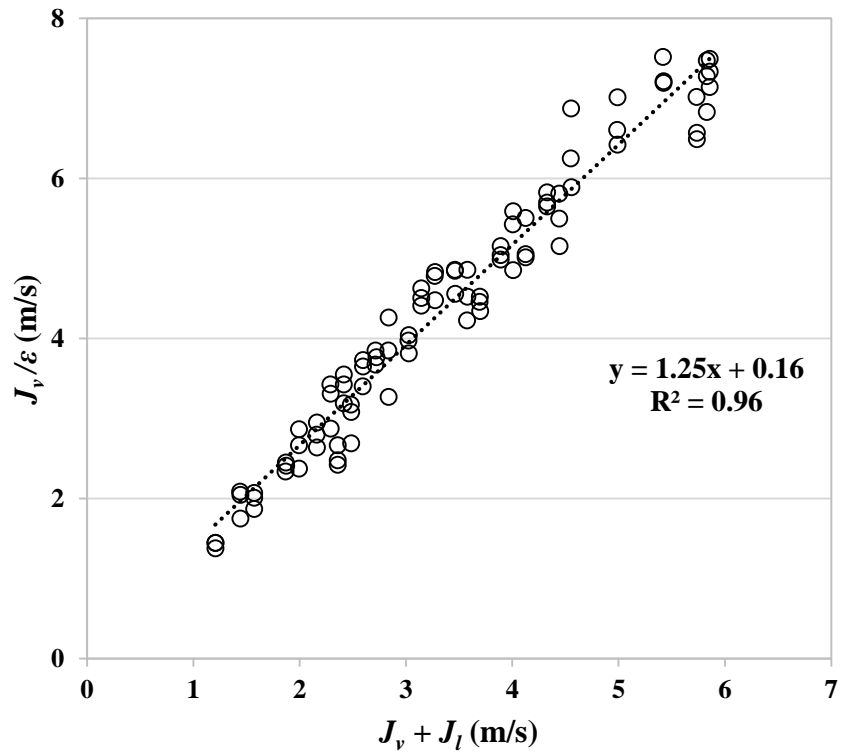


**Figure 44:** Correlation for churn flow regime





of annular flow regime the value of the distribution parameter approaches unity ( $C_o \rightarrow 1$ ). Hence, the values of the distribution parameter for each particular flow regime found from the experimental study agree well with the findings of Lahey (1974).

## 4.9 Comparison between model and experimental results

Having determined the flow regime specific values of the distribution parameter and drift velocity, the values were used to estimate the performance of the bubble pump using the model previously developed (Section 4.5). The predictions of the model were then compared with the experimental results. Figure 46 shows the comparison between the predicted and the experimental values for a bubble pump having the lift-tube diameter of 10 mm and operating at a submergence ratio of 0.7. It was found that the model agrees relatively well at low airflow rates (up to 4.0 litre/min). In this range of airflow, the bubble pump was operating in a slug flow regime.

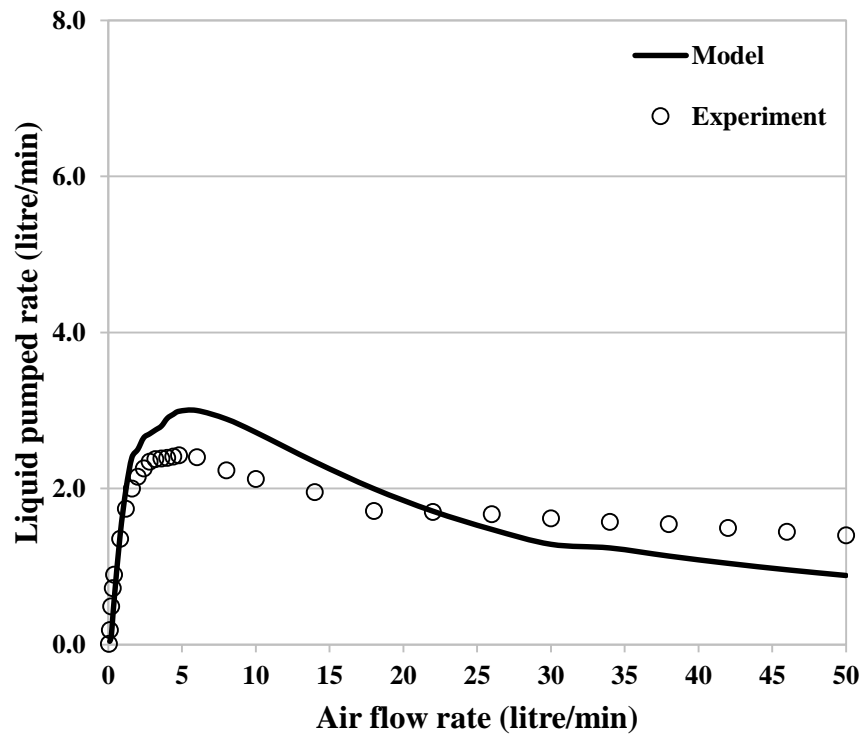


**Figure 46:** Performance comparison for 10 mm lift-tube at 0.7 submergence ratio

Further increasing the airflow rate over the range of 4.0 to 18 litre/min, the model tends to deviate from the experimental values due to the occurrence of the chaotic churn flow regime observed during the flow regime visualisation. At very high flow rates (greater than 18 litre/min), both the experimental and the model show a decrease in the pumping capacity due to the occurrence of the annular flow regime.

Now, for the same submergence ratio i.e. 0.7, the model and experiment were compared for the bubble pump having a lift-tube diameter of 14 mm as shown in Figure 47. It was found that the model agrees well over the range of airflow rates up to 3.0 litre/min. Further increasing the airflow rate the model tends to deviate away significantly in the churn flow regime from the experimental value due to the unstable nature of the churn flow regime.

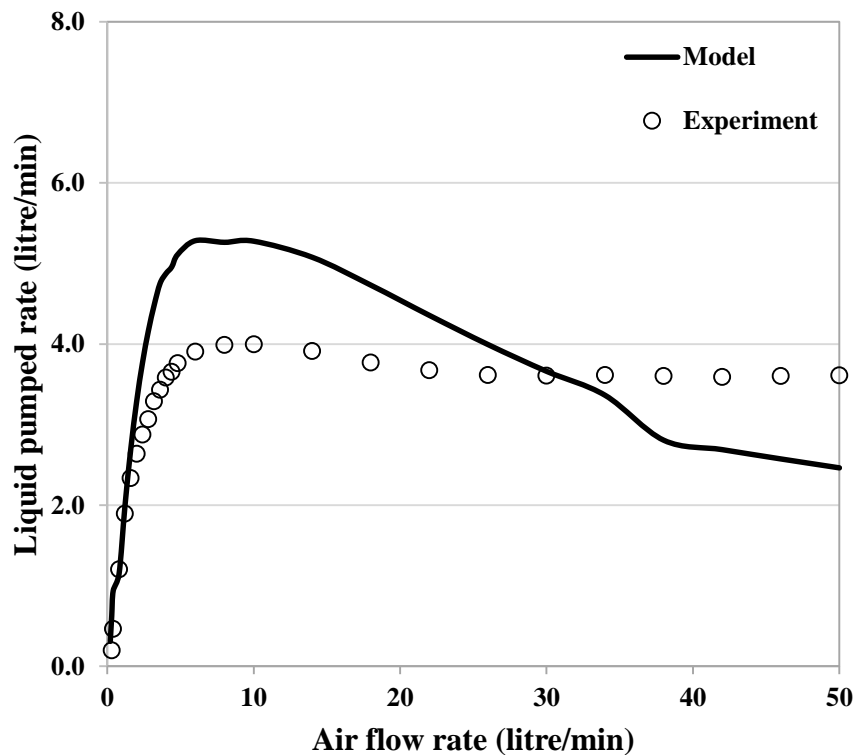


**Figure 47:** Performance comparison for 14 mm lift-tube at 0.7 submergence ratio

The model predictions of 10 mm and 14 mm diameter lift-tubes were compared with their experimental results at the submergence ratio of 0.5. Figure 48 shows the comparison between the model and experiment for a 10 mm lift-tube. A good agreement was found between the model and the experiment for airflow rates up to 4.0 litre/min. Further increase in the airflow rate does not deviates the model significantly. However, at very high airflow rates greater than 25 litre/min both the model and experiment deviates significantly from each other due to the occurrence of annular flow regime.

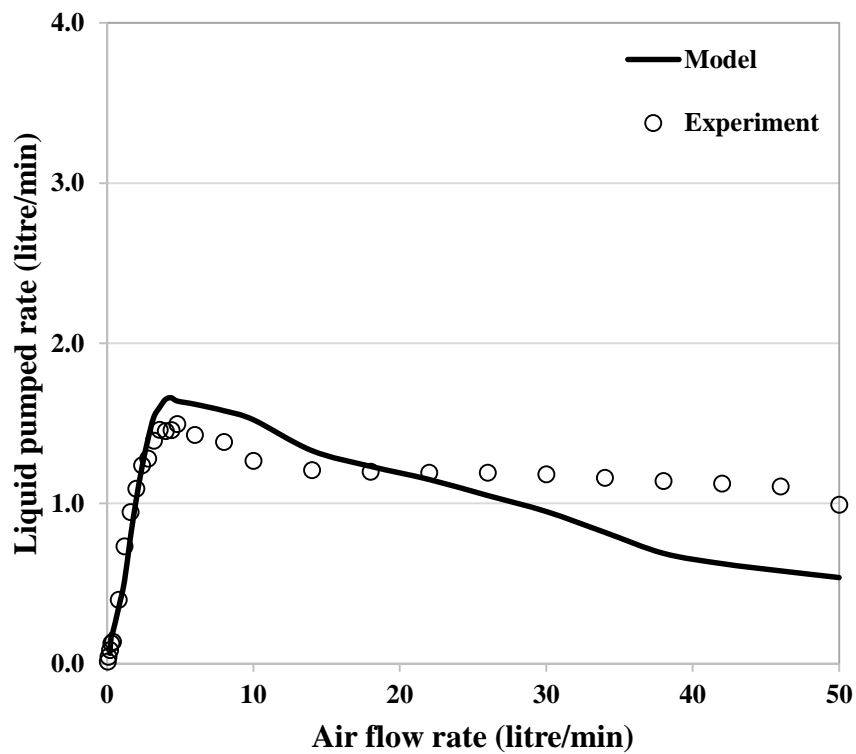


**Figure 48:** Performance comparison for 10 mm lift-tube at 0.5 submergence ratio

Figure 49 shows the comparison between the model and the experiment for a 14 mm diameter lift-tube. It was found that both the model and the experimental results agrees well over a range of airflow rates up to 25 litre/min. However, they tend to deviate as the airflow rate was further increased.

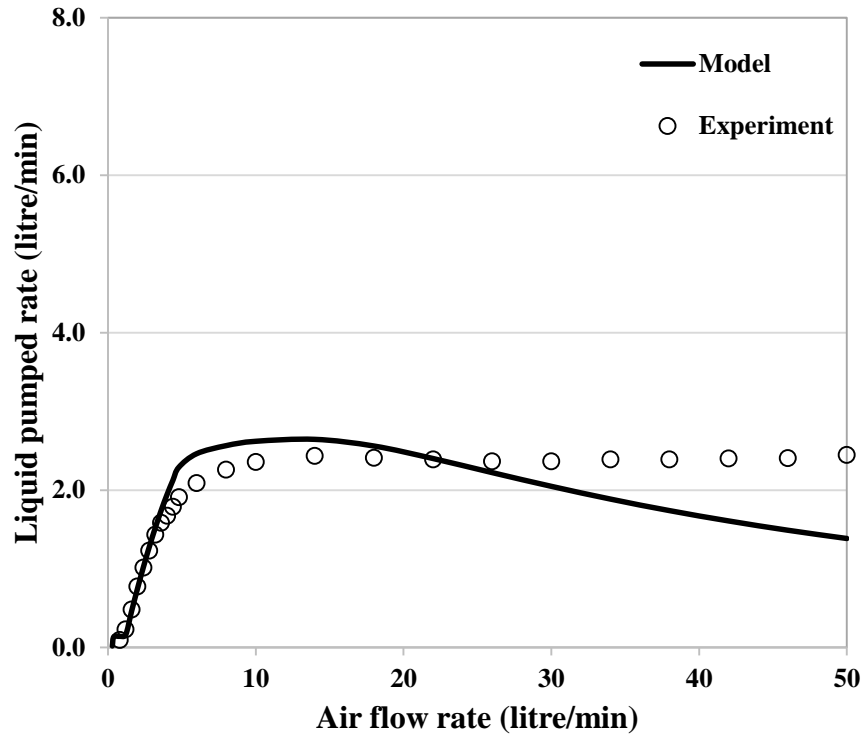


**Figure 49:** Performance comparison for 14 mm lift-tube at 0.5 submergence ratio

Now, for all the performance comparisons, it was found that the model agrees reasonably well with the results of the experiment up to the transition from a slug to churn flow regime. Beyond this point, the model showed deviation in the performance at high airflow rates. It was found that the model performed well at the submergence ratio of 0.5 where it showed low deviation from the experimental results. Furthermore, due to the chaotic nature of the churn flow regime, it was difficult to accurately estimate the performance of the bubble pump operating at churn flow regime.

#### 4.10 Performance of a heat driven bubble pump

Having verified the bubble pump model with an airlift pump system, the model was used to estimate the performance of a heat-driven bubble pump system using the empirical correlations of the drift velocity and the distribution parameter given in Table 6. Now, in an airlift pump system, the bubbles are formed by supplying compressed air

to the sparger; however, in a heat-driven bubble pump the addition of heat at the saturation temperature of the liquid generates vapour bubbles. The mass flow rate ( $\dot{m}_v$ ) of the vapour generated can be estimated by Equation 66:

$$\dot{m}_v = \frac{\dot{Q}_{gen}}{h_{fg}} \quad (66)$$

Where,  $\dot{Q}_{gen}$  is the heat added, at the saturation temperature of the liquid, and  $h_{fg}$  the enthalpy of vaporisation.

The estimated performance of the heat-driven bubble pump model was compared with the experimental results of An et al. (2017). In order to make the model comparable with the experimental investigation of An et al., the working fluid and the parameters were kept same. The working fluid used by An et al. was water and all the experimental readings were taken at atmospheric pressure, while the parameters used are given in Table 7.

**Table 7:** Parameters for the heat-driven bubble pump model

Parameter	Value
Lift-tube length (mm)	600
Lift-tube diameter (mm)	10
Submergence ratio	0.3, 0.4, 0.5
Heat Input (W)	120 - 600

Having formulated the heat driven bubble pump model, the predictions of the model was compared with the experimental results of An et al. as shown in Figures 50 to 52. It was found that for all the tests the trend of the curves for An et al. experiment and the model were similar. However, at heat inputs greater than 400 W, the model deviates from the experimental results and the pumping rate decreases, which can be attributed to the changing flow regime.

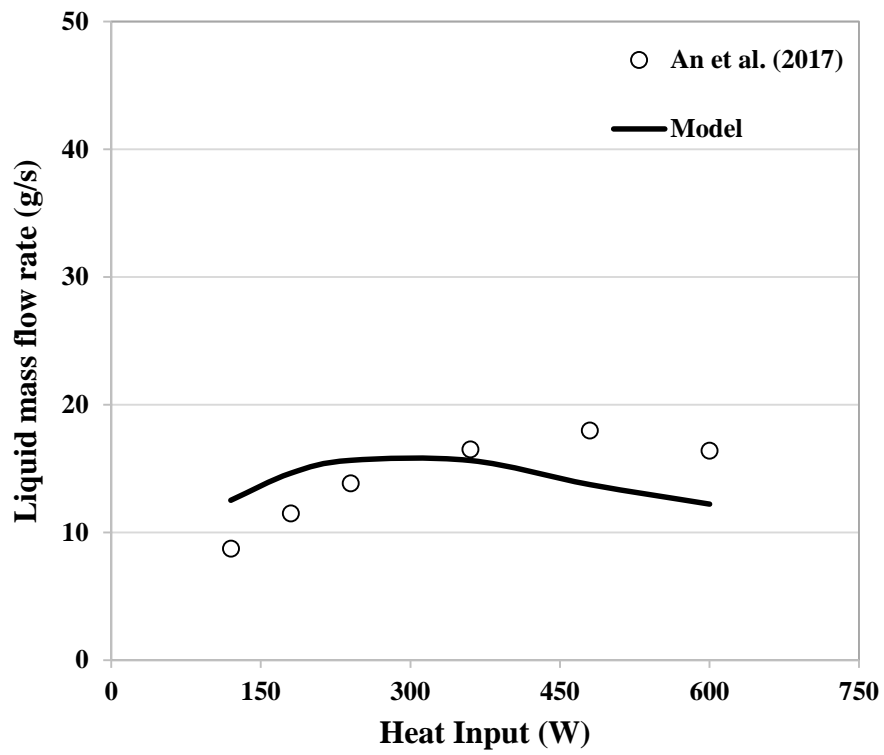


**Figure 50:** Performance comparison for the submergence ratio of 0.3

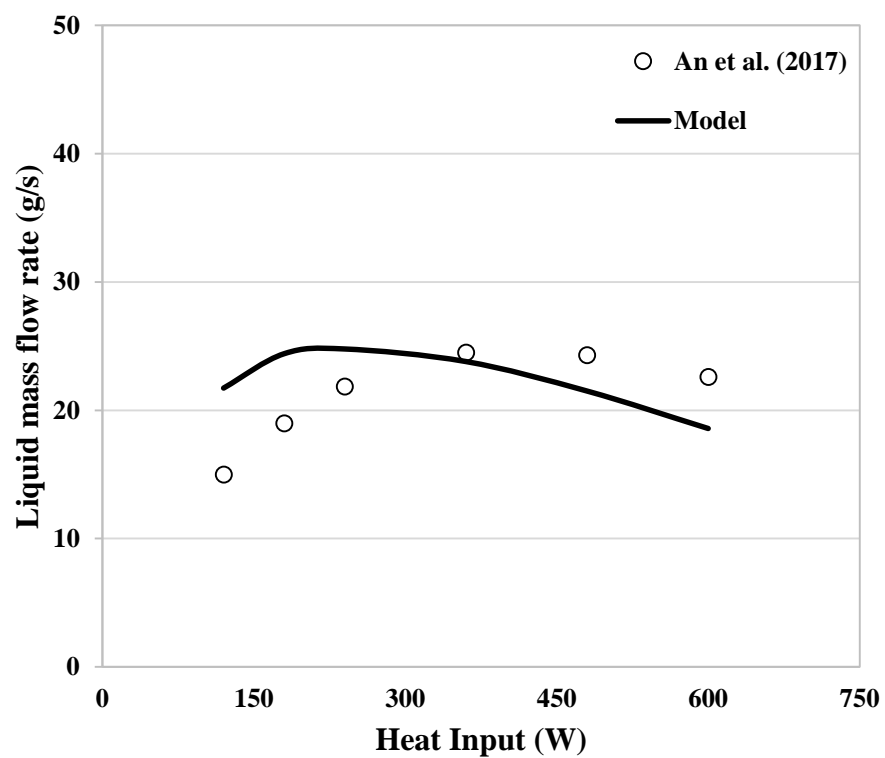


**Figure 51:** Performance comparison for the submergence ratio of 0.4

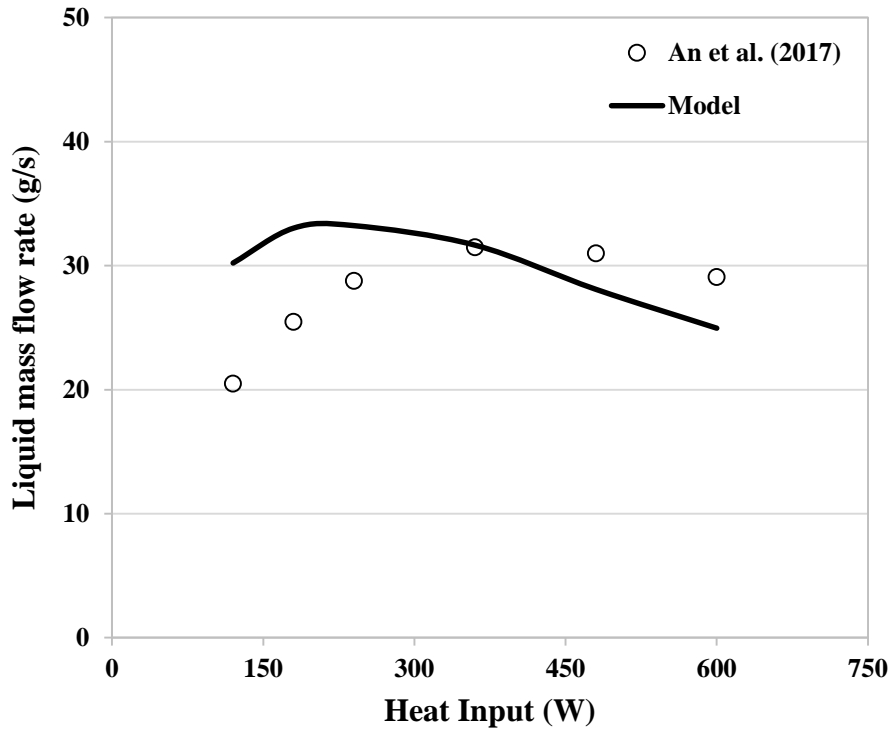


**Figure 52:** Performance comparison for the submergence ratio of 0.5

## 4.11 Concluding remarks

In this chapter, the operation of the bubble pump was examined by using an airlift pump and an analytical model of the bubble pump was developed. The performance of the bubble pump was studied based on the flow regimes and design parameters. From the flow regime visualisation and the experimental performance, it was found that the slug flow regime is the most efficient flow regime during the operation of the bubble pump, while the bubbly flow regime is the least efficient flow regime as it was not able to pump the liquid. The experimental results showed that both the lift-tube diameter and the submergence ratio influence the performance of the bubble pump. For the same submergence ratio, the change in the lift-tube diameter influences the performance of the bubble pump.

A theoretical model was developed based on the correlations developed for each specific flow regime. It was observed that the model showed good predictions for slug flow regime. However, some deviation between the predicted values of the model and the experimental values were observed in the transition region of slug-churn flow regime due to its unstable nature. At this transition, it was found that the amount of the liquid pumped by the bubble pump reached a maximum value after which its performance reduced. As such, a single lift-tube bubble pump is best utilised up to this limit, which also limits the operating range of the DAR system. Therefore, in order to improve the operating range of the DAR system, the pumping performance of the bubble pump needs to be improved.



# **Chapter 5: Influence of multiple lift-tube on the performance of bubble pump**

## **5.1 Overview**

In Chapter 4, an understanding was developed regarding the pumping characteristics of a single lift-tube bubble pump. It was found that a single lift-tube could pump efficiently up to a maximum after which its pumping performance reduces. Therefore, in order to improve the pumping capacity of a single lift-tube bubble pump, the submergence ratio could be increased or the lift-tube diameter increased. However, increasing the lift-tube diameter may increase the inter-phase slip affecting the pumping performance of the bubble pump (Rattner, 2015) and as shown previously, there is clearly a limit to the amount of liquid delivered by a single lift-tube bubble pump.

In order to overcome the limitations associated with a single lift-tube for achieving higher liquid flow rate, there is a possibility of utilising multiple lift-tubes. Vicatos and Bennett (2007) were probably the first researchers to have investigated the performance of a multiple lift-tube bubble pump. In their study, they examined two experimental units: one had a bubble pump accommodating both single and multiple lift-tubes, while the other involved installing additional lift-tubes in the bubble pump of a commercially manufactured DAR system. The results of their experimental multiple lift-tube bubble pumps showed that multiple lift-tubes were able to increase the pumping capacity of the bubble pump. By installing additional lift-tubes in the commercial DAR system, the performance of the system improved at high heat input. While at low heat input, the addition of lift-tubes reduced the performance of the DAR system due to a change in

generator temperature. However, Vicatos and Bennet did not explore the mechanistic behaviour of multiple lift-tube bubble pumps.

Further analysing the influence of multiple lift-tube, Monsef et al. (2012) performed an experimental analysis of a DAR system with five lift-tubes. They used H<sub>2</sub>O-LiBr as the working fluid pair and reported that multiple lift-tube bubble pumps were suitable for use in a DAR system. However, they also did not study the flow behaviour in the lift-tubes.

Gurevich et al. (2015) studied the performance of two and three multiple lift-tube bubble pumps with R134a-DMAC as the working fluid pair. They concluded that the use of the multiple lift-tube improved the cooling capacity of the DAR system, as more refrigerant participated in the cooling cycle. In addition, they examined the influence of additional lift-tube on the pumping characteristics and suggested that the mutual influence between the lift-tubes was negligible as the flow rates were evenly distributed.

Recently, Lin et al. (2016) studied the performance of a cone-mouthed bubble pump with 1,2,3,4, and 5 lift-tubes. Their results showed that the pumping performance of the bubble pump improved with an increase in the number of lift-tubes and submergence ratio. However, unlike Gurevich et al. (2015) they suggest that the use of multiple lift-tubes might result in an uneven distribution of gas in the lift-tubes, which needs further attention.

From the studies performed on multiple lift-tube bubble pumps, it seems that the research on bubble pumps with multiple lift-tubes is still in the preliminary phase. In

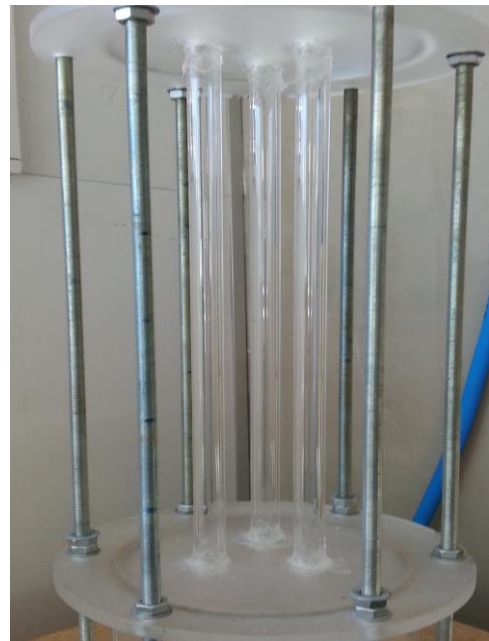
particular, it requires a better understanding of the pumping characteristics of multiple lift-tubes and the influence of lift-tubes on each other.

## 5.2 Experimental method

The experimental setup for this investigation was the same as that used for the single lift-tube bubble pump described in Section 4.2 but with 2 and 3 lift-tubes having a diameter and length of 10 mm and 500 mm, respectively, as shown in Figure 53. Tests were conducted under submergence ratios of 0.7, 0.5, and 0.3. For all tests, the airflow rate was varied over the range of 0.05 to 50 litre/min.



(a)



(b)

**Figure 53:** Bubble pump with multiple lift-tube (a) 2 lift-tubes (b) 3 lift-tubes

The lift-tubes were placed symmetrically with respect to the sparger as shown in Figure 54. This meant that the direct path length for bubbles was equal. As per the single lift-tube experiments, the airflow rate was adjusted and the rate of the water pumped was

measured. Furthermore, the occurrence of the flow regime in each lift-tube was visualised.

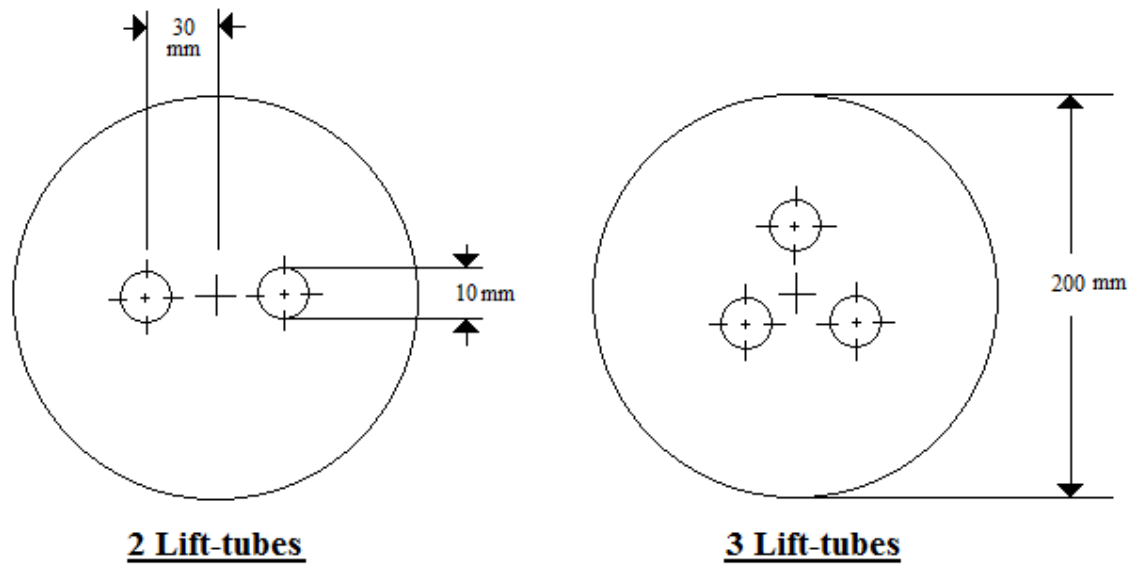


**Figure 54:** Symmetry of the multiple lift-tube in the experimental configuration

## 5.3 Experimental results

### 5.3.1 Observation of flow regimes in multiple lift-tubes

During the visual observation of the flow regimes in the single-lift tube bubble pump, as described in section 4.3.1, it was seen that the flow inside the lift-tube was a complex two-phase flow consisting of different flow regimes. This suggests that the distribution of the two-phase flow in multiple lift-tube will add to its complexity. As such, it is important to analyse the regime of the two-phase in each lift-tube and its influence on the pumping characteristic of the bubble pump.

At low airflow rates, a variable pumping phenomenon was observed. Initially, one of the lift-tubes stops pumping and effectively becomes idle for a short span of time. Later

on, the idle lift-tube starts pumping and one of the other lift-tube becomes idle. This idle behaviour of the lift-tubes resulted in varying flow in the lift-tubes. Figures 55 and 56, shows the variable pumping observed for both 2 and 3 tube configuration.

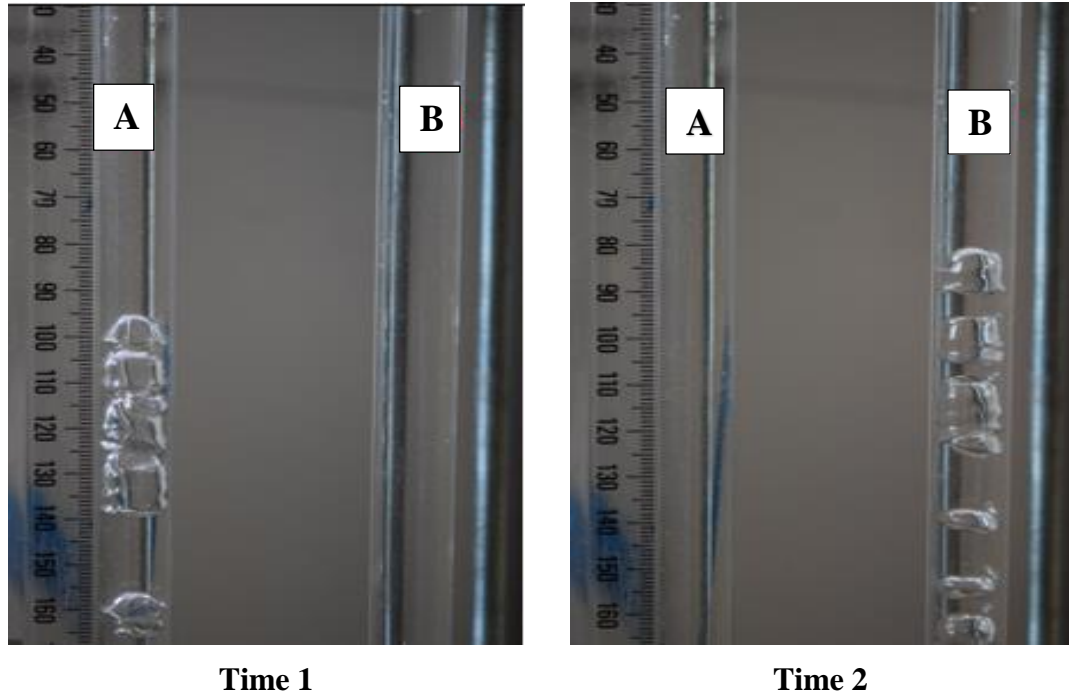


**Figure 55:** Variable pumping phenomenon in 2 lift-tubes

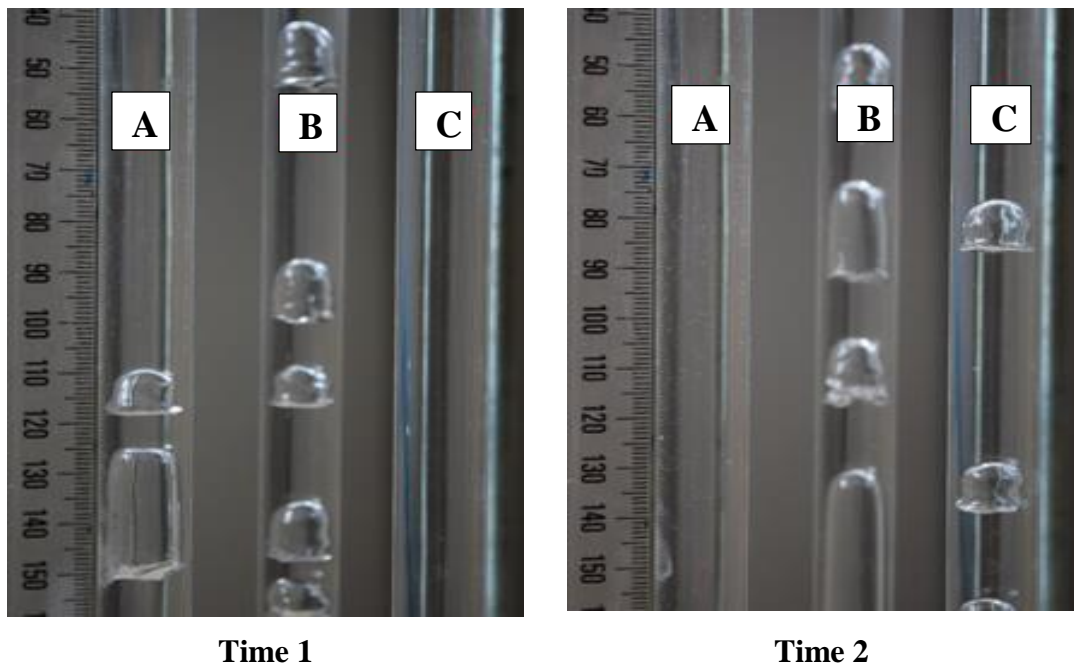


**Figure 56:** Variable pumping phenomenon in 3 lift-tubes

On increasing the airflow rate, the variable pumping phenomenon diminished and the flow was stabilized. A constant pumping phenomenon was observed in all lift-tubes; however, the rate of the pumping was not the same for all the lift-tubes highlighting an uneven distribution of air in each lift-tube.

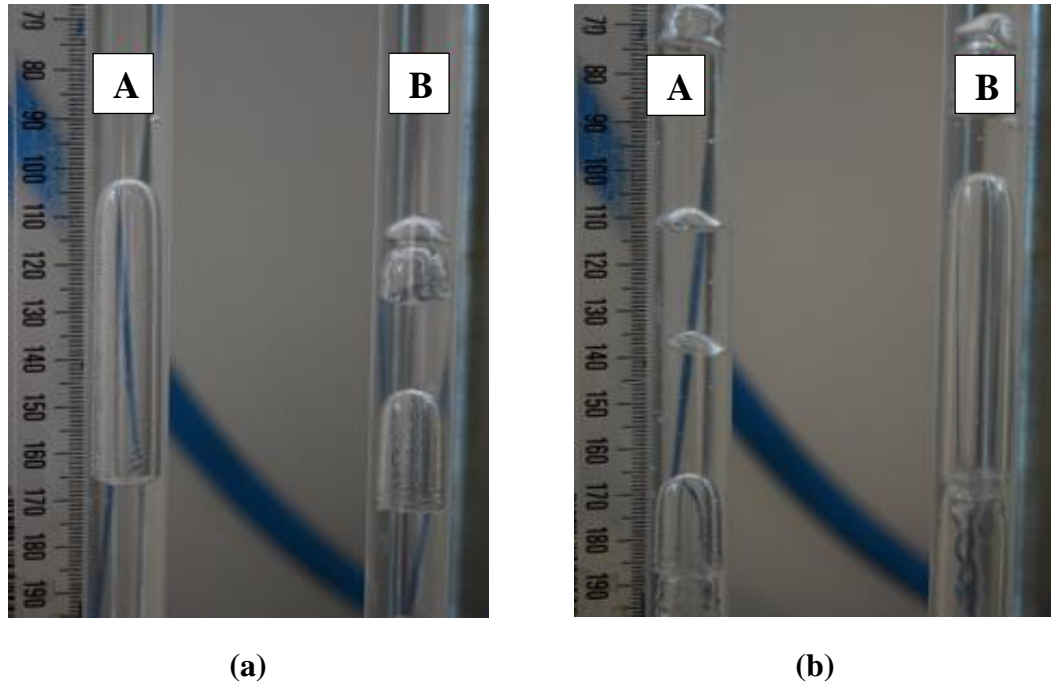
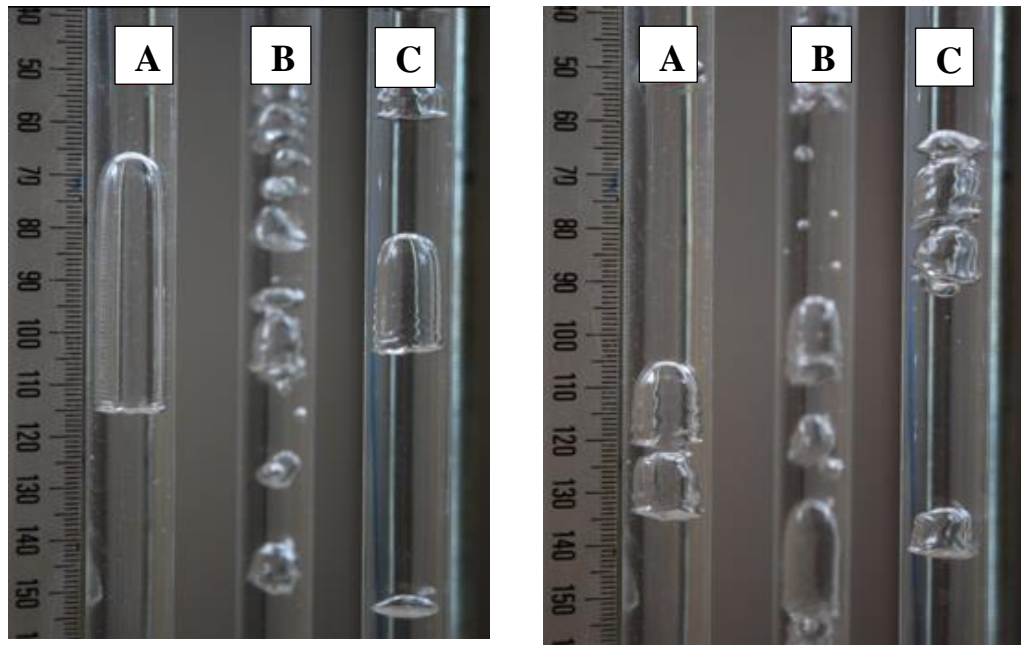


**Figure 57:** Slug flow regime in 2 lift-tube configuration at different time intervals

At a fixed airflow rate, Figure 57 shows the occurrence of slug flow regime in a two lift-tube configuration at a different time interval. Even though the slug flow regime was observed in both the lift-tubes, the size of the air slugs suggests an uneven distribution of air between the lift-tubes. As in the case of Figure 57(a), the size of the air slug in lift-tube A is larger than in lift-tube B; however, after some time more air starts to flow in lift-tube B and results in large air slugs as shown in Figure 57(b).



(a)

(b)

**Figure 58:** Slug flow regime in 3 lift-tube configuration at different time intervals

Similarly, one would expect the same behaviour for a 3 lift-tube configuration. In this regard, Figure 58 shows the occurrence of different sizes of air slugs in each lift-tube. As shown in Figure 58(a), the size of the air slug in lift-tube A is bigger than compared to other lift-tubes which, after some time interval, shortens due to low airflow rate as shown in Figure 58(b), thus, representing an uneven flow distribution.

Further increasing the airflow rate the flow regime occurring in each lift-tube becomes unstable which suggest the occurrence of churn flow regime as shown in Figure 59. Visual observations during the experiments showed unequal pumping phenomena from each lift-tube, which suggest an unequal distribution of air in the lift-tubes.

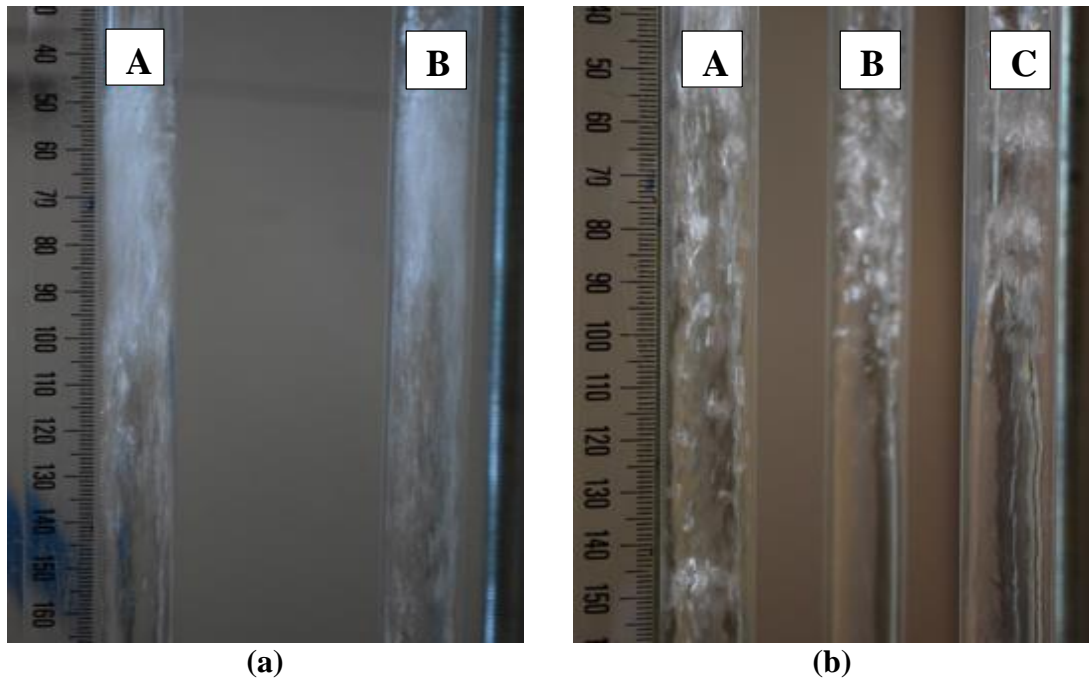


**Figure 59:** Churn flow regime in (a) 2 lift-tubes (b) 3 lift-tubes

### 5.3.2 Influence of the additional lift-tube

The influence of additional lift-tubes on the pumping performance at different submergence ratios is shown in Figures 60 to 62.

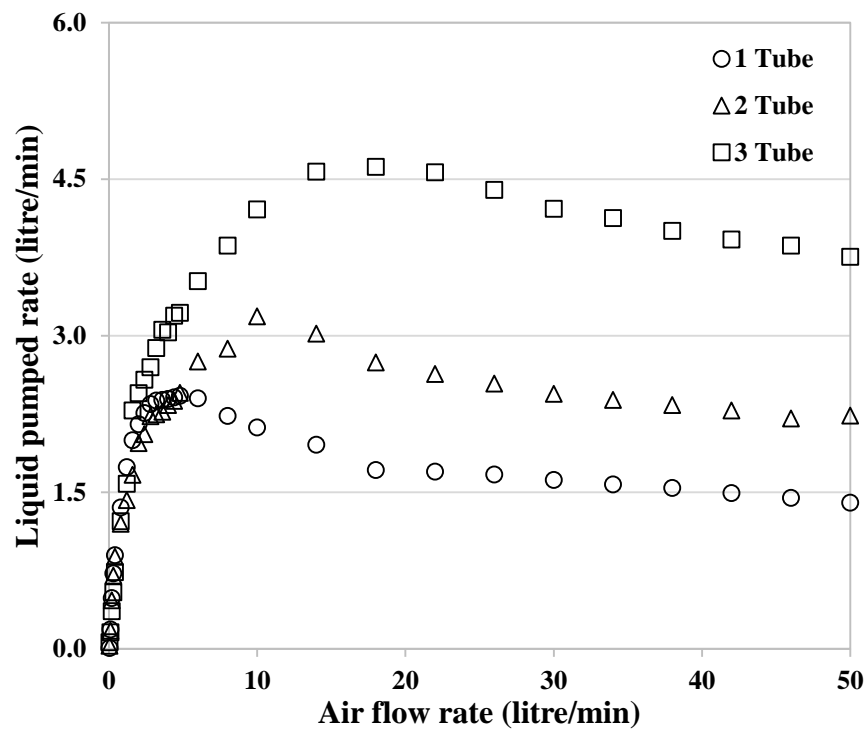


**Figure 60:** Influence of lift-tube quantity at submergence ratio of 0.7



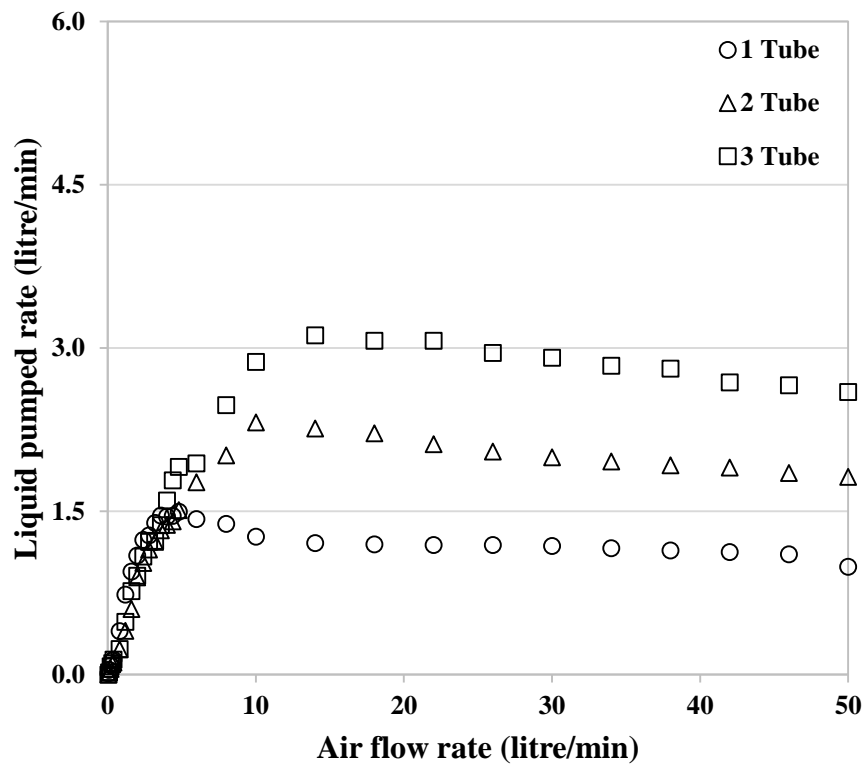


**Figure 61:** Influence of lift-tube quantity at submergence ratio of 0.5

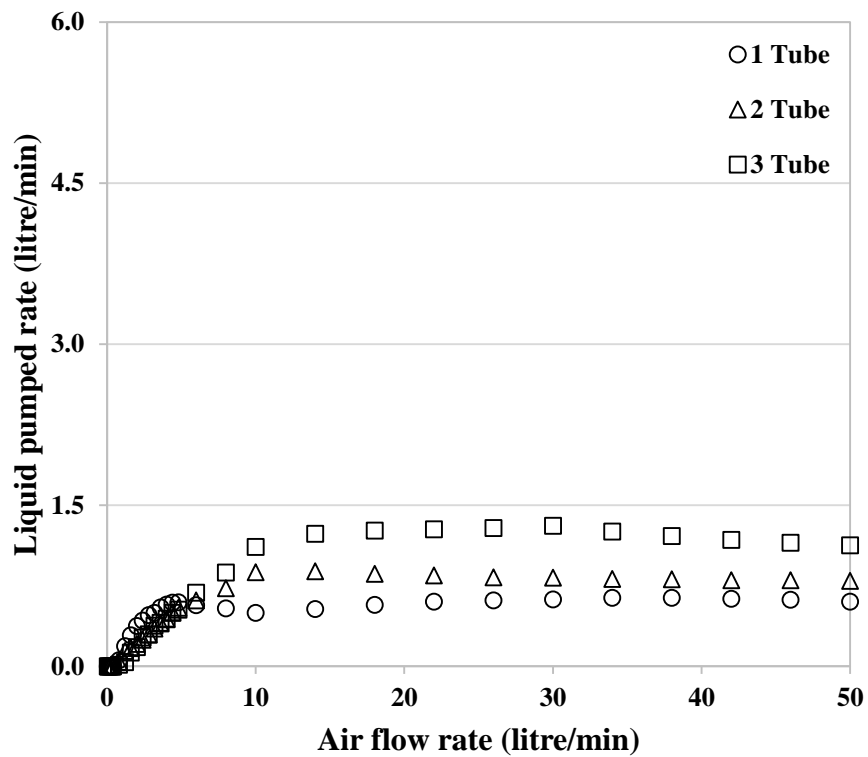


**Figure 62:** Influence of lift-tube quantity at submergence ratio of 0.3

An increase in the number of lift-tubes increases the maximum pumping capability at all submergence ratios. It is seen that irrespective of the lift-tube quantity, the performance characteristics of the bubble pumps are the same. In each case, the performance curve followed a trend of a sharp slope at lower airflow rates followed by a gentle decay, as the airflow rate was increased.

Furthermore, it was seen that the impact of the multiple lift-tube takes effect when the performance of single lift-tube starts to decrease. For all the test cases, the performance of the single lift-tube bubble pump was found to be slightly better than multiple lift-tube bubble pump at low airflow rates. However, the range of low airflow rate varies with the submergence ratio.

## **5.4 Multiple lift-tube bubble pump modelling**

Having analysed the experimental performance of a multiple lift-tube bubble pump using an airlift pump, a theoretical study was performed in order to predict its performance. In previous studies, Vicatos and Bennett (2007) and Lin et al. (2016) theoretically analysed the performance of multiple lift-tube bubble pumps assuming uniform flow distribution. However, as they did not take into account the mal distribution of gas that was evident in the experimental investigation of this study, there is a need to examine the validity of this approach.

To address this shortcoming, it was decided to incorporate a hypothetical distribution of gas in each lift-tube of a multiple lift-tube configuration assuming each lift-tube to be modelled as a single lift-tube as shown in Section 4.5. For this purpose, the amount of

air in each lift-tube in a multiple lift-tube configuration was varied between 10 to 90 percent of the total amount of airflow rate as shown in Table 8.

**Table 8:** Percentage of airflow rate in each lift-tube

<b>Test Condition</b>	<b>Number of Tubes</b>	<b>Percentage of airflow rate</b>		
		<b>Tube 1</b>	<b>Tube 2</b>	<b>Tube 3</b>
1	2	10	90	-
2	2	20	80	-
3	2	30	70	-
4	2	40	60	-
5	2	50	50	-
6	3	10	20	70
7	3	20	30	50
8	3	40	50	10
9	3	60	20	20

For the test condition 1, it was assumed that in a 2 lift-tube bubble pump, 10 percent of the total airflow rate flows through one tube and 90 percent of the total airflow rate flows through another tube. Similarly, different assumptions in the percentage of airflow rate in each lift-tube were made for the other test conditions.

Now, in order to estimate the pumping performance of each lift-tube in a multiple lift-tube bubble pump configuration, the model of a single lift-tube bubble pump developed in Section 4.5 was used. The individual performance of each lift-tube was summed to estimate the total performance of the multiple lift-tube configuration. Figure 63 shows the comparison between the experimental performance and the model of a two lift-tube bubble pump operating at a submergence ratio of 0.5.

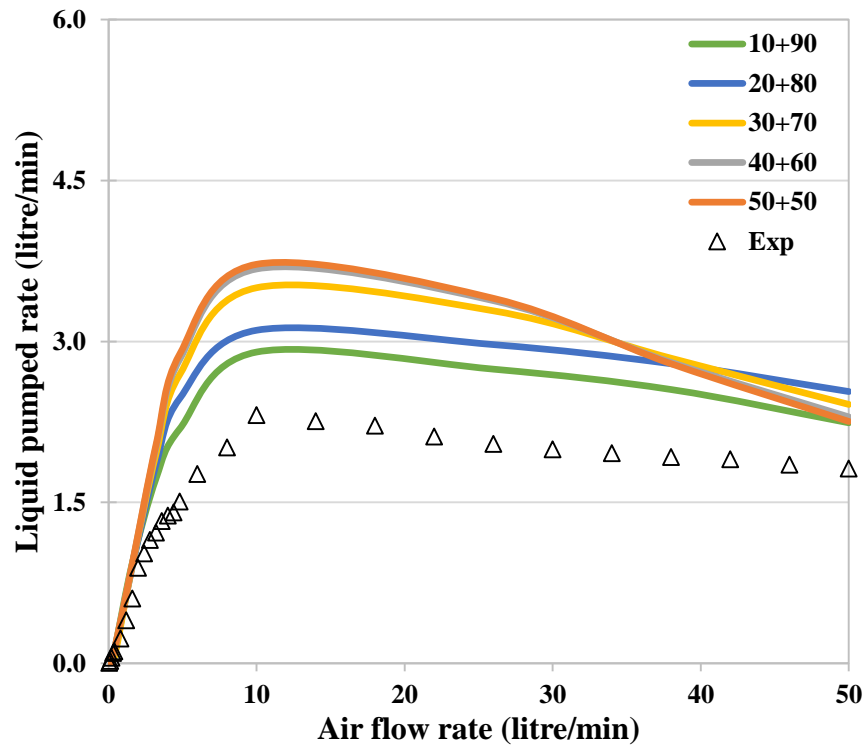


**Figure 63:** Comparison between experiment and model for 2 lift-tube bubble pump

It was found that at very low values of airflow rate, the model predicts well for all the conditions of distributed flow, which is probably due to the occurrence of the stable slug flow regime. However, at high airflow rates, the model starts to deviate significantly from the experimental results due to the occurrence of the churn and later on annular flow regime. More tellingly, even for uniform distribution (50 + 50) of the flow, there is relatively poor agreement.

Similarly, Figure 64 shows the comparison between the experimental performance and the model of a three lift-tube bubble pump operating at a submergence ratio of 0.5. Similar to the case of 2 lift-tube configuration, both the model predictions and the experimental results follow the same trend. This suggest that by considering the different conditions of distributed airflow rates, the theoretical model is limited to very low values of airflow rate.

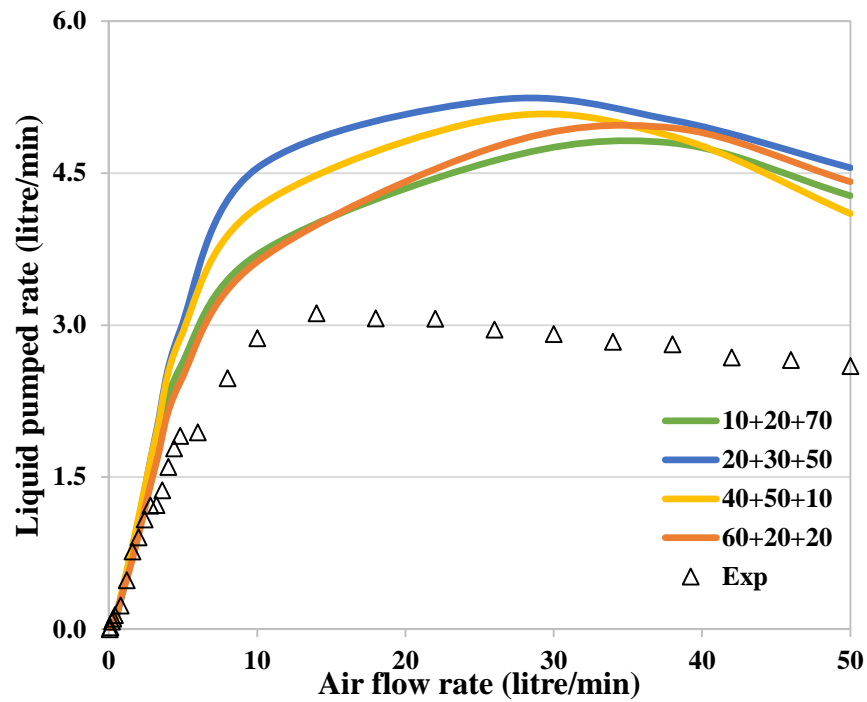


**Figure 64:** Comparison between experiment and model for 3 lift-tube bubble pump

## 5.5 Concluding remarks

In this chapter, the pumping characteristics of bubble pumps with multiple lift-tubes were studied. The results of the experiments showed that multiple lift-tubes improve the pumping capacity of the bubble pump. In addition, visual observations during the experiments revealed that both the nature of flow regimes and the pumping rate varies between the lift-tubes, which suggested unequal airflow distribution in the lift-tubes.

In exploring this, a numerical investigation using empirical relationships was performed in order to predict the pumping performance of multiple lift-tube bubble pumps. The unequal distribution of air was considered in the theoretical model. It was found that for the large range of airflow rates, the theoretical prediction varied significantly with the experimental results. As such, it raises a question as to how to effectively model a multiple lift-tube bubble pump to account for the flow distribution.

# **Chapter 6: Artificial neural network based modelling of a multiple lift-tube bubble pump**

## **6.1 Overview**

To overcome the limited pumping capacity of single lift-tube bubble pump, it was hypothesised that multiple lift-tubes could be used as studied in Chapter 5. However, it was shown that a classical approach was unable to model this effectively. From an analytical perspective this leads to multiple steady state solutions due to flow distribution, and hence, accurately predicting the pumping characteristics becomes extremely complex (Pustylnik et al. 2006, Baikin et al. 2011).

In light of the complexity of multiphase flow, few studies have utilised artificial intelligence techniques to better predict their behaviour. In this respect, researchers have looked at identifying two-phase flow regimes from temporal pressure measurements using artificial neural networks (ANN) (Azizi et al. 2016a, Al-Naser et al. 2016, Bar and Das (2013), Bar et al. 2013, Salgado et al. 2010). The advantage of an ANN model is that it does not require explicit knowledge of the physical phenomena under investigation (Azizi et al. 2016b), but can be developed through training to predict outputs based on a series of specified inputs. Hence, an ANN can be used to predict the unknown output values from a set of new input values previously unseen by the model (Bar et al. 2010).

That said, there has been no study on predicting the performance of multiple lift-tube bubble pump using ANN. As such, the aim of this study is to predict the performance of a multiple parallel lift-tube airlift pump using the MATLAB tool based ANN technique.

## 6.2 Method

For this study, the ANN consists of three interconnected layers – an input, hidden, and output layer as shown in Figure 65, with each layer consisting of one or multiple nodes called neurons.

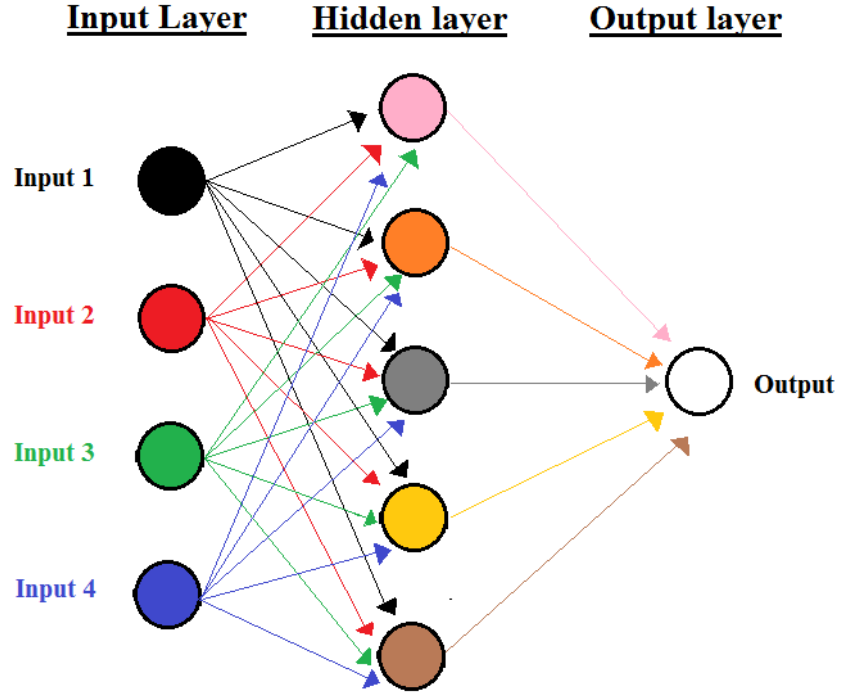


**Figure 65:** Schematic diagram of a typical artificial neural network

The number of nodes in the input and the output layer is equal to the total number of input and output parameters respectively, whereas the number of the nodes in the hidden layer depends upon the performance and the complexity of the network (Azizi et al. 2016b). The input layer accepts the data from the specified source and transfers it to the nodes in the hidden or output layers, which act as a summing junction for inputs, and modifies the input, using Equation 67.

$$S_i = \sum_{j=1}^m x_i w_{ij} + b_j \quad (67)$$

In Equation 67,  $S_i$  is the net input to node  $j$  in the hidden or output layer,  $x_i$  is the input to node  $j$ ,  $w_{ij}$  is the strength of the weight connection between the  $i^{th}$  node and  $j^{th}$  node,  $b_j$  is the bias associated with node  $j$ , and  $i$  is the number of nodes. In order to generate relationships between the input and output a linear (purelin), hyperbolic tangent sigmoid (tansig), logarithmic sigmoid (logsig) or radial basis (radbas) transfer function can be used. The most common transfer functions for a non-linear relationship are the logsig and tansig functions, which are given by Equations 68 and 69 respectively.

$$f(S_j) = \frac{1}{1 + e^{-S_j}} \quad (68)$$

$$f(S_j) = \frac{e^{S_j} - e^{-S_j}}{e^{S_j} + e^{-S_j}} \quad (69)$$

With an ANN, the relationship between the data in the input and output layers is established using a ‘training’ process consisting of three steps, training, testing, and validation. For the training, a set of known input and output values are given to the network, the model adjusts the weight between the nodes until the desired output is obtained (Malayeri et al. 2003). This iterative method of adjusting the weights is termed as epoch. Subsequently, the ANN undergoes testing and validation to determine if unseen input data can be presented to the network to determine output.

In order to train the ANN, it was necessary to develop a data set with a number of input variables. For this study, four input parameters were chosen: airflow rate, lift-tube diameter, lift-tube quantity, and submergence ratio, with the output parameter being the amount of liquid pumped. To develop a sufficiently rich data set for the ANN model, a total of 1044 data points (Appendix D) were collected from experiments performed on



1, 2 and 3 lift-tubes airlift pump with configurations shown in Table 9 and with airflow rates between 0.5 and 50 litre/min at each configuration.

**Table 9:** Experimental configurations used for the design of the network

Setup	No of tube(s)	Diameter of tube (mm)	Submergence Ratio
1	1	14	0.7
2	1	14	0.5
3	1	14	0.3
4	1	10	0.7
5	1	10	0.5
6	1	10	0.3
7	2	10	0.7
8	2	10	0.5
9	2	10	0.3
10	3	10	0.7
11	3	10	0.5
12	3	10	0.3

As described earlier, the network was trained with four input parameters to determine the rate at which water was pumped. In doing this, the input data was randomly divided into three sets consisting of 70% for training using the Levenberg-Marquardt back propagation (LM-BP) algorithm (Singh et al. 2007), 15% for validation, and 15% for testing. The training set was used to develop and adjust the weights and the bias of the network, the validation set was used to ensure the accuracy of the developed model, and the testing set was used to check the final performance of the developed network.

In the initial phase of the ANN modelling, the number of the neurons in the hidden layer is normally not known. As such, they are estimated by varying their number and

calculating the error for each set of neurons. In this study, the number of the neurons in the hidden layer was varied from 2 to 30 and the error for each case was estimated using the mean square error (MSE) as given by Equation 70.

$$MSE = \frac{1}{n} \sum_{m=1}^n (Y_{Exp,m} - Y_{Pred,m})^2 \quad (70)$$

Where  $n$  is the number of data points,  $Y_{Exp}$  is the experimental value, and  $Y_{Pred}$  is the predicted value from the network and the estimation of the neurons in the hidden layer was estimated using two transfer functions: tansig and logsig.

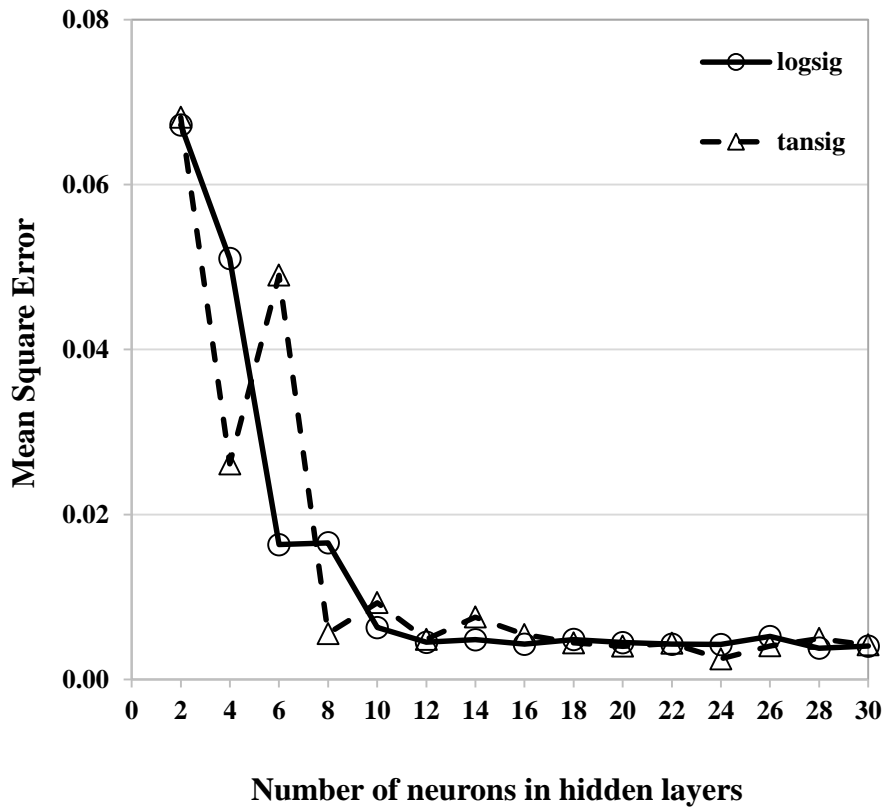


**Figure 66:** Determination of the number of neurons in the hidden layer

As shown in Figure 66, the network with 24 hidden neurons and using tansig transfer function showed the least error. Therefore, the developed model used tansig as the transfer function and consisted of 4 neurons in its input layer, 24 neurons in its hidden

layer and 1 neuron in its output layer. The convergence of the optimum model is shown in Figure 67.

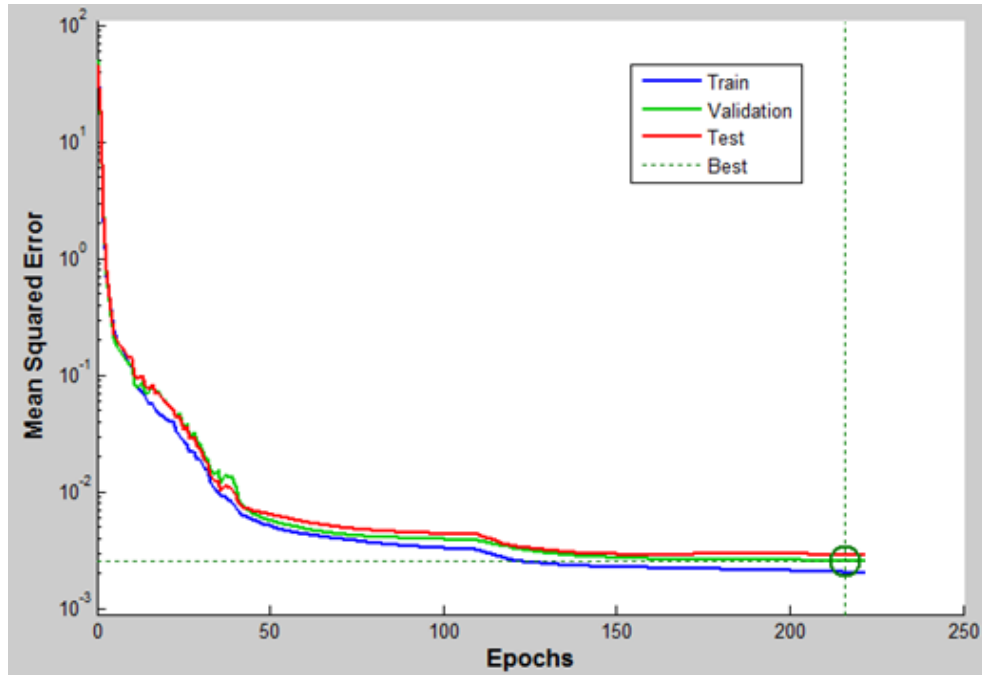


**Figure 67:** MSE versus epoch with 4-24-1 network configuration

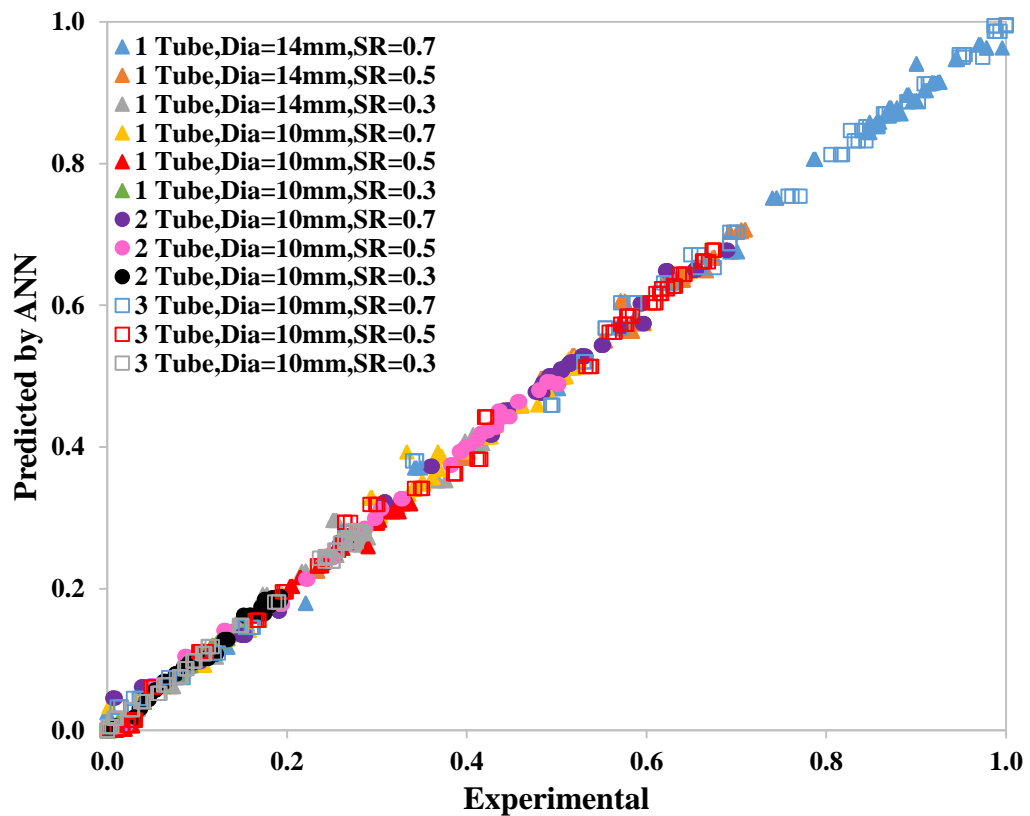
### 6.3 Results and discussions

In formulating an ANN, it is important to understand the consistency of its predictions when applied to the data used in the development phase of the model and for the prediction of the unseen data. In this respect, the performance of the optimum model was assessed by calculating the coefficient of determination ( $R^2$ ) and mean squared error (MSE) in each phase. The performance of the model is shown in Table 10 and shows a high value of  $R^2$  and MSE for all the data sets, thus indicating a strong predictive capacity.

**Table 10:** Performance of ANN model for training, validation, testing and all data sets

Data	No of Data points	MSE	R <sup>2</sup>
Training	730	0.00215160	0.99933
Test	157	0.00289613	0.99903
Validation	157	0.00257442	0.99925
Total Data	1044	0.00250516	0.99999

Exploring this further, Figure 68 shows a normalised comparison between the optimum ANN predicted values and the experimental values. From this it can be seen that the optimum model shows good prediction values when compared with the values for different experimental set ups.

**Figure 68:** Predicted values from ANN model versus experimental values for all the data sets

In order to check the flexibility of the ANN model it was tested for its ability to predict the pumped water flow rate based on an unseen data set within the training bounds. In the first instance, the ANN was set the task of predicting the liquid pumped by an airlift pump with 2 and 3 lift-tubes of 10 mm diameter, submergence ratios of 0.5 and 0.7, and airflow rates that had not been previously tested.

Figures 69 and 70 show the comparison between the prediction made by the ANN and the experimental data for 2 and 3 lift-tubes. Given that the testing was for data within the training bounds, the results show good agreement between the experiment and the ANN prediction, as one would expect.

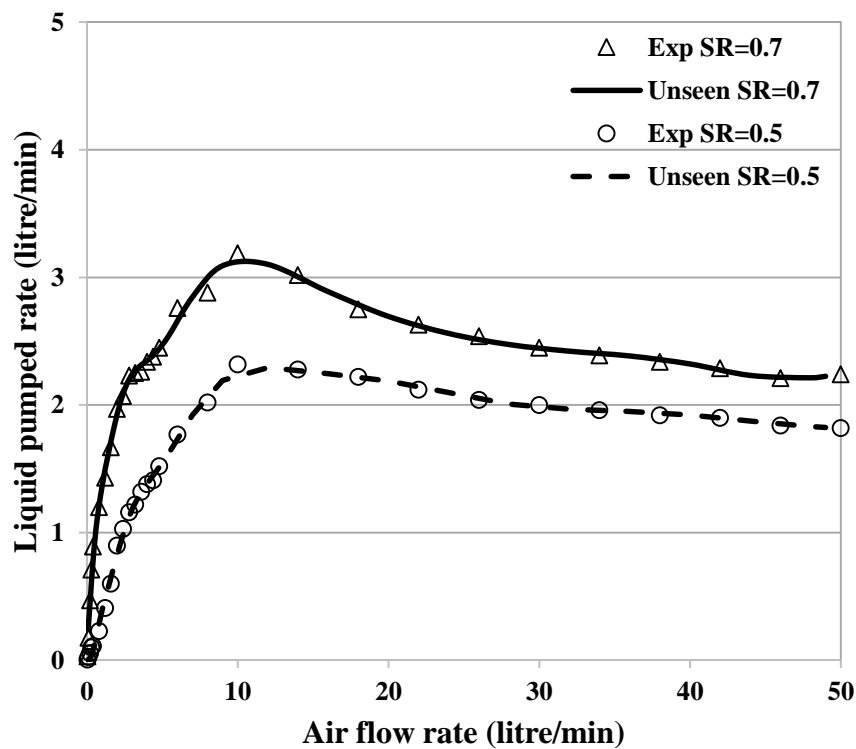


**Figure 69:** Predicted values of unseen data from ANN model versus experimental values for 2 lift-tubes

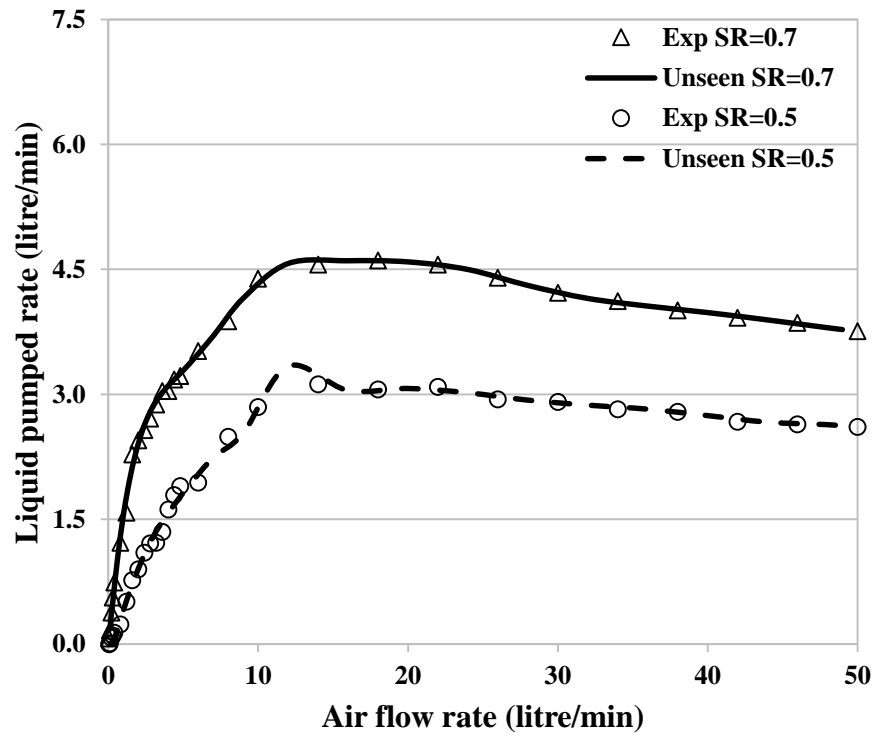


**Figure 70:** Predicted values of unseen data from ANN model versus experimental values for 3 lift-tubes

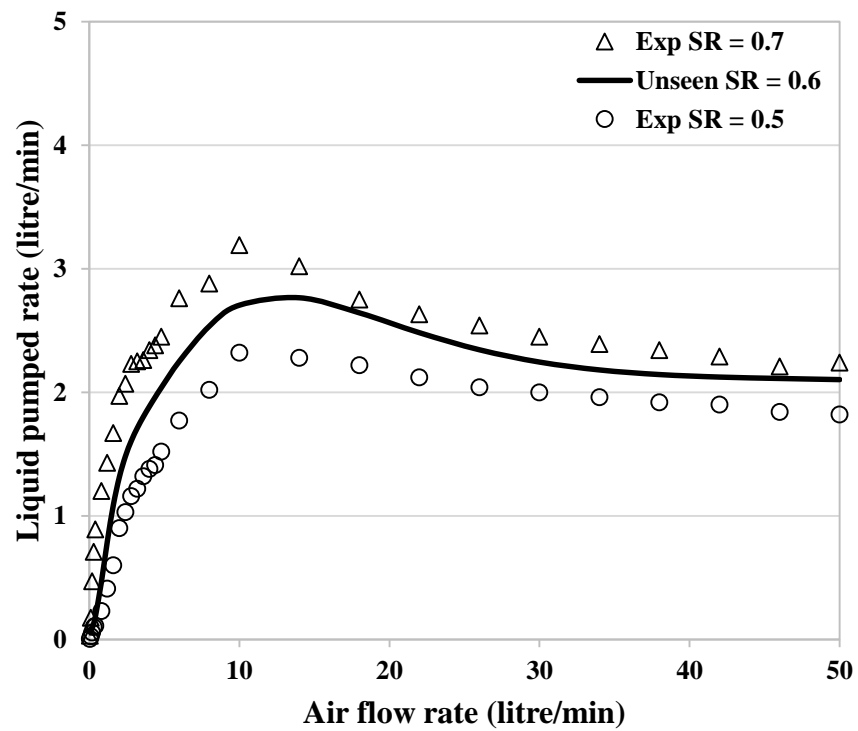


**Figure 71:** Predicted values for 0.6 submergence ratio from ANN model versus experimental values for 2 lift-tubes

Following on from this, the performance of the multiple lift-tube airlift pump for an unseen submergence ratio (0.6) was evaluated using the ANN. As shown in Figures 71 and 72, the model suggests that the pumping capacity would lie between that of pumps of submergence ratios of 0.5 and 0.7, as one might expect.

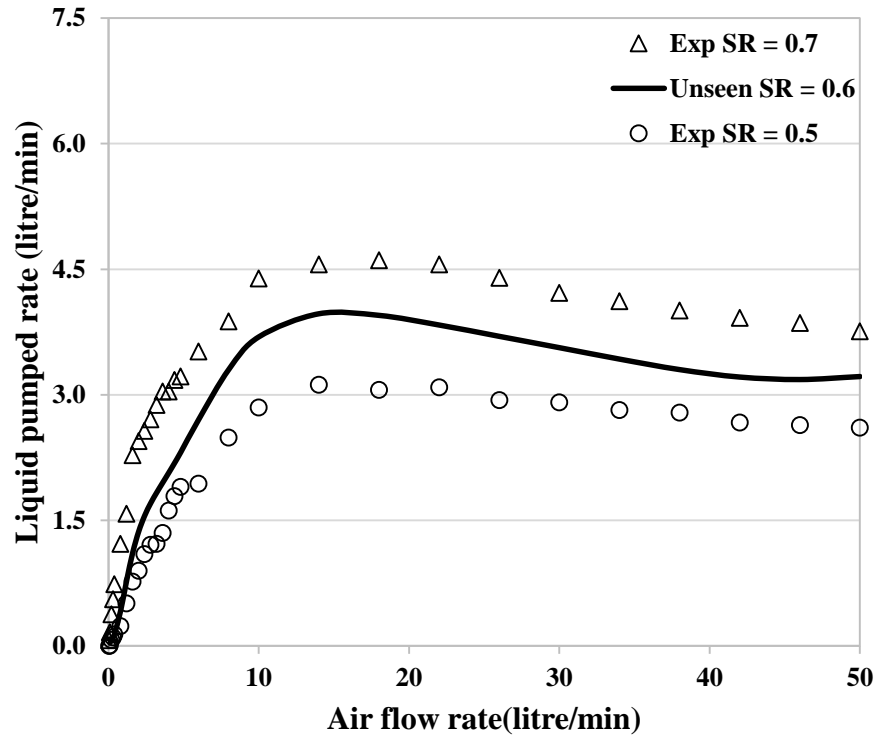


**Figure 72:** Predicted values for 0.6 submergence ratio from ANN model versus experimental values for 3 lift-tubes

Previously, it was shown that an ANN provided an accurate prediction of the pumped liquid flow rate within the bounds of the data it was trained. However, if the ANN is provided with inputs outside the bounds of the training set, one would expect a less accurate prediction. That said, with a robust network it should be able to provide insights into possible outcomes that would be extremely difficult to realise by traditional methods. Hence, to examine the ANN capabilities outside the training bounds the ANN was used to predict the performance of an airlift pump with four lift-tubes at the submergence ratio of 0.7. In the previous results, it could be seen that an

increase in the number of lift-tubes reduces the performance of the pump at low airflow rates but improves it at higher airflow rates. Essentially the airflow needs to be divided amongst multiple lift-tubes, which delays the onset of slug flow, where the pump tends to perform best.

Based on this, one would expect to see a four-tube airlift pump to exhibit lower pumping rates at low airflow rates and higher rates at higher airflows. As such, Figure 73 shows the predictions of the ANN for the multiple airlift pump operating with four lift-tubes compared to that of three lift-tubes and illustrates the behaviour one would expect. In this respect, the ANN provides an insight into the characteristics of the airlift pump when operating with four lift-tubes, which, as stated previously, would be extremely difficult to achieve by analytical means.

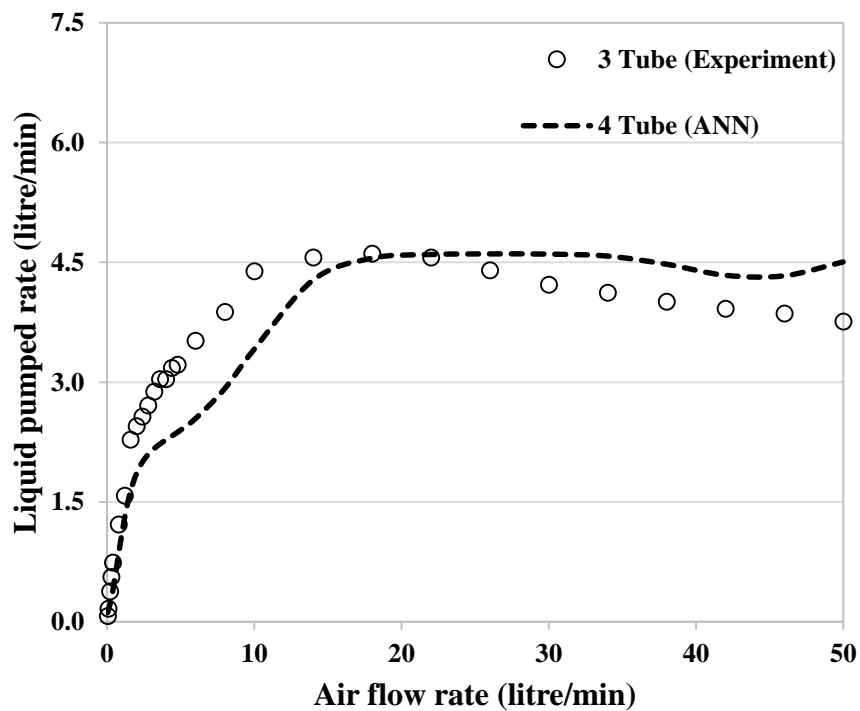


**Figure 73:** Predicted values for 4 lift-tube airlift pump from ANN model



## 6.4 Predicting the performance of heat driven bubble pump

After successfully predicting the performance of the multiple lift-tube bubble pump using the model developed through ANN technique, the model was tested for its applicability to a heat driven multiple lift-tube bubble pump.

For this purpose, the predictions of the ANN model were compared with the experimental results of Lin et al. (2016). In this regard, Figures 74 and 75 show the predictions of the ANN model for a heat-driven bubble pump with two and three lift-tubes (Appendix C).

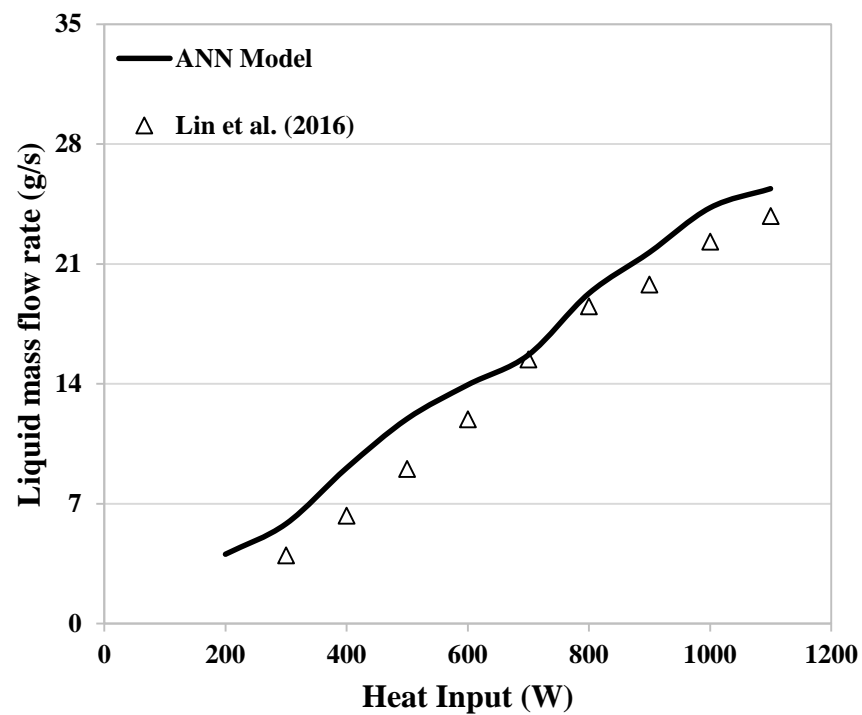


**Figure 74:** Comparison between the experimental results of Lin et al. (2016) and ANN predictions for 2 lift-tubes

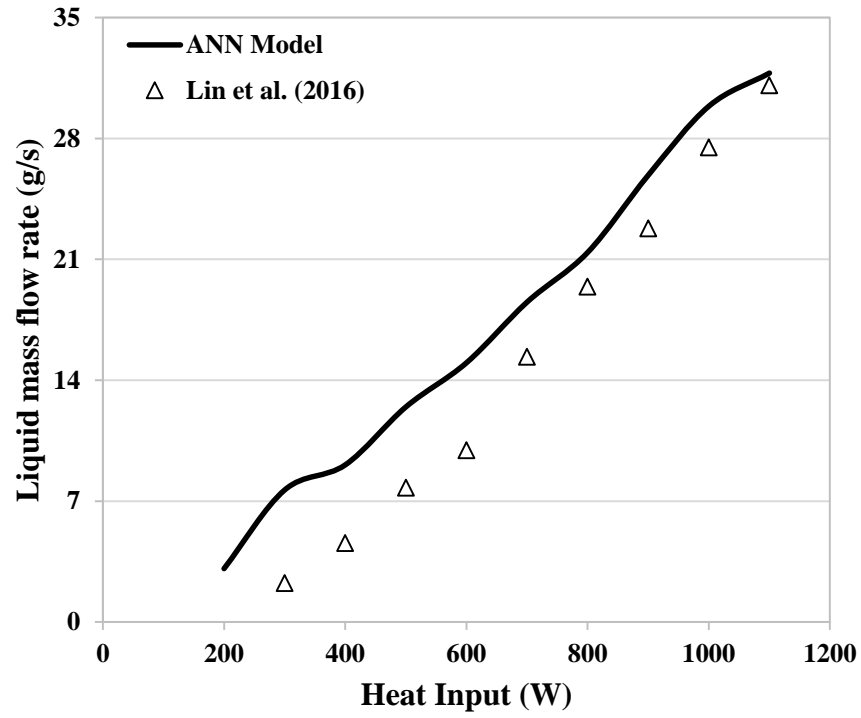


**Figure 75:** Comparison between the experimental results of Lin et al. (2016) and ANN predictions for 3 lift-tubes

The model developed using the ANN technique, shows good agreement with experimental results of Lin et al. (2016). It can be seen that both the model predictions and the experimental results follows the same trend i.e. the performance of the multiple lift-tube improves with the increase of the heat input. This illustrates that the ANN model developed using the experimental values of the airlift pump can successfully be used to predict the performance of heat driven multiple lift-tube bubble pumps.

## 6.5 Concluding remarks

In this study, a novel ANN technique was developed to predict the pumping characteristics of multiple lift-tube airlift pumps. The ANN was trained, tested and validated against the experimental data that were taken from the studies performed with single and multiple lift-tubes and an optimum ANN was identified. The results showed

that the ANN was able to predict the performance of airlift pumps based on unseen values of airflow rate, lift-tube diameter, number of lift-tubes, and submergence ratios extremely accurately. Moreover, it was shown that the ANN could provide insights into the performance of airlift pumps with design parameters outside the training bounds.

In addition, the ANN model developed using the experimental values of an airlift pump, was able to predict the performance of a heat-driven bubble pump. Given the capability and flexibility of the ANN technique, it presents a unique and novel alternative approach to designing and analysing the performance of multiple parallel airlift pumps. This is of particular significance, as analytical approaches are at best cumbersome and, at worst, unable to facilitate this prediction.

# **Chapter 7: Influence of lift-tube quantity on the performance of a DAR tri-generation system**

## **7.1 Overview**

In the preceding chapters, the experimental investigation of a tri-generation system, sensitivity analysis of a DAR system, modelling and experimental analysis of the bubble pump with single and multiple lift-tube, and the application of ANN technique for predicting the performance of the multiple lift-tube bubble pump were examined. It was suggested that an increase in the quantity of the lift-tube could potentially improve the operating range as well as the refrigerating capacity of the DAR system and eventually the performance of the tri-generation system. Since there is no analytical study in the available literature regarding the influence of the lift-tube quantity on the performance of the DAR system, this chapter explores the influence of the lift-tube quantity on the performance of the DAR system and its impact on small-scale tri-generation system.

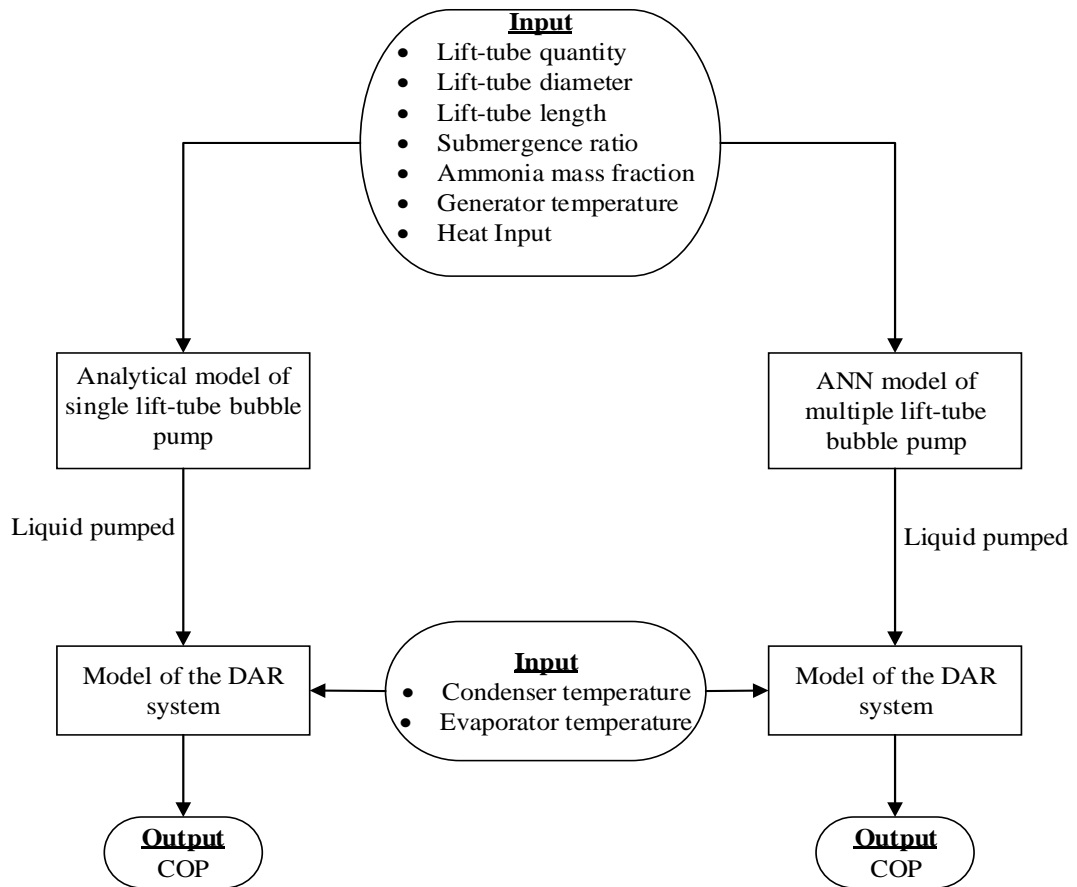
## **7.2 Modelling scheme**

For modelling the performance of a DAR system using a single or multiple lift-tube bubble pump, it was necessary to select the working fluid and the operating parameters. The working fluid used was the binary mixture of ammonia as refrigerant, water as absorbent and hydrogen as an inert gas, while the set of operating parameters selected for the analysis are given in Table 11.

**Table 11:** Input parameters for the analysis

Parameter	Value
Lift-tube quantity	1, 2 and 3
Lift-tube diameter (mm)	10
Lift-tube length (mm)	500
Submergence ratio	0.3
Generator temperature (°C)	150
Condenser temperature (°C)	40
Evaporator exit temperature (°C)	10
Ammonia mass fraction of strong solution	0.3
Heat Input (W)	200-2500

After selecting both the design and operating parameters for the analysis, a modelling scheme was followed as shown in Figure 76.

**Figure 76:** Modelling scheme

The modelling started by first estimating the pumping performance for both single and multiple lift-tube bubble pump. The pumping performance of the single-lift tube bubble pump was estimated using the analytical model of the bubble pump developed in Chapter 4, whereas the pumping performance of the multiple lift-tube bubble pump was estimated using the ANN model developed in Chapter 6. After determining the pumping performance of both the single and multiple lift-tube bubble pump, the performance of the DAR system with single and multiple lift-tube was evaluated. For this purpose, the amount of the liquid pumped was used as an input parameter in the DAR model developed in Chapter 3.

### 7.3 Result and discussion

Figure 77 shows the influence of the lift-tube quantity on the pumping performance of the bubble pump.

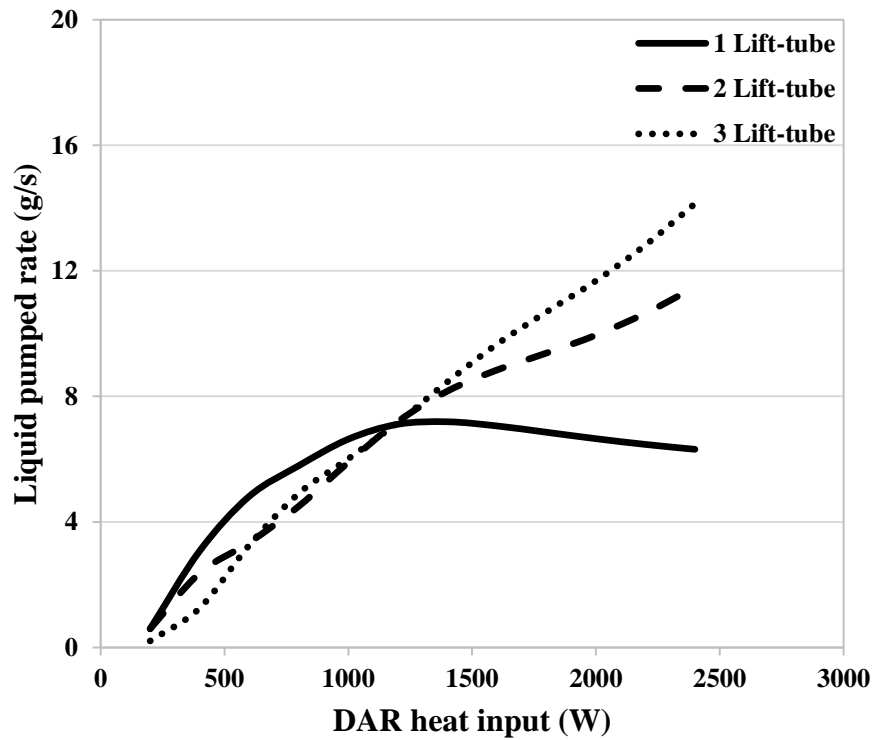


**Figure 77:** Influence of lift-tube quantity on pumping performance

It can be seen that at low heat input the pumping performance of the single lift-tube bubble pump is better than the multiple lift-tube bubble pump. However, as the heat input is increased the pumping performance of the single lift-tube decreases relative to the multiple lift-tube bubble pumps, which is due to the occurrence of different flow regimes in single and multiple lift-tube bubble pump.

Having determined the values for the pumping performance of single and multiple lift-tube bubble pumps. These values were used as one of the input parameter in the DAR model developed in Chapter 3. It was found that the variations in the pumping performance influence the temperature of the working fluid in the generators of single and multiple lift-tube bubble pump as shown in Figure 78. This finding agrees well with the results reported by Vicatos and Bennett (2007).

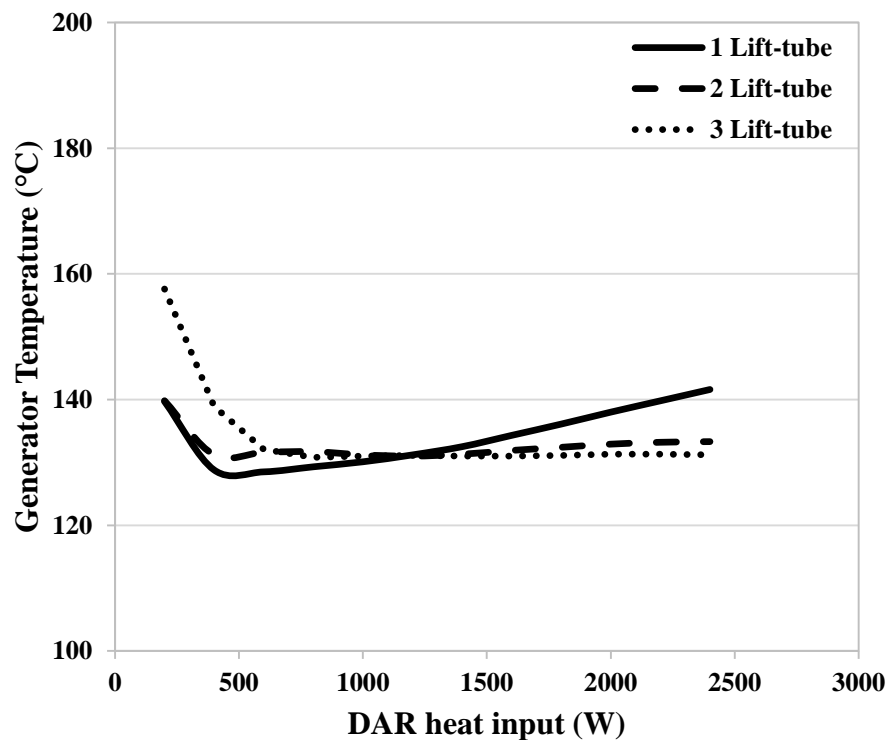


**Figure 78:** Influence of lift-tube quantity on generator temperature

It can be seen that at low heat input the temperature of the working fluid in the generator of the DAR system with single lift-tube bubble pump is less as compared to

multiple lift-tube bubble pump. By increasing the heat input, the generator temperature of the DAR system with a single lift-tube increases and eventually rises higher than the generator temperature of the multiple lift-tube bubble pump. The reason for this variation in the generator temperature is that when the rate of the working fluid flowing through the generator is less, a greater amount of heat is absorbed by the working fluid in the generator, which raises the temperature of the working fluid in the generator (Koyfman et al., 2003).

In Chapter 3, it was shown that as the temperature of the working fluid in the generator increases, the performance of the DAR system reduces. Now, due to the variations in the temperature of the working fluid in the generators of single and multiple lift-tube bubble pump, one would expect variations in the cooling produced, as shown in Figure 79.

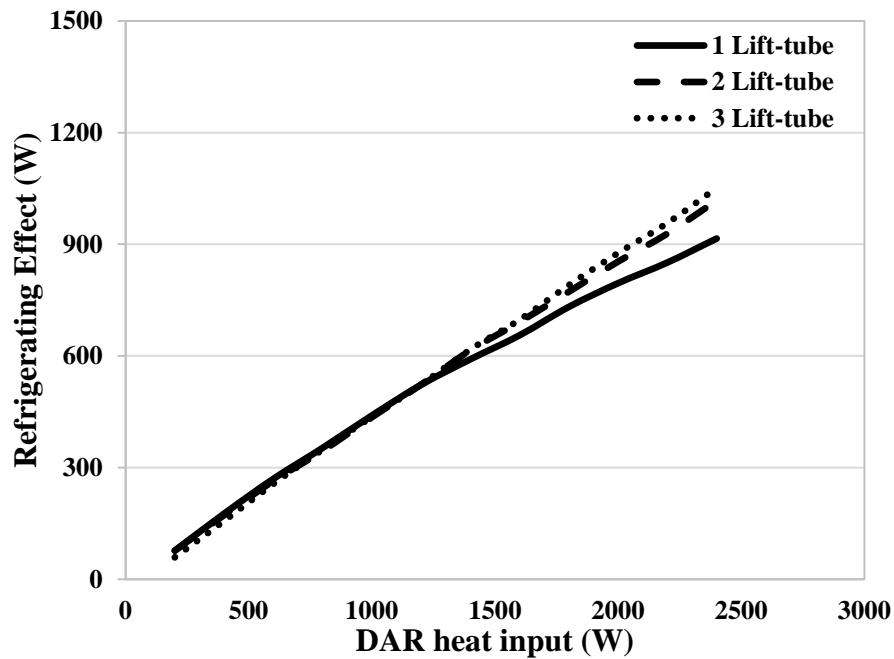


**Figure 79:** Influence of lift-tube quantity on cooling effect

It can be seen that at low heat input the use of the multiple lift-tube does not improve the cooling capacity of the DAR system, due to high generator temperature. However, at



high heat inputs, multiple lift-tubes show an increase in the refrigeration effect due to low generator temperatures, because of improved pumping performance. Additionally, Figure 80 shows the comparison between the performance of the DAR system with single and multiple lift-tube suggesting that for high values of heat input, the operating range of the DAR system can be improved by using a multiple lift-tube bubble pump. However, for low heat input the use of a single lift-tube bubble pump in a DAR system is more beneficial.

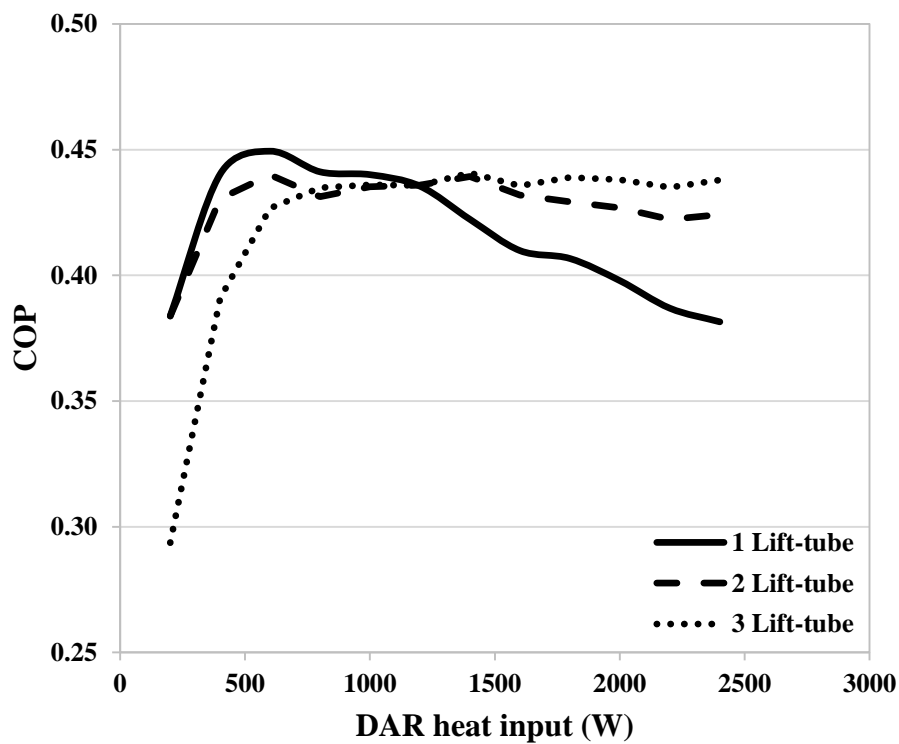


**Figure 80:** Influence of lift-tube quantity on the performance of DAR system

After studying the influence of the lift-tube quantity on the performance of the DAR system. It was decided to analyse the influence of the DAR system with single and multiple lift-tube on the performance of the tri-generation system. For this purpose, the values of the brake power and the heating produced were taken from the preliminary experimental investigation of the tri-generation system studied in Chapter 2, whereas

the values shown in Figure 79 were taken as the refrigeration produced by the DAR system with single and a multiple lift-tube bubble pump. Hence, the output of the tri-generation system is the sum of the brake power, heating, and cooling capacity.

Figure 81 shows the influence of the DAR system with single and multiple lift-tube bubble pump on the amount of useful energy produced by the tri-generation system. It can be seen that by using a DAR system with a multiple lift-tube bubble pump in a tri-generation setup, both the useful output energy and operating range for such a type of tri-generation system can be improved.

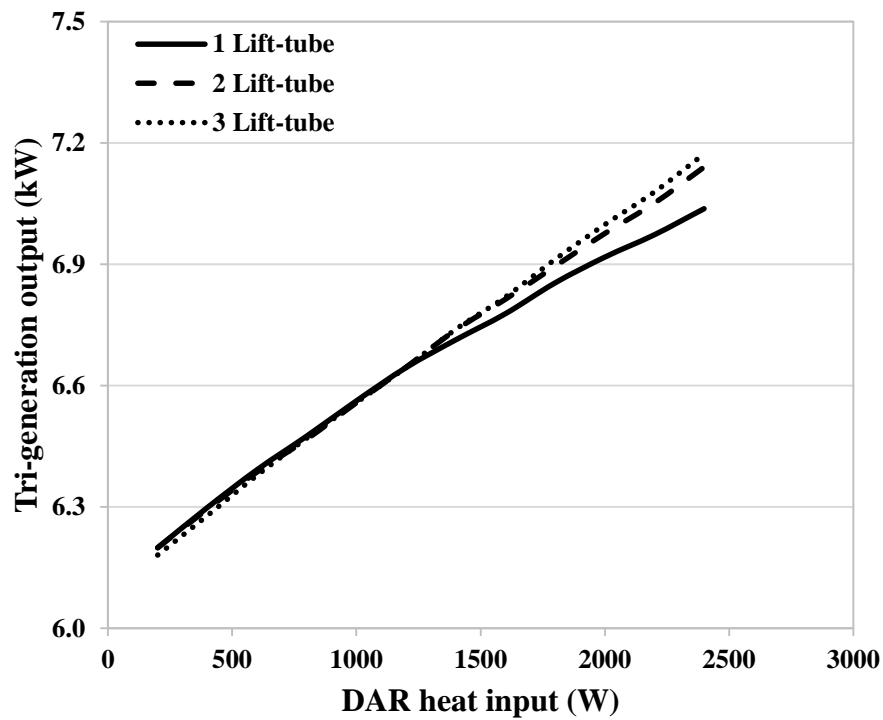


**Figure 81:** Influence of the DAR system with single and multiple lift-tube on the output of the tri-generation system

## 7.4 Conclusion

In this chapter, the influence of the lift-tube quantity on the performance of the DAR system was studied. The pumping performance of the bubble pumps with single and

multiple lift-tube were evaluated using the analytical model of the single lift-tube bubble pump and the ANN model of the multiple lift-tube bubble pump.

The results of the analysis showed that the performance of the DAR system is affected by the lift-tube quantity of the bubble pump due to the variation in the amount of liquid pumped. The variation in the pumping performance of both the single and multiple lift-tube bubble pumps influence their generator temperature, which affects the performance of the DAR system.

It was shown that the multiple lift-tube bubble pump showed greater performance at high heat input, thus improving the operating range of the DAR system. Furthermore, it was shown that for a tri-generation system employing a DAR system, both the performance and the operating range of such type to tri-generation system can be improved by using a DAR system with a multiple lift-tube bubble pump.

## **Chapter 8: Conclusions and recommendations**

### **8.1 Conclusions**

In this study, it was shown that there are number of areas where significant improvements can be made in order to increase the performance of the internal combustion engine based tri-generation system. In particular, a DAR system makes an ideal candidate as a cooling system. Notably, the characteristic of the DAR system to be driven solely by the waste heat energy without the need of any work input ensures that all the engine shaft work is utilised in the generation of other forms of energy.

In the preliminary experimental investigation, it was found that the performance of the DAR system reduces at high generating temperatures. As such, a sensitivity analysis of the DAR system was performed in order to understand the factors that affect the performance of the DAR system. It was found that the generator temperature influences the performance of the DAR system. Variations in the generator temperature affect the amount of the working fluid flow through the bubble pump of the DAR system.

It was shown that the pumping performance of the bubble pump is governed by the occurrence of different two-phase flow regimes. As such, empirical correlations were developed to model the behaviour of the bubble pump while operating in a particular flow regime. However, it was found that the bubble pumps with a single lift-tube were limited by the amount of the liquid they can pump. As such, it was suggested that the use of multiple lift-tubes could improve the pumping performance of the bubble pump, which would eventually increase the performance of the DAR system.

It was shown that while an analytical model was able to predict the pumping performance of the single lift-tube bubble pump, it was not able to predict the characteristics of a bubble pump with multiple lift-tube. In this regard, the predictions of an analytical model for a multiple lift-tube bubble pump significantly deviate from experimental results.

To address this, it was suggested that the artificial intelligence technique could be taken to better predict the behaviour of the two-phase flow. The performance of the bubble pump with multiple lift-tubes was predicted using the ANN technique. The predictions of the ANN modelling technique suggest that within its training bounds, ANN is an extremely efficient technique in predicting the performance of a multiple lift-tube bubble pump. Furthermore, the ANN model developed using the experimental value from an airlift pump was able to predict the performance of a heat driven bubble pump.

Finally, the performance of the DAR system using bubble pumps with single and multiple lift-tube was predicted. It was shown that by using multiple lift-tubes the amount of the liquid pumped by the bubble pump influences the generator temperature as more liquid is being pumped. This improves the cooling performance and the operating range of the DAR system, eventually making the tri-generation system more efficient.

## **8.2 Recommendations**

Besides the work that has been done regarding the utilisation of waste heat from an internal combustion engine, there are number of areas that could be explored to improve the efficiency of tri-generation systems. The demand of the energy from tri-generation

systems will vary based on the weather conditions. As such, control strategies can be designed for managing the output energy from such type of tri-generation system.

The occurrence of different flow regimes inside a bubble pump led to the development of flow regime based empirical correlations. However, a single empirical correlation that can predict the behaviour of a bubble pump for all the flow regimes will be a challenge. In a multiple lift-tube bubble pump, the prediction of the amount of air distribution in each lift-tube is a challenge. As such, multi-phase CFD simulations could significantly improve the understanding of flow distribution in each lift-tube.

It was noted that at low heat inputs the pumping performance of multiple lift-tube bubble pump is less than that of single lift-tube bubble pump. This limits the application of a multiple lift-tube bubble pump for low heat inputs. To overcome this, valves can be installed in the lift-tubes so that the flow through the multiple lift-tube bubble pump could be controlled based on the heat input and generator temperature.

Finally, the presence of the inert gas may provide shielding for the mass transfer between the weak solution and refrigerant vapour. This may cause unabsorbed refrigerant vapour to return to the evaporator, resulting in decreased performance of the system. As such, it would be interesting to analyse the influence of different types of absorbers on the performance of the DAR system.

## References

- Ahn, T. H., Yun, B. J. and Jeong, J. J., 2015, "Void fraction prediction for separated flows in the nearly horizontal tubes", *Nuclear Engineering and Technology*, Vol. 47, No. 6, pp. 669-677
- Al-Naser, M., Elshafei, M. and Al-Sarkhi, A., 2016, "Artificial neural network application for multiphase flow patterns detection: A new approach", *Journal of Petroleum Science and Engineering*, Vol. 145, pp. 548-564
- An, L., Liu, D., Chen, Y., Yang, L., Yang, M. and Lin, F., 2017, "Theoretical and experimental study on the lifting performance of bubble pump with variable cross-section lift tube", *Applied Thermal Engineering*, Vol. 111, pp. 1265-1271
- Angrisani, G., Roselli, C. and Sasso, M., 2012, "Distributed microtrigeneration systems", *Energy*, Vol. 38, No. 4, pp. 502-521
- Awad, M. M. and Muzychka, Y. S., 2008, "Effective property models for homogenous two-phase flow", *Experimental Thermal and Fluid Science*, Vol. 33, pp. 106-113
- Azizi, S., Ahmadloo, E. and Awad, M. M., 2016a, "Prediction of void fraction for gas-liquid flow in horizontal, upward and downward inclined pipes using artificial neural network", *International Journal of Multiphase Flow*, Vol. 87, pp. 35-44
- Azizi, S., Awad, M. M. and Ahmadloo, E., 2016b, "Prediction of water holdup in vertical and inclined oil-water two-phase flow using artificial neural network", *International Journal of Multiphase Flow*, Vol. 80, pp. 181-187
- Baikin, M., Taitel, Y. and Barnea, D., 2011, "Flow rate distribution in parallel heated pipes", *International Journal of Heat and Mass Transfer*, Vol. 54, No. 19-20, pp. 4448-4457
- Bar, N. and Das, S. K., 2013, "Prediction of flow regime for air-water flow in circular micro channels using ANN", *Procedia Technology*, Vol. 10, pp. 242-252
- Bar, N., Bandyopadhyay, T. K., Biswas, M. N. and Das, S. K., 2010, "Prediction of pressure drop using artificial neural network for non-Newtonian liquid flow through piping components", *Journal of Petroleum Science and Engineering*, Vol. 71, pp. 187-194
- Bar, N., Das, S. K. and Biswas, M. N., 2013, "Prediction of frictional pressure drop using artificial neural network for air-water flow through U-bends", *Procedia Technology*, Vol. 10, pp. 813-821

- Beattie, D. R. H. and Whalley, P. B., 1982, "A simple two-phase frictional pressure drop calculation method", *International Journal of Multiphase Flow*, Vol. 8, No. 1, pp. 83-87
- Belman-Flores, J. M., Rodriguez-Muniz, J. L., Rubio-Maya, C., Ramirez-Minguela, J. J. and Perez-Garcia, V., 2014, "Energetic analysis of a diffusion-absorption system: A bubble pump under geometrical and operational conditions effects", *Applied Thermal Engineering*, Vol. 71, No. 1, pp. 1-10
- Ben Ezzine, N., Garma, R. and Bellagi, A., 2010, "A numerical investigation of a diffusion-absorption refrigeration cycle based on R124-DMAC mixture for solar cooling", *Energy*, Vol. 35, No. 5, pp. 1874-1883
- Benhmidene, A., Chaouchi, B., Gabai, S. and Bourouis, M., 2011, "Modelling of heat flux received by a bubble pump of absorption-diffusion refrigeration cycles", *Heat and Mass Transfer*, Vol. 47, No. 11, pp. 1341-1347
- Bhagwat, S. M. and Ghajar, A. J., 2014, "A flow pattern independent drift flux model based void fraction correlation for a wide range of gas-liquid two-phase flow", *International Journal of Multiphase Flow*, Vol. 59, pp. 186-205
- Bourseau, P. and Bugarel, R., 1986, "Absorption-diffusion machines: comparison of the performances of  $\text{NH}_3\text{H}_2\text{O}$  and  $\text{NH}_3\text{NaSCN}$ ", *International Journal of Refrigeration*, Vol. 9, No. 4, pp. 206-214
- Cacua, K., Olmos-Villalba, L., Herrera, B. and Gallego, A., 2016, "Experimental evaluation of a diesel-biogas dual fuel engine operated on micro-trigeneration system for power, drying and cooling", *Applied Thermal Engineering*, Vol. 100, pp. 762-767
- Cengel, Y. and Ghajar, A., 2014, "*Heat and Mass Transfer: Fundamentals and Applications*", McGraw-Hill, New York
- Chan, K. W. and McCulloch, M., 2013, "Analysis and modelling of water based bubble pump at atmospheric pressure", *International Journal of Refrigeration*, Vol. 36, No. 5, pp. 1521-1528
- Chen, J., Kim, J. K. and Herold, E. K., 1996, "Performance enhancement of a diffusion-absorption refrigerator", *International Journal of Refrigeration*, Vol. 19, No. 3, pp. 208-218
- Chen, L., Tian, Y. S. and Karayiannis, T. G., 2005, "The effect of tube diameter on vertical two-phase flow regimes in small tubes", *International Journal of Heat and Mass Transfer*, Vol. 49, pp. 4220-4230



- Chicco, G. and Mancarella, P., 2007, "Trigeneration primary energy saving evaluation for energy planning and policy development", *Energy Policy*, Vol. 35, No. 12, pp.6132-6144
- Delfos, R., Wisse, C. J and Oliemans, R. V. A., 2001, "Measurement of air-entrainment from a stationary Taylor bubble in a vertical tube", *International Journal of Multiphase Flow*, Vol. 27, pp. 1769-1787
- Deng, J., Wang, R. Z and Han, G. Y., 2011, "A review of thermally activated cooling technologies for combined cooling, heating and power systems", *Progress in Energy and Combustion Science*, Vol. 37, No. 2, pp. 172-203
- Ersoz, M. T., 2015, "Investigation the effects of different heat inputs supplied to the generator on the energy performance in diffusion absorption refrigeration systems", *International Journal of Refrigeration*, Vol. 54, pp.10-21
- Furukawa, T. and Fukano, T., 2001, "Effects of liquid viscosity on flow patterns in vertical upward gas-liquid two-phase flow", *International Journal of Multiphase Flow*, Vol. 27, No. 6, pp.1109-1126
- Garma, R., Stiriba, Y., Bourouis, M and Bellagi, A., 2014, "Numerical investigations of the heating distribution effect on the boiling flow in bubble pumps", *International Journal of Hydrogen Energy*, Vol. 39, No. 27, pp. 15256-15260
- Gelegenis, J. and Mavrotas, G., 2017, "An analytical study of critical factors in residential cogeneration optimization", *Applied Energy*, Vol. 185, pp.1625-1632
- GLACIER, 2014, "*Absorption Mini Fridge/Refrigerator Core Cooling Unit*", Zibo Glacier Electrical Appliance Company limited, Shandong
- Godefroy, J., Boukhanouf, R. and Riffat, S., 2007, "Design, testing and mathematical modelling of a small-scale CHP and cooling system (small CHP-ejector trigeneration)", *Applied Thermal Engineering*, Vol. 27, No. 1, pp. 68-77
- Goyal, R., Sharma, D., Gupta, P. K., Johar, D. and Sonar, D., 2015, "Performance and emission analysis of CI engine operated micro-trigeneration system for power, heating and space cooling", *Applied Thermal Engineering*, Vol. 75, pp. 817-825
- Griffith, P. and Wallis, G. B., 1961, "Two-phase slug flow", *Journal of Heat Transfer*, Vol. 83, No. 3, pp. 307-318
- Gurevich, B., Jelinek, M., Levy, A. and Borde, I., 2015, "Performance of a set of parallel bubble pumps operating with a binary solution of R134a-DMAC", *Applied Thermal Engineering*, Vol. 75, pp. 724-730

Han, X. H., Wang, S. K., He, W., Hao, N., Zeng, Z. Y., Wang, Q. and Chen, G. M., 2015, "Experimental investigations on the pumping performance of bubble pumps with organic solutions", *Applied Thermal Engineering*, Vol. 86, pp. 43-48d

Hanafizadeh, P., Ghanbarzadeh, S. and Saidi, M. H., 2011a, "Visual technique for detection of gas-liquid two-phase flow regime in the airlift pump", *Journal of Petroleum Science and Engineering*, Vol. 75, No. 3-4, pp. 327-335

Hanafizadeh, P., Saidi, M. H., Gheimasi, A. N. and Ghanbarzadeh, S., 2011b, "Experimental investigation of air-water, two-phase flow regimes in vertical mini pipe", *Scientia Iranica*, Vol. 18, No. 4, pp. 923-929

Hernandez-Santoyo, J. and Sanchez-Cifuentes, A., 2003, "Tri-generation: an alternative for energy savings", *Applied Energy*, Vol. 76, No. 1-3, pp. 219-227

Hewitt, G. F. and Roberts, D. N., 1969, "*Studies of two-phase flow patterns by simultaneous X-ray and flash photography*", United Kingdom Atomic Energy Authority Report, AERE-M 2159, Berkshire

Hibiki, T. and Ishii, M., 2002, "Distribution parameter and drift velocity of drift-flux model in bubble flow", *International Journal of Heat and Mass Transfer*, Vol. 45, No. 4, pp. 707-721

Hibiki, T. and Ishii, M., 2003, "One-dimensional drift-flux model and constitutive equations for relative motion between phases in various two-phase flow regimes", *International Journal of Heat and Mass Transfer*, Vol. 46, No. 25, pp. 4935-4948

Huangfu, Y., Wu, Y. J., Wang, Z. R., Kong, Q. X. and Wei, H. B., 2007, "Evaluation and analysis of novel micro-scale combined cooling heating and power (MCCHP) system", *Energy Conversion and Management*, Vol. 48, No. 5, pp. 1703-1709

Hughes, B. R., Chaudhry, H. N. and Ghani, S. A., 2011, "A review of sustainable cooling technologies in buildings", *Renewable and Sustainable Energy Reviews*, Vol. 15, No. 6, pp. 3112-3120

Hussain, A., Arif, S. M. and Aslam, M., 2017, "Emerging renewable and sustainable energy technologies: State of the art", *Renewable and Sustainable Energy Reviews*, Vol. 71, pp. 12-28

Isaacs, N., Saville-Smith, K., Camilleri, M. and Burrough, L., 2010, "Energy in New Zealand houses: comfort, physics and consumption", *Building Research and Information*, Vol. 38, No. 5, pp. 470-480

Ishii, M., 1977, "*One-dimensional drift-flux model and constitutive equations for relative motion between phases in various two-phase flow regimes*", Argonne National Laboratory Technical Report, ANL-77-47, USA

- Jakob, U., Eicker, S., Schneider, D. and Taki, H. A., 2008, "Simulation and experimental investigation into diffusion absorption cooling machines for air-conditioning applications", *Applied Thermal Engineering*, Vol. 28, No. 10, pp. 1138-1150
- Jelinek, M., Levy, A. and Borde, I., 2016, "The influence of the evaporator inlet conditions on the performance of a diffusion absorption refrigeration cycle", *Applied Thermal Engineering*, Vol. 99, pp. 979-987
- Johnson, I., Choate, W. T. and Davidson, A., 2008. "Waste Heat Recovery. Technology and Opportunities in US Industry", BCS, Inc., Laurel, MD (United States).
- Jradi, M. and Riffat, S., 2014, "Tri-generation systems: Energy policies, prime movers, cooling technologies, configurations and operation strategies", *Renewable and Sustainable Energy Reviews*, Vol. 32, pp. 396-415
- Kassab, S. Z., Kandil, H. A., Warda, H. A. and Ahmed, W. H., 2009, "Airlift pumps characteristics under two-phase flow conditions", *International Journal of Heat and Fluid Flow*, Vol. 30, No. 1, pp. 88-98
- Kazi, S. N., 2012, "An Overview of Heat Transfer Phenomena", InTech, Croatia
- Khatri, K. K., Sharma, D., Soni, L. S. and Tanwar, D., 2010, "Experimental investigation of CI engine operated Micro-Trigeneration system", *Applied Thermal Engineering*, Vol. 30, No. 11-12, pp. 1505-1509
- Kim, S. H., Sohn, C. H. and Hwang, J. Y., 2014, "Effects of tube diameter and submergence ratio on bubble pattern and performance of airlift pump", *International Journal of Multiphase Flow*, Vol. 58, pp. 195-204
- Kline, S. and McClintock, F., 1953, "Describing uncertainties in single-sample experiments", *Mechanical Engineering*, Vol. 75, No. 1, pp. 3-8
- Koyfman, A., Jelinek, M., Levy, A. and Borde, I., 2003, "An experimental investigation of bubble pump performance for diffusion absorption refrigeration system with organic working fluids", *Applied Thermal Engineering*, Vol. 23, No. 15, pp. 1881-1894
- Lahey, R. T. Jr., 1974, "Two-phase flow in boiling water nuclear reactors", Technical Report, NEDO--13388, USA
- Lin, F., Liu, D., Jiang, D., Yang, L. and Zhao, R., 2016, "An experimental study on the performance of guided bubble pump with multiple tubes", *Applied Thermal Engineering*, Vol. 106, pp. 1052-1061

Lin, L., Wang, Y., Shemmeri, T., Ruxton, T., Turner, S., Zeng, S., Huang, J., He, Y. and Huang, X., 2007, "An experimental investigation of a household size trigeneration", *Applied Thermal Engineering*, Vol. 27, No. 2, pp. 576-585

Long, Z., Luo, Y., Li, H., Bu, X. and Ma, W., 2013, "Performance analysis of a diffusion absorption refrigeration cycle working with TFE-TEGDME mixture", *Energy and Buildings*, Vol. 58, pp. 86-92

Malayeri, M. R., Muller-Steinhagen, H. and Smith, J. M., 2003, "Neural network analysis of void fraction in air/water two-phase flows at elevated temperatures", *Chemical Engineering and Processing: Process Intensification*, Vol. 42, No. 8-9, pp. 587-597

Miguez, L. J., Murillo, S., Porteiro, J. and Lopez, M. L., 2004, "Feasibility of a new domestic CHP trigeneration with heat pump: I. Design and development", *Applied Thermal Engineering*, Vol. 24, pp. 1409-1419

Miro, L., Gasia, J. and Cabeza, L. F., 2016, "Thermal energy storage (TES) for industrial waste heat (IWH) recovery: A review", *Applied Energy*, Vol. 179, pp. 284-301

Monsef, H., Zadegan, M. N. and Javaherdeh, K., 2012, "Design and construction of a low capacity pump-less absorption system", *Thermal Science*, Vol. 18, No. 2, pp. 577-590

Montoya, G., Lucas, D., Baglietto, E. and Liao, Y., 2016, "A review on mechanisms and models for the churn-turbulent flow regime", *Chemical Engineering Science*, Vol. 141, pp. 86-103

Morgado, A. O., Miranda, J. M., Araujo, J. D. P. and Campos, J. B. L. M., 2016, "Review on vertical gas-liquid slug flow", *International Journal of Multiphase Flow*, Vol. 85, pp. 348-368

Moussawi, H. A., Fardoun, F. and Louahlia, H., 2016, "Selection based on differences between cogeneration and trigeneration in various prime mover technologies", *Renewable and Sustainable Energy Reviews*, Vol. 74, pp. 491-511

Patek, J. and Klomfar, J., 1995, "Simple functions for fast calculations of selected thermodynamic properties of the ammonia-water system", *International Journal of Refrigeration*, Vol. 18, No. 4, pp. 228-234

Pfaff, M., Saravanan, R., Maiya, M. P. and Murthy, S. S., 1998, "Studies on bubble pump for a water-lithium bromide vapour absorption refrigerator", *International Journal of Refrigeration*, Vol. 21, pp. 452-562

Pringle, C. C., Ambrose, S., Azzopardi, B. J. and Rust, A. C., 2015, "The existence and behaviour of large diameter Taylor bubbles", *International Journal of Multiphase Flow*, Vol. 72, pp. 318-323

Pustyl'nik, L., Barnea, D. and Taitel, Y., 2006, "Prediction of two-phase flow distribution in parallel pipes using stability analysis", *AIChE Journal*, Vol. 52, pp. 3345-3552

Raj, N. T., Iniyan, S. and Goic, R., 2011, "A review of renewable energy based cogeneration", *Renewable and Sustainable Energy Reviews*, Vol. 15, No. 8 pp. 3640-3648

Ratner, M. and Glover, C., 2014, "*U.S. Energy: Overview and Key Statistics*", Congressional Research Service, R40187, USA

Rattner, A. G. and Garimella, S., 2011, "Energy harvesting, reuse and upgrade to reduce primary energy usage in the USA", *Energy*, Vol. 36, No.10, pp. 6172-6183

Rattner, A. S., 2015, *Single pressure absorption refrigeration systems for low-source-temperature applications*, PhD Thesis, Georgia Institute of Technology, USA

Richter, H. J., 1983, "Separated two-phase flow model: application to critical two-phase flow", *International Journal of Multiphase Flow*, Vol. 9, No.5, pp. 511-530

Rodriguez-Munoz, J. L. and Belman-Flores, J. M., 2014, "Review of diffusion-absorption refrigeration technologies", *Renewable and Sustainable Energy Reviews*, Vol. 30, pp. 145-153

Salgado, C. M., Pereira, C. M. N. A., Schirru, R. and Brandao, L. E. B., 2010, "Flow regime identification and volume fraction prediction in multiphase flows by means of gamma-ray attenuation and artificial neural networks", *Progress in Nuclear Energy*, Vol. 52, N. 6, pp. 555-562

Samaras, V. C. and Margaritis, D. P., 2005, "Two-phase flow regime maps for airlift pump vertical upward gas-liquid flow", *International Journal of Multiphase Flow*, Vol. 31, No. 6, pp. 757-766

Schlegel, J. P., Sawant, P., Paranjape, S., Ozar, B., Hibiki, T. and Ishii, M., 2009, "Void fraction and flow regime in adiabatic upward two-phase flow in large diameter vertical pipes", *Nuclear Engineering and Design*, Vol. 239, pp. 2864-2874

Shaban, H. and Tavoularis, S., 2014, "Identification of flow regime in vertical upward air-water pipe flow using differential pressure signals and elastic maps", *International Journal of Multiphase Flow*, Vol. 61, pp. 62-72

Singh, V., Gupta, I. and Gupta, H. O., 2007, “ANN-based estimator for distillation using Levenberg-Marquardt approach”, *Engineering Applications of Artificial Intelligence*, Vol. 20, No. 2, pp. 249-259

Situ, R., Hibiki, T., Brown, R. J., Hazuku, T. and Takamasa, T., 2011, “Flow regime transition criteria for two-phase flow at reduced gravity conditions”, *International Journal of Multiphase Flow*, Vol. 37, pp. 1165-1177

Sonar, D., Soni, S. L. and Sharma, D., 2014, “Micro-trigeneration for energy sustainability: Technologies, tools and trends”, *Applied Thermal Engineering*, Vol. 71, pp. 790-796

Sozen, A., Menlik, T. and Ozbas, E., 2012, “The effect of ejector on the performance of diffusion absorption refrigeration systems: An experimental study”, *Applied Thermal Engineering*, Vol. 33-34, pp. 44-53

Srikhirin, P. and Aphornratana, S., 2002, “Investigation of a diffusion absorption refrigerator”, *Applied Thermal Engineering*, Vol. 22, No. 11, pp. 1181-1193

Starace, G. and De Pascallis, L., 2012, “An advanced analytical model of the Diffusion Absorption Refrigerator cycle”, *International Journal of Refrigeration*, Vol. 35, No. 3, pp. 605-612

Starace, G. and De Pascallis, L., 2013, “An enhanced model for the design of Diffusion Absorption Refrigerators”, *International Journal of Refrigeration*, Vol. 36, No. 5, pp. 1495-1503

Sternling, V. C., 1965, “Two-phase flow theory and engineering decision”, *Award lecture presented at AIChE annual meeting*.

Stojkov, M., Hnatko, E., Kljajin, M., Zivic, M. and Hornung, K., 2011, “CHP and CCHP Systems Today”, *International Journal of Electrical and Computer Engineering Systems*, Vol. 2, No. 2, pp. 75-79

Taitel, Y. and Bornea, D., 1980, “Modeling flow pattern transition for steady upward gas-liquid flow in vertical tubes”, *AIChE Journal*, Vol. 26, pp. 345-354

Tighzert, H., Brahim, M., Kechroud, N. and Benabbas, F., 2013, “Effect of submergence ratio on the liquid phase velocity, efficiency and void fraction in an airlift pump”, *Journal of Petroleum Science and Engineering*, Vol. 110, pp. 155-161

Vicatos, G. and Bennett, A., 2007, “Multiple lift tube pumps boost refrigeration capacity in absorption plants”, *Journal of Energy in Southern Africa*, Vol. 18, No. 3, pp. 49-57

Von Platen, B. D. and Munters, C. G., 1928, “refrigerator”, *US Patent 1864562*

Wallis, G. B, 1969, “*One Dimensional Two-Phase Flow*”, McGraw-Hill, New York

Wang, T., Zhang, Y., Zhang, J., Peng, Z. and Shu, G., 2014, “Comparisons of system benefits and thermos-economics for exhaust energy recovery applied on a heavy-duty diesel engine and a light-duty vehicle gasoline engine”, *Energy Conversion and Management*, Vol. 84, pp. 97-107

Wang, Y., Huang, Y., Chiremba, E., Roskilly, A. P., Hewitt, N., Ding, Yulong., Wu, D., Yu, H., Chen, X., Li, Y., Huang, J., Wang, R., Wu, J., Xia, Z. and Tan, C., 2011, “An investigation of a household size trigeneration running with hydrogen”, *Applied Energy*, Vol. 88, pp. 2176-2182

White, S. J., 2001, *Bubble pump design and performance*, Master Thesis, Georgia Institute of Technology, USA

Woldesemayat, M. A. and Ghajar, A. J., 2007, “Comparison of void fraction correlations for different flow patterns in horizontal and upward inclined pipes”, *International Journal of Multiphase Flow*, Vol. 33, No. 4, pp. 347-370

Yildiz, A. and Ersoz, M. A., 2013, “Energy and exergy analyses of the diffusion absorption refrigeration system”, *Energy*, Vol. 60, pp. 407-415

Yildiz, A., Ersoz, M. A., and Gozmen, B., 2014, “Effect of insulation on the energy and exergy performances in Diffusion Absorption Refrigeration (DAR) systems”, *International Journal of Refrigeration*, Vol. 44, pp. 161-167

Zohar, A., Jelinek, M., Levy, A. and Borde, I., 2008, “The influence of the generator and bubble pump configuration on the performance of diffusion absorption refrigeration (DAR) system”, *International Journal of Refrigeration*, Vol. 31, No. 6, pp. 962-969

Zuber, N. and Findlay, J. A., 1965, “Average volume concentration in two-phase flow systems”, *Journal of Heat Transfer*, Vol. 87, No. 4, pp. 453-468

## Appendix A: Energy analysis

### A.1 Refrigeration effect

The refrigeration effect produced by the DAR system was calculated using Equation 71:

$$\dot{Q}_{evp} = h^* A_{evp} \left[ \left( \frac{T_{evpi} + T_{evpo}}{2} \right) - T_{amb} \right] \quad (71)$$

Where  $h^*$  is the convection coefficient,  $A_{evp}$  is the surface area of the evaporator,  $T_{evpi}$  and  $T_{evpo}$  are the inlet and exit temperature at the evaporator,  $T_{amb}$  is the ambient temperature.

The parameters  $A_{evp}$ ,  $T_{evpi}$ ,  $T_{evpo}$  and  $T_{amb}$  have been calculated and recorded during the time when the experiment was running whereas  $h^*$  is estimated using Equation 72:

$$Nu = \frac{h^* L_c}{k} \quad (72)$$

Where  $Nu$  is the Nusselt number,  $L_c$  is the characteristic length of the evaporator tube, and  $k$  is the thermal conductivity of the ambient air. It was assumed that the serpentine-type evaporator tube was analogous to a horizontal tube having a length equal to the serpentine length. In this regard, the Nusselt number for the evaporator tube under natural convection, as was the case in this study, can be estimated using Equation 73 (Cengel and Ghajar, 2014):

$$Nu = \left\{ 0.6 + \frac{0.387 Ra^{1/6}}{[1 + (0.469/Pr)^{9/16}]^{8/27}} \right\}^2 \quad (73)$$

Where  $Ra$  is the Rayleigh number and  $Pr$  is the Prandtl number of the ambient air. The Rayleigh number can be determined using Equation 74:



$$Ra = \frac{g\beta(T_{evp} - T_{amb})D_{evp}^3}{\nu^2} \quad (74)$$

Where  $g$  is the gravitational acceleration,  $\beta$  is the coefficient of volumetric expansion of air,  $D_{evp}$  is the diameter of the evaporator tube, and  $\nu$  is the kinematic viscosity of the air. The property database of Engineering Equation Solver (EES) was used to evaluate the parameters  $k$ ,  $Pr$  and  $\nu$  at the film temperature ( $T_{fm}$ ) given by Equation 75:

$$T_{fm} = \frac{\left(\frac{T_{evpi} + T_{evpo}}{2}\right) + T_{amb}}{2} \quad (75)$$

The coefficient of volumetric expansion ( $\beta$ ) for the ideal gases can be evaluated using Equation 76:

$$\beta = \frac{1}{T_{fm}} \quad (76)$$

## A.2 Heat transfer to DAR system

The heat transfer rate from the exhaust gas to the DAR system can be evaluated using Equation 77:

$$\dot{Q}_{gen} = \dot{m}_{ex}c_{pex}(T_{exi} - T_{exo}) \quad (77)$$

where  $\dot{Q}_{gen}$  is the heat input to the DAR system,  $T_{exi}$  and  $T_{exo}$  are the temperatures of the exhaust gas entering and leaving the DAR system,  $\dot{m}_{ex}$  is the mass flow rate of the exhaust gas, and  $c_{pex}$  is the specific heat of the exhaust gas which is assumed to be the same as of air for the ease of calculation. The mass flow rate of exhaust gas ( $\dot{m}_{ex}$ ) is evaluated by applying mass balance across the engine, which is given by Equation 78:

$$\dot{m}_{ex} = \dot{m}_f + \dot{m}_a \quad (78)$$

Where  $\dot{m}_f$  and  $\dot{m}_a$  are the mass flow rate of fuel and air. The mass flow rate of fuel ( $\dot{m}_f$ ) can be calculated using Equation 79:

$$\dot{m}_f = sfc\dot{W} \quad (79)$$

Where  $\dot{W}$  is the engine shaft work output and  $sfc$  is the specific fuel consumption, which was evaluated from the engine performance curve.

The mass flow rate of the induced air ( $\dot{m}_a$ ) can be calculated using Equation 80:

$$\dot{m}_a = \rho_a \dot{V}_a \quad (80)$$

Where  $\rho_a$  is the density of the air and  $\dot{V}_a$  is the volume flow rate of the air induced, which can be estimated by Equation 81:

$$\dot{V}_a = V_d \frac{N}{2} \eta_v \quad (81)$$

Where  $N$  is the speed of the engine,  $V_d$  is the displaced volume in the cylinder and  $\eta_v$  is the volumetric efficiency, which is assumed to be 90 percent. The displaced volume ( $V_d$ ) can be evaluated by Equation 82:

$$V_d = \frac{\pi}{4} B^2 L_s \quad (82)$$

Where  $B$  and  $L_s$  are the bore and stroke of the cylinder respectively. Their values were taken from the available engine data.

## Appendix B: Uncertainty analysis

To determine the uncertainties associated with the preliminary experimental investigation (Chapter 2), the method proposed by Kline and McClintock (1953) was adopted. According to this method, the uncertainty in the measurement is the function ( $R$ ) of the independent variables  $x_1, x_2, x_3, \dots, x_n$  used in its calculation and is given by Equation 83:

$$R = R(x_1, x_2, x_3, \dots, x_n) \quad (83)$$

If  $w_R$  is the uncertainty in the result of a measurement and the uncertainties in the independent variables are assumed with the same odds. Then  $w_R$  can be estimated using Equation 84:

$$w_R = \sqrt{\left(\frac{\partial R}{\partial x_1} w_1\right)^2 + \left(\frac{\partial R}{\partial x_2} w_2\right)^2 + \dots + \left(\frac{\partial R}{\partial x_n} w_n\right)^2} \quad (84)$$

In the preliminary experimental investigation, the thermocouple readings were taken using an 8-channel Picolog TC-08 data acquisition system. The thermocouples were calibrated with boiling and freezing point of the water at the local pressure as the measuring standard. The uncertainty of the thermocouples was determined to be  $\pm 0.4$  °C.

When determining the uncertainty in refrigerating effect, the refrigerating effect ( $\dot{Q}_{evp}$ ) is a function of the convection coefficient ( $h^*$ ), surface area of the

evaporator ( $A_{evp}$ ), inlet temperature ( $T_{evpi}$ ), exit temperature ( $T_{evpo}$ ), and ambient temperature ( $T_{amb}$ ) as shown in Equation 85:

$$\dot{Q}_{evp} = h^* A_{evp} \left[ \left( \frac{T_{evpi} + T_{evpo}}{2} \right) - T_{amb} \right] \quad (85)$$

Where the convection coefficient ( $h^*$ ) itself is a function of Nusselt number ( $Nu$ ), characteristic length ( $L_c$ ), and thermal conductivity ( $k$ ). The convection coefficient ( $h^*$ ) is estimated by determining the values of Nusselt number ( $Nu$ ) and Rayleigh number ( $Ra$ ).

Therefore, the uncertainty in determining the Rayleigh number, assuming uncertainty in the coefficient of volumetric expansion of air ( $\beta$ ) is 0.005, while the viscosity of the air ( $\nu$ ), and diameter of the evaporator tube ( $D_{evp}$ ) are zero, is given by Equation 86:

$$w_{Ra} = \sqrt{\left( \frac{\partial Ra}{\partial \beta} w_{\beta} \right)^2 + \left( \frac{\partial Ra}{\partial T_{evp}} w_{T_{evp}} \right)^2 + \left( \frac{\partial Ra}{\partial T_{amb}} w_{T_{amb}} \right)^2} \quad (86)$$

By substituting the values of the measurements and the associated uncertainty for each of them, the uncertainty in the Rayleigh number is approximately  $\pm 12\%$ . Where 45.41% is due to the coefficient of volumetric expansion of air, 27.29% is due to the evaporator temperature, and 27.29% is due to the ambient temperature.

The uncertainty in the Nusselt number, assuming uncertainty in the Prandtl number is zero, can be estimated from Equation 87:

$$w_{Nu} = \sqrt{\left(\frac{\partial Nu}{\partial Ra} w_{Ra}\right)^2} \quad (87)$$

By substituting the values of the measurements and the associated uncertainty, the uncertainty in the Nusselt number is approximately  $\pm 3\%$ .

The uncertainty in the convection coefficient, assuming uncertainty in the characteristic length and thermal conductivity are zero, is given by Equation 88:

$$w_{h^*} = \sqrt{\left(\frac{\partial h^*}{\partial Nu} w_{Nu}\right)^2} \quad (88)$$

By substituting the values of the measurements and the associated uncertainty, the uncertainty in the convection coefficient is approximately  $\pm 3\%$ . Finally, the uncertainty in the refrigerating effect, assuming uncertainty in the surface area of the evaporator is zero, can be estimated using Equation 89:

$$w_{\dot{Q}_{evp}} = \sqrt{\left(\frac{\partial \dot{Q}_{evp}}{\partial h^*} w_{h^*}\right)^2 + \left(\frac{\partial \dot{Q}_{evp}}{\partial T_{evp}} w_{T_{evp}}\right)^2 + \left(\frac{\partial \dot{Q}_{evp}}{\partial T_{amb}} w_{T_{amb}}\right)^2} \quad (89)$$

By substituting the values of the measurements and the associated uncertainty for each of them, the uncertainty in the refrigerating effect is approximately  $\pm 9\%$ . Where 11.52% is due to the convection coefficient, 44.24% is due to the evaporator temperature, and 44.24% is due to the ambient temperature.

## Appendix C: Predicting the performance of a heat driven bubble pump

In order to predict the values using an ANN model, the unseen input parameter should be one of the input parameters used in developing the model. However, in the case of Lin et al. (2016), the input parameter used in their experimental investigation was heat input at the saturation temperature of the working fluid. This heat input was not used as an input parameter in developing the ANN model. As such, the heat input was converted to the volumetric flow rate of the vapours. To achieve this, the heat input was first used to estimate the mass flow rate ( $\dot{m}_v$ ) of the vapour using Equation 90:

$$\dot{m}_v = \frac{\dot{Q}_{gen}}{h_{fg}} \quad (90)$$

Where  $\dot{Q}_{gen}$  is the amount of heat added in the bubble pump at the saturation temperature of the liquid and  $h_{fg}$  is the enthalpy of vaporisation.

Once the mass flow rate of the vapour was determined, it was converted to the volumetric flow rate by dividing it with the density of the vapour. Table 12 shows the volume flow rate of the vapours estimated at the saturation temperature for heat input in Lin et al. (2016) experiments.

**Table 12:** Estimated volumetric flow rate of vapour

Heat Input (W)	Mass flow rate of vapour (g/sec)	Volumetric flow rate of vapour (litre/min)
200	0.089	8.9
300	0.133	13.35
400	0.177	17.8
500	0.221	22.25
600	0.266	26.7
700	0.310	31.15
800	0.354	35.6
900	0.399	40.05
1000	0.443	44.5
1100	0.487	48.95

Once the volumetric flow rate of the vapour is estimated, it can be used as an unseen input parameter in the ANN model in order to predict the performance of the multiple lift-tube bubble pumps. In regards to this, Figure 82 shows the comparison between the predictions of ANN model and the experimental results of Lin et al. (2016) for a 10 mm single lift-tube bubble pump operating at the submergence ratio of 0.4.

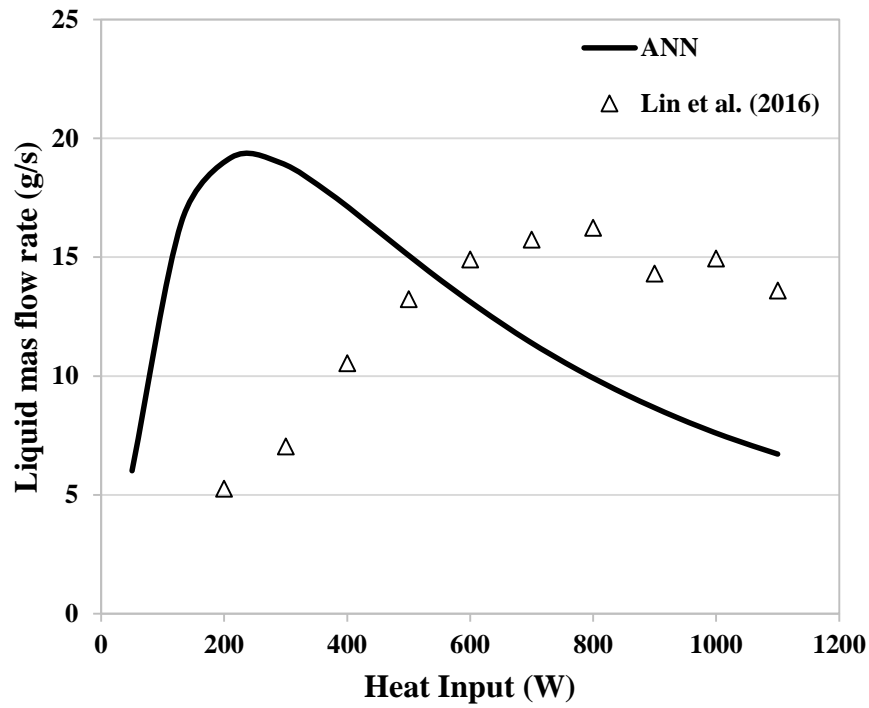


**Figure 82:** Comparison between ANN predictions and Lin et al. (2016) experimental values

It can be seen that there is a big variation between the predictions of the ANN model and the experimental values. Especially in the region when the heat input is maintained between 200 W to 500 W, the ANN model predicts a drop in the pumping performance of the bubble pump, whereas the experimental values show an increase in the pumping rate of the liquid.

While going through the different studies on heat-driven bubble pumps, it was found that the studies of Lin et al. (2016) and An et al. (2017) were performed by the same group of researchers using the same experimental setup. As such, the experimental performance of a heat driven single lift-tube bubble pump reported both by Lin et al. and An et al. at the same operating conditions were compared.



Figure 83 shows the comparison between the experimental values reported by Lin et al. and An et al. for a heat driven single lift-tube bubble pump having lift-tube diameter of 10 mm and operating at the submergence ratio of 0.4.

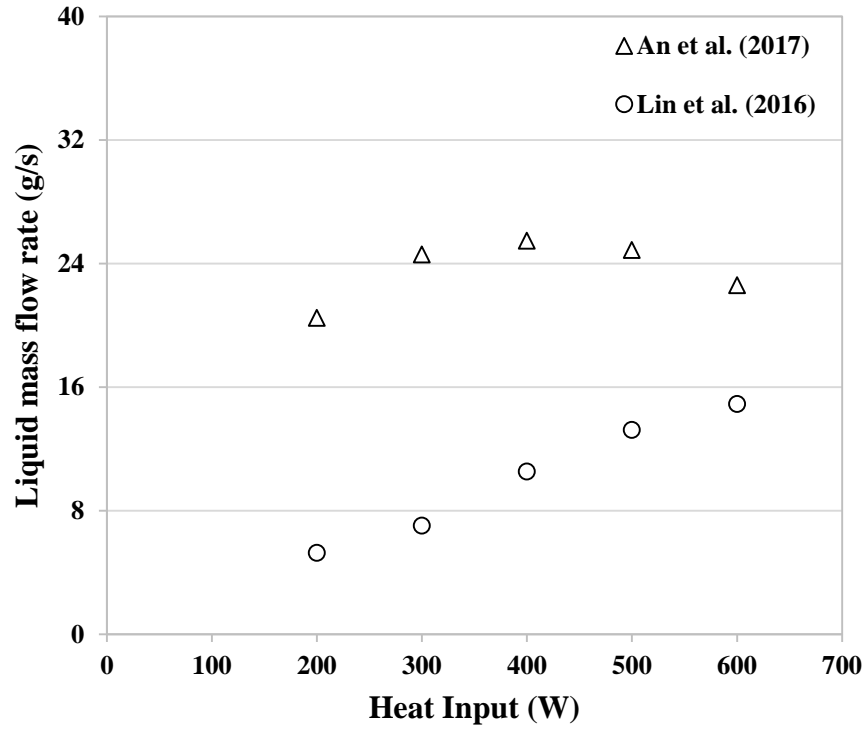


**Figure 83:** Comparison between experimental results of An et al. (2017) and Lin et al. (2016)

It was found that for similar operating conditions and the experimental setup there is a significant inconsistency between their experimental results. Lin et al. reports an increase in pumping rate with the increase of heat input whereas An et al. reports a decrease in pumping rate at higher heat input.

Furthermore, the experimental values of An et al. and Lin et al. were compared with the predictions of the analytical model of the single lift-tube developed in Chapter 4. Figure 84 shows that for similar operating conditions the model shows good agreements with

the experimental results of An et al. (2017) as compared to the experimental results of Lin et al. (2016).

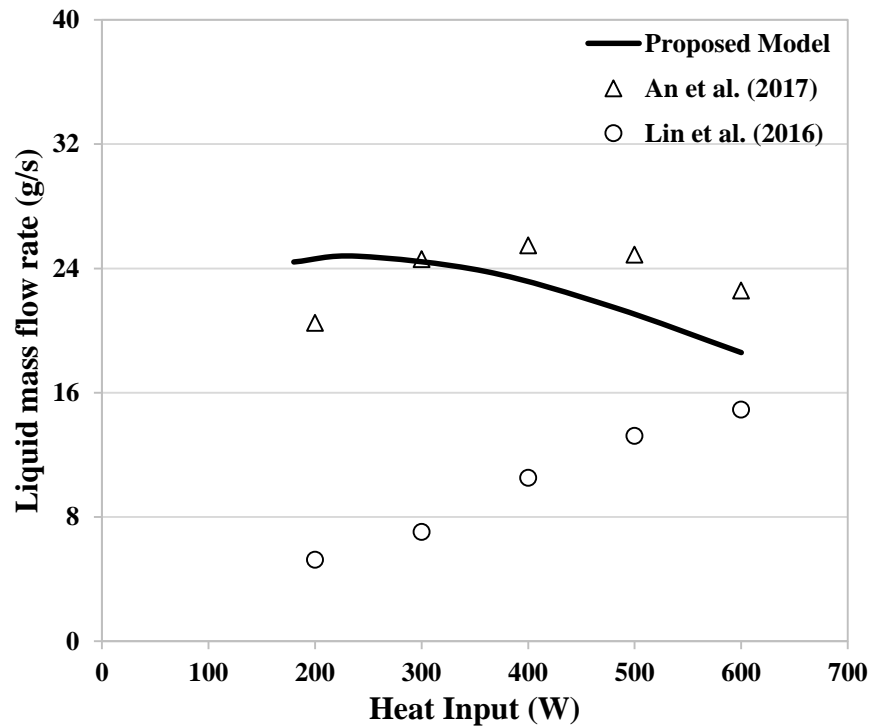


**Figure 84:** Comparison between results of analytical model and experimental results of An et al. (2017) and Lin et al. (2016)

Hence based on the experimental results of An et al. and predictions of the theoretical analytical model, it can be implied that there is a significant variation in the gas flow rate of Lin et al.

Now, by using the model of a single lift-tube bubble pump one could estimate the amount of vapour required to lift a certain volume of liquid. For this purpose, the experimental values of the liquid pumped as reported by Lin et al. for a single lift-tube bubble pump was used to estimate the amount of vapour. Table 13 shows both the amount of vapour generated using Equation 90 and the amount of vapour estimated using the analytical model.

**Table 13:** Estimated mass flow rate of vapour

Heat Input (W)	Mass flow rate of vapour (g/s)	
	$\dot{Q}_{gen} = \dot{m}_v h_{fg}$	Analytical Model
200	0.089	0.011
300	0.133	0.017
400	0.177	0.021
500	0.221	0.030
600	0.266	0.038
700	0.310	0.046
800	0.354	0.062
900	0.398	0.077
1000	0.442	0.090
1100	0.487	0.097

It was found that there is a significant difference in their values, which suggests that the actual amount of vapour generated during the experiments of Lin et al. was much less. Once the actual flow rate of the vapours is estimated using the analytical model, it was used as an unseen input parameter in the ANN model in order to estimate the amount of the liquid pumped using multiple lift-tubes.

In this regard, Figures 85 and 86 show the predictions of the ANN model for a heat-driven bubble pump with two and three lift-tubes.

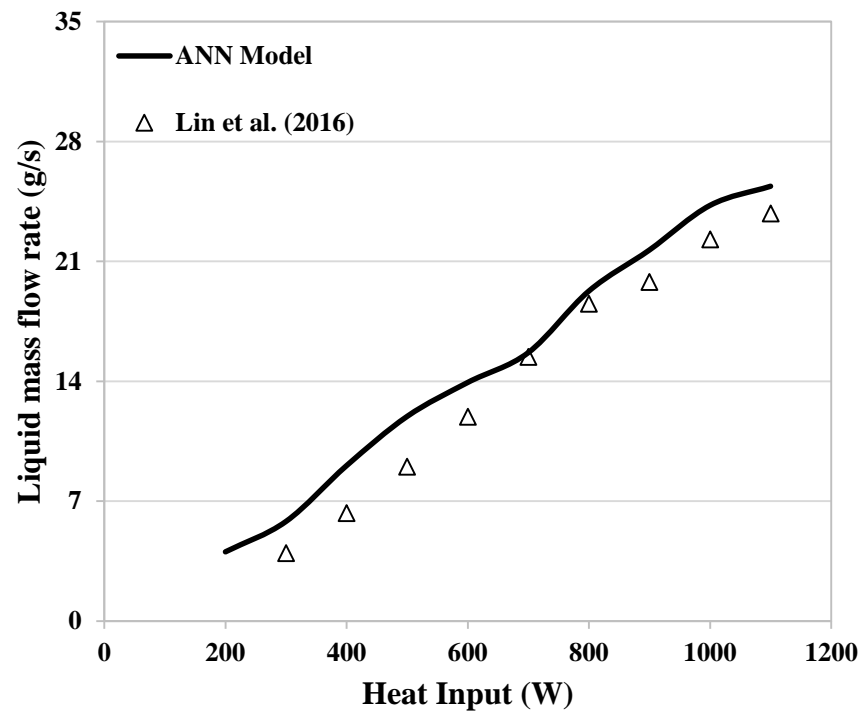


**Figure 85:** Comparison between the experimental results of Lin et al. (2016) and ANN predictions for 2 lift-tubes

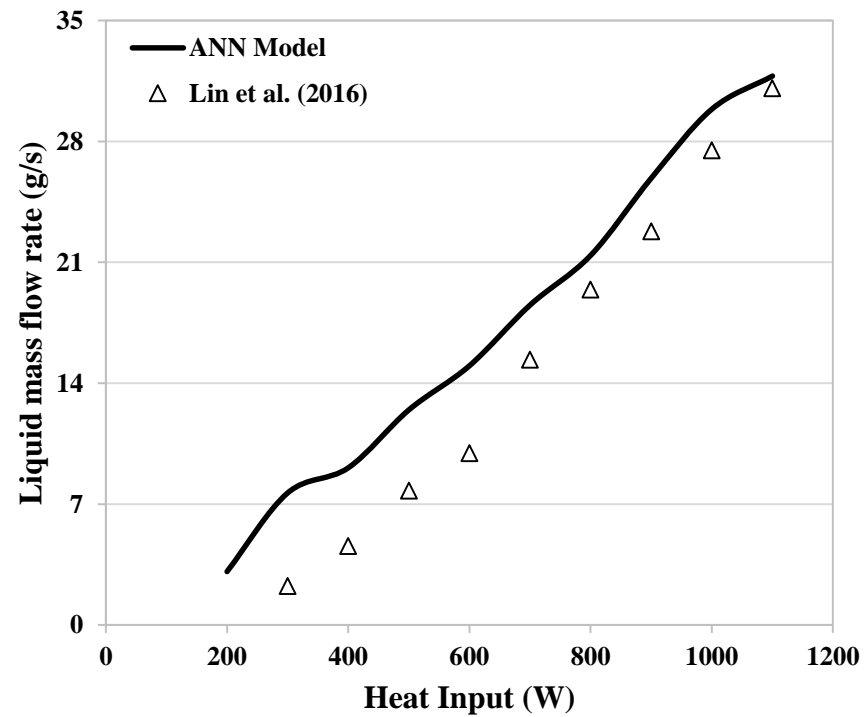


**Figure 86:** Comparison between the experimental results of Lin et al. (2016) and ANN predictions for 3 lift-tubes

## Appendix D: Experimental data of an airlift pump

Tube Diameter (mm)	Tube Length (mm)	Submergence Ratio	Tube Quantity	Airflow rate (litre/min)	Liquid pumped rate (litre/min)					
					Number of Readings					Average
					1	2	3	4	5	
8	500	0.3	1	0.05	0.000	0.000	0.000	0.000	0.000	0.000
8	500	0.3	1	0.10	0.000	0.000	0.000	0.000	0.000	0.000
8	500	0.3	1	0.20	0.000	0.000	0.000	0.000	0.000	0.000
8	500	0.3	1	0.30	0.005	0.005	0.005	0.010	0.005	0.006
8	500	0.3	1	0.40	0.035	0.030	0.030	0.030	0.035	0.032
8	500	0.3	1	0.80	0.090	0.100	0.090	0.090	0.095	0.093
8	500	0.3	1	1.20	0.210	0.220	0.220	0.220	0.220	0.218
8	500	0.3	1	1.60	0.310	0.320	0.310	0.310	0.310	0.312
8	500	0.3	1	2.00	0.410	0.415	0.415	0.410	0.410	0.412
8	500	0.3	1	2.40	0.460	0.470	0.460	0.460	0.460	0.462
8	500	0.3	1	2.80	0.540	0.540	0.530	0.530	0.530	0.534
8	500	0.3	1	3.20	0.560	0.560	0.550	0.560	0.550	0.556
8	500	0.3	1	3.60	0.540	0.540	0.540	0.550	0.540	0.542
8	500	0.3	1	4.00	0.530	0.530	0.530	0.540	0.530	0.532
8	500	0.3	1	4.40	0.520	0.520	0.525	0.525	0.520	0.522
8	500	0.3	1	4.80	0.50	0.50	0.5	0.5	0.50	0.54
8	500	0.3	1	6.00	0.480	0.480	0.480	0.470	0.480	0.478
8	500	0.3	1	8.00	0.440	0.450	0.440	0.440	0.440	0.442
8	500	0.3	1	10.00	0.430	0.435	0.430	0.430	0.430	0.431
8	500	0.3	1	14.00	0.440	0.440	0.450	0.440	0.440	0.442
8	500	0.3	1	18.00	0.460	0.460	0.460	0.460	0.460	0.460
8	500	0.3	1	22.00	0.450	0.450	0.450	0.460	0.450	0.452
8	500	0.3	1	26.00	0.440	0.440	0.450	0.440	0.440	0.442
8	500	0.3	1	30.00	0.430	0.430	0.430	0.430	0.430	0.430
8	500	0.3	1	34.00	0.420	0.430	0.420	0.420	0.420	0.422
8	500	0.3	1	38.00	0.410	0.420	0.410	0.410	0.420	0.414
8	500	0.3	1	42.00	0.400	0.410	0.410	0.410	0.400	0.406
8	500	0.3	1	46.00	0.390	0.400	0.400	0.390	0.390	0.394
8	500	0.3	1	50.00	0.380	0.380	0.380	0.370	0.380	0.378
8	500	0.5	1	0.05	0.015	0.020	0.015	0.020	0.020	0.018
8	500	0.5	1	0.10	0.055	0.060	0.055	0.060	0.055	0.057
8	500	0.5	1	0.20	0.120	0.110	0.110	0.120	0.120	0.116
8	500	0.5	1	0.30	0.150	0.150	0.140	0.140	0.150	0.146
8	500	0.5	1	0.40	0.160	0.160	0.160	0.170	0.160	0.162
8	500	0.5	1	0.80	0.620	0.630	0.620	0.620	0.630	0.624
8	500	0.5	1	1.20	0.900	0.900	0.920	0.910	0.910	0.908
8	500	0.5	1	1.60	1.200	1.210	1.190	1.190	1.190	1.196
8	500	0.5	1	2.00	1.220	1.220	1.220	1.230	1.220	1.222

8	500	0.5	1	2.40	1.260	1.260	1.250	1.250	1.260	1.256
8	500	0.5	1	2.80	1.270	1.270	1.280	1.280	1.270	1.274
8	500	0.5	1	3.20	1.220	1.210	1.210	1.210	1.210	1.212
8	500	0.5	1	3.60	1.180	1.180	1.190	1.190	1.180	1.184
8	500	0.5	1	4.00	1.170	1.170	1.170	1.180	1.170	1.172
8	500	0.5	1	4.40	1.160	1.160	1.160	1.160	1.160	1.160
8	500	0.5	1	4.80	1.140	1.130	1.130	1.140	1.130	1.134
8	500	0.5	1	6.00	1.100	1.100	1.050	1.050	1.100	1.080
8	500	0.5	1	8.00	0.950	0.950	0.980	0.980	0.970	0.966
8	500	0.5	1	10.00	0.940	0.930	0.930	0.940	0.940	0.936
8	500	0.5	1	14.00	0.890	0.900	0.900	0.900	0.890	0.896
8	500	0.5	1	18.00	0.870	0.880	0.880	0.870	0.880	0.876
8	500	0.5	1	22.00	0.860	0.840	0.860	0.850	0.850	0.852
8	500	0.5	1	26.00	0.800	0.810	0.810	0.800	0.810	0.806
8	500	0.5	1	30.00	0.780	0.790	0.790	0.780	0.780	0.784
8	500	0.5	1	34.00	0.770	0.760	0.760	0.760	0.770	0.764
8	500	0.5	1	38.00	0.740	0.740	0.730	0.740	0.730	0.736
8	500	0.5	1	42.00	0.700	0.710	0.710	0.700	0.710	0.706
8	500	0.5	1	46.00	0.690	0.680	0.690	0.680	0.690	0.686
8	500	0.5	1	50.00	0.660	0.660	0.650	0.660	0.660	0.658
8	500	0.7	1	0.05	0.020	0.020	0.015	0.015	0.020	0.018
8	500	0.7	1	0.10	0.300	0.300	0.320	0.320	0.300	0.308
8	500	0.7	1	0.20	0.630	0.600	0.620	0.620	0.620	0.618
8	500	0.7	1	0.30	0.890	0.900	0.900	0.890	0.890	0.894
8	500	0.7	1	0.40	1.140	1.140	1.130	1.130	1.130	1.134
8	500	0.7	1	0.80	1.430	1.430	1.430	1.440	1.430	1.432
8	500	0.7	1	1.20	1.700	1.700	1.690	1.700	1.690	1.696
8	500	0.7	1	1.60	1.850	1.850	1.850	1.860	1.860	1.854
8	500	0.7	1	2.00	1.900	1.890	1.890	1.890	1.900	1.894
8	500	0.7	1	2.40	1.930	1.930	1.940	1.930	1.930	1.932
8	500	0.7	1	2.80	2.100	2.120	2.100	2.100	2.110	2.106
8	500	0.7	1	3.20	2.150	2.150	2.160	2.150	2.150	2.152
8	500	0.7	1	3.60	2.170	2.170	2.170	2.180	2.170	2.172
8	500	0.7	1	4.00	2.200	2.200	2.190	2.190	2.200	2.196
8	500	0.7	1	4.40	2.210	2.220	2.220	2.220	2.210	2.216
8	500	0.7	1	4.80	2.230	2.230	2.220	2.230	2.230	2.228
8	500	0.7	1	6.00	2.200	2.200	2.190	2.200	2.190	2.196
8	500	0.7	1	8.00	2.060	2.050	2.050	2.050	2.050	2.052
8	500	0.7	1	10.00	1.880	1.880	1.900	1.900	1.900	1.892
8	500	0.7	1	14.00	1.760	1.760	1.760	1.750	1.760	1.758
8	500	0.7	1	18.00	1.600	1.590	1.600	1.580	1.590	1.592
8	500	0.7	1	22.00	1.460	1.460	1.470	1.470	1.460	1.464
8	500	0.7	1	26.00	1.400	1.390	1.380	1.380	1.380	1.386
8	500	0.7	1	30.00	1.300	1.310	1.300	1.300	1.300	1.302

8	500	0.7	1	34.00	1.210	1.220	1.210	1.210	1.200	1.210
8	500	0.7	1	38.00	1.150	1.160	1.150	1.140	1.150	1.150
8	500	0.7	1	42.00	1.040	1.050	1.050	1.040	1.050	1.046
8	500	0.7	1	46.00	0.980	0.980	0.970	0.980	0.980	0.978
8	500	0.7	1	50.00	0.900	0.900	0.900	0.910	0.910	0.904
8	500	0.3	2	0.05	0.000	0.000	0.000	0.000	0.000	0.000
8	500	0.3	2	0.10	0.000	0.000	0.000	0.000	0.000	0.000
8	500	0.3	2	0.20	0.000	0.000	0.000	0.000	0.000	0.000
8	500	0.3	2	0.30	0.010	0.010	0.010	0.015	0.010	0.011
8	500	0.3	2	0.40	0.015	0.020	0.020	0.015	0.020	0.018
8	500	0.3	2	0.80	0.075	0.070	0.070	0.065	0.075	0.071
8	500	0.3	2	1.20	0.100	0.095	0.100	0.100	0.100	0.099
8	500	0.3	2	1.60	0.280	0.270	0.280	0.280	0.280	0.278
8	500	0.3	2	2.00	0.360	0.350	0.360	0.370	0.360	0.360
8	500	0.3	2	2.40	0.460	0.450	0.450	0.450	0.440	0.450
8	500	0.3	2	2.80	0.480	0.470	0.470	0.460	0.470	0.470
8	500	0.3	2	3.20	0.530	0.530	0.540	0.550	0.550	0.540
8	500	0.3	2	3.60	0.580	0.590	0.590	0.600	0.590	0.590
8	500	0.3	2	4.00	0.650	0.640	0.650	0.660	0.650	0.650
8	500	0.3	2	4.40	0.720	0.720	0.720	0.710	0.730	0.720
8	500	0.3	2	4.80	0.740	0.740	0.730	0.750	0.730	0.738
8	500	0.3	2	6.00	0.790	0.780	0.790	0.790	0.790	0.788
8	500	0.3	2	8.00	0.810	0.820	0.810	0.810	0.810	0.812
8	500	0.3	2	10.00	0.800	0.800	0.800	0.810	0.800	0.802
8	500	0.3	2	14.00	0.770	0.790	0.780	0.780	0.770	0.778
8	500	0.3	2	18.00	0.760	0.750	0.760	0.760	0.760	0.758
8	500	0.3	2	22.00	0.740	0.750	0.740	0.740	0.730	0.740
8	500	0.3	2	26.00	0.730	0.720	0.720	0.720	0.720	0.722
8	500	0.3	2	30.00	0.710	0.710	0.710	0.710	0.700	0.708
8	500	0.3	2	34.00	0.690	0.700	0.690	0.690	0.690	0.692
8	500	0.3	2	38.00	0.670	0.670	0.665	0.670	0.670	0.669
8	500	0.3	2	42.00	0.650	0.660	0.655	0.660	0.655	0.656
8	500	0.3	2	46.00	0.650	0.660	0.650	0.650	0.645	0.651
8	500	0.3	2	50.00	0.650	0.645	0.645	0.650	0.645	0.647
8	500	0.5	2	0.05	0.020	0.015	0.020	0.020	0.020	0.019
8	500	0.5	2	0.10	0.055	0.060	0.060	0.060	0.055	0.058
8	500	0.5	2	0.20	0.140	0.130	0.140	0.140	0.130	0.136
8	500	0.5	2	0.30	0.150	0.145	0.150	0.150	0.145	0.148
8	500	0.5	2	0.40	0.160	0.170	0.170	0.170	0.165	0.167
8	500	0.5	2	0.80	0.300	0.290	0.300	0.300	0.290	0.296
8	500	0.5	2	1.20	0.50	0.490	0.50	0.50	0.490	0.496
8	500	0.5	2	1.60	0.870	0.880	0.880	0.870	0.880	0.876
8	500	0.5	2	2.00	0.910	0.920	0.920	0.920	0.910	0.916
8	500	0.5	2	2.40	0.940	0.950	0.940	0.940	0.940	0.942

8	500	0.5	2	2.80	0.970	0.960	0.960	0.970	0.960	0.964
8	500	0.5	2	3.20	1.050	1.060	1.060	1.050	1.060	1.056
8	500	0.5	2	3.60	1.170	1.180	1.180	1.170	1.180	1.176
8	500	0.5	2	4.00	1.320	1.310	1.320	1.310	1.310	1.314
8	500	0.5	2	4.40	1.370	1.380	1.380	1.380	1.370	1.376
8	500	0.5	2	4.80	1.450	1.440	1.440	1.440	1.450	1.444
8	500	0.5	2	6.00	1.550	1.540	1.540	1.550	1.550	1.546
8	500	0.5	2	8.00	1.650	1.660	1.660	1.650	1.660	1.656
8	500	0.5	2	10.00	1.640	1.640	1.640	1.630	1.640	1.638
8	500	0.5	2	14.00	1.570	1.560	1.560	1.560	1.570	1.564
8	500	0.5	2	18.00	1.400	1.390	1.400	1.400	1.400	1.398
8	500	0.5	2	22.00	1.320	1.320	1.320	1.330	1.320	1.322
8	500	0.5	2	26.00	1.250	1.250	1.240	1.250	1.240	1.246
8	500	0.5	2	30.00	1.190	1.190	1.200	1.190	1.200	1.194
8	500	0.5	2	34.00	1.150	1.150	1.140	1.150	1.150	1.148
8	500	0.5	2	38.00	1.110	1.110	1.100	1.110	1.100	1.106
8	500	0.5	2	42.00	1.050	1.060	1.040	1.040	1.050	1.048
8	500	0.5	2	46.00	1.020	1.010	1.010	1.020	1.020	1.016
8	500	0.5	2	50.00	0.990	0.980	0.990	0.995	0.990	0.989
8	500	0.7	2	0.05	0.115	0.115	0.120	0.115	0.120	0.117
8	500	0.7	2	0.10	0.135	0.130	0.135	0.130	0.130	0.132
8	500	0.7	2	0.20	0.240	0.250	0.245	0.250	0.245	0.246
8	500	0.7	2	0.30	0.480	0.475	0.480	0.480	0.475	0.478
8	500	0.7	2	0.40	0.530	0.525	0.530	0.530	0.530	0.529
8	500	0.7	2	0.80	0.800	0.790	0.800	0.800	0.790	0.796
8	500	0.7	2	1.20	1.270	1.275	1.280	1.280	1.275	1.276
8	500	0.7	2	1.60	1.600	1.590	1.600	1.600	1.590	1.596
8	500	0.7	2	2.00	1.670	1.660	1.660	1.660	1.670	1.664
8	500	0.7	2	2.40	1.740	1.750	1.740	1.740	1.750	1.744
8	500	0.7	2	2.80	1.840	1.850	1.850	1.840	1.850	1.846
8	500	0.7	2	3.20	1.910	1.910	1.910	1.900	1.910	1.908
8	500	0.7	2	3.60	2.110	2.100	2.110	2.110	2.100	2.106
8	500	0.7	2	4.00	2.130	2.140	2.140	2.130	2.140	2.136
8	500	0.7	2	4.40	2.200	2.210	2.210	2.200	2.210	2.206
8	500	0.7	2	4.80	2.290	2.280	2.290	2.280	2.290	2.286
8	500	0.7	2	6.00	2.400	2.390	2.390	2.400	2.390	2.394
8	500	0.7	2	8.00	2.500	2.490	2.500	2.500	2.490	2.496
8	500	0.7	2	10.00	2.550	2.550	2.560	2.560	2.550	2.554
8	500	0.7	2	14.00	2.330	2.330	2.320	2.330	2.320	2.326
8	500	0.7	2	18.00	2.150	2.160	2.160	2.150	2.160	2.156
8	500	0.7	2	22.00	2.050	2.050	2.040	2.050	2.040	2.046
8	500	0.7	2	26.00	1.870	1.870	1.880	1.880	1.870	1.874
8	500	0.7	2	30.00	1.710	1.720	1.720	1.710	1.720	1.716
8	500	0.7	2	34.00	1.640	1.650	1.640	1.650	1.650	1.646



8	500	0.7	2	38.00	1.450	1.450	1.440	1.440	1.450	1.446
8	500	0.7	2	42.00	1.350	1.350	1.360	1.350	1.360	1.354
8	500	0.7	2	46.00	1.340	1.340	1.340	1.330	1.340	1.338
8	500	0.7	2	50.00	1.310	1.320	1.320	1.320	1.310	1.316
8	500	0.3	3	0.05	0.000	0.000	0.000	0.000	0.000	0.000
8	500	0.3	3	0.10	0.000	0.000	0.000	0.000	0.000	0.000
8	500	0.3	3	0.20	0.000	0.000	0.000	0.000	0.000	0.000
8	500	0.3	3	0.30	0.000	0.000	0.000	0.000	0.000	0.000
8	500	0.3	3	0.40	0.000	0.000	0.000	0.000	0.000	0.000
8	500	0.3	3	0.80	0.005	0.025	0.015	0.015	0.010	0.014
8	500	0.3	3	1.20	0.040	0.045	0.035	0.035	0.035	0.038
8	500	0.3	3	1.60	0.125	0.125	0.130	0.125	0.125	0.126
8	500	0.3	3	2.00	0.170	0.185	0.180	0.180	0.175	0.178
8	500	0.3	3	2.40	0.270	0.270	0.260	0.270	0.270	0.268
8	500	0.3	3	2.80	0.310	0.290	0.300	0.300	0.290	0.298
8	500	0.3	3	3.20	0.380	0.370	0.380	0.380	0.380	0.378
8	500	0.3	3	3.60	0.410	0.400	0.400	0.400	0.410	0.404
8	500	0.3	3	4.00	0.450	0.440	0.440	0.440	0.450	0.444
8	500	0.3	3	4.40	0.50	0.50	0.490	0.50	0.50	0.498
8	500	0.3	3	4.80	0.540	0.520	0.520	0.530	0.520	0.526
8	500	0.3	3	6.00	0.690	0.680	0.690	0.680	0.680	0.684
8	500	0.3	3	8.00	0.860	0.880	0.880	0.870	0.880	0.874
8	500	0.3	3	10.00	1.120	1.090	1.120	1.110	1.120	1.112
8	500	0.3	3	14.00	1.280	1.220	1.220	1.230	1.220	1.234
8	500	0.3	3	18.00	1.220	1.280	1.270	1.280	1.270	1.264
8	500	0.3	3	22.00	1.260	1.280	1.280	1.270	1.280	1.274
8	500	0.3	3	26.00	1.260	1.300	1.290	1.300	1.290	1.288
8	500	0.3	3	30.00	1.320	1.300	1.310	1.310	1.300	1.308
8	500	0.3	3	34.00	1.240	1.260	1.260	1.250	1.260	1.254
8	500	0.3	3	38.00	1.200	1.220	1.220	1.210	1.220	1.214
8	500	0.3	3	42.00	1.180	1.180	1.170	1.180	1.180	1.178
8	500	0.3	3	46.00	1.120	1.160	1.160	1.150	1.160	1.150
8	500	0.3	3	50.00	1.140	1.120	1.130	1.120	1.120	1.126
8	500	0.5	3	0.05	0.000	0.000	0.000	0.000	0.000	0.000
8	500	0.5	3	0.10	0.040	0.040	0.050	0.050	0.040	0.044
8	500	0.5	3	0.20	0.090	0.090	0.090	0.080	0.090	0.088
8	500	0.5	3	0.30	0.160	0.170	0.160	0.160	0.160	0.162
8	500	0.5	3	0.40	0.200	0.190	0.200	0.195	0.200	0.197
8	500	0.5	3	0.80	0.305	0.310	0.310	0.300	0.310	0.307
8	500	0.5	3	1.20	0.580	0.590	0.590	0.590	0.580	0.586
8	500	0.5	3	1.60	0.860	0.850	0.850	0.850	0.860	0.854
8	500	0.5	3	2.00	0.940	0.930	0.930	0.940	0.930	0.934
8	500	0.5	3	2.40	0.990	0.980	0.990	0.995	0.990	0.989
8	500	0.5	3	2.80	1.020	1.030	1.020	1.020	1.020	1.022

8	500	0.5	3	3.20	1.060	1.050	1.060	1.070	1.060	1.060
8	500	0.5	3	3.60	1.220	1.220	1.210	1.210	1.220	1.216
8	500	0.5	3	4.00	1.530	1.540	1.530	1.530	1.530	1.532
8	500	0.5	3	4.40	1.760	1.750	1.750	1.760	1.750	1.754
8	500	0.5	3	4.80	1.840	1.830	1.830	1.840	1.830	1.834
8	500	0.5	3	6.00	1.930	1.920	1.920	1.930	1.920	1.924
8	500	0.5	3	8.00	2.050	2.040	2.040	2.050	2.040	2.044
8	500	0.5	3	10.00	2.040	2.030	2.040	2.030	2.030	2.034
8	500	0.5	3	14.00	1.990	1.980	1.980	1.990	1.990	1.986
8	500	0.5	3	18.00	1.930	1.930	1.930	1.940	1.930	1.932
8	500	0.5	3	22.00	1.910	1.910	1.920	1.920	1.910	1.914
8	500	0.5	3	26.00	1.800	1.790	1.800	1.800	1.790	1.796
8	500	0.5	3	30.00	1.750	1.750	1.740	1.750	1.750	1.748
8	500	0.5	3	34.00	1.660	1.660	1.670	1.670	1.670	1.666
8	500	0.5	3	38.00	1.620	1.300	1.620	1.620	1.620	1.556
8	500	0.5	3	42.00	1.490	1.490	1.480	1.480	1.490	1.486
8	500	0.5	3	46.00	1.470	1.460	1.460	1.470	1.470	1.466
8	500	0.5	3	50.00	1.440	1.450	1.430	1.440	1.440	1.440
8	500	0.7	3	0.05	0.230	0.240	0.240	0.240	0.230	0.236
8	500	0.7	3	0.10	0.120	0.130	0.120	0.120	0.120	0.122
8	500	0.7	3	0.20	0.190	0.180	0.190	0.190	0.190	0.188
8	500	0.7	3	0.30	0.380	0.380	0.370	0.380	0.370	0.376
8	500	0.7	3	0.40	0.450	0.440	0.440	0.450	0.440	0.444
8	500	0.7	3	0.80	0.800	0.800	0.810	0.810	0.800	0.804
8	500	0.7	3	1.20	1.430	1.440	1.430	1.430	1.430	1.432
8	500	0.7	3	1.60	1.680	1.670	1.670	1.680	1.670	1.674
8	500	0.7	3	2.00	1.900	1.890	1.890	1.900	1.890	1.894
8	500	0.7	3	2.40	2.200	2.190	2.190	2.200	2.190	2.194
8	500	0.7	3	2.80	2.240	2.230	2.240	2.240	2.240	2.238
8	500	0.7	3	3.20	2.460	2.450	2.450	2.460	2.450	2.454
8	500	0.7	3	3.60	2.780	2.770	2.770	2.780	2.770	2.774
8	500	0.7	3	4.00	2.840	2.850	2.840	2.840	2.840	2.842
8	500	0.7	3	4.40	2.970	2.970	2.970	2.960	2.970	2.968
8	500	0.7	3	4.80	3.100	3.100	3.000	3.000	3.000	3.040
8	500	0.7	3	6.00	3.180	3.170	3.170	3.180	3.170	3.174
8	500	0.7	3	8.00	3.370	3.360	3.360	3.360	3.370	3.364
8	500	0.7	3	10.00	3.400	3.410	3.410	3.400	3.410	3.406
8	500	0.7	3	14.00	3.520	3.530	3.520	3.520	3.530	3.524
8	500	0.7	3	18.00	3.640	3.640	3.630	3.630	3.640	3.636
8	500	0.7	3	22.00	3.560	3.550	3.550	3.560	3.550	3.554
8	500	0.7	3	26.00	3.450	3.440	3.440	3.440	3.450	3.444
8	500	0.7	3	30.00	3.260	3.260	3.260	3.270	3.260	3.262
8	500	0.7	3	34.00	3.150	3.140	3.140	3.150	3.140	3.144
8	500	0.7	3	38.00	2.990	2.980	2.980	2.990	2.980	2.984

8	500	0.7	3	42.00	2.900	2.890	2.890	2.900	2.890	2.894
8	500	0.7	3	46.00	2.760	2.760	2.750	2.750	2.760	2.756
8	500	0.7	3	50.00	2.700	2.700	2.710	2.710	2.710	2.706
10	500	0.3	1	0.05	0.000	0.000	0.000	0.000	0.000	0.000
10	500	0.3	1	0.10	0.000	0.000	0.000	0.000	0.000	0.000
10	500	0.3	1	0.20	0.000	0.000	0.000	0.000	0.000	0.000
10	500	0.3	1	0.30	0.000	0.000	0.000	0.000	0.000	0.000
10	500	0.3	1	0.40	0.000	0.000	0.000	0.000	0.000	0.000
10	500	0.3	1	0.80	0.050	0.060	0.055	0.060	0.055	0.056
10	500	0.3	1	1.20	0.190	0.190	0.185	0.185	0.190	0.188
10	500	0.3	1	1.60	0.290	0.290	0.285	0.290	0.290	0.289
10	500	0.3	1	2.00	0.380	0.370	0.380	0.370	0.380	0.376
10	500	0.3	1	2.40	0.430	0.420	0.420	0.430	0.420	0.424
10	500	0.3	1	2.80	0.480	0.480	0.470	0.480	0.470	0.476
10	500	0.3	1	3.20	0.50	0.50	0.490	0.50	0.50	0.498
10	500	0.3	1	3.60	0.540	0.560	0.550	0.550	0.540	0.548
10	500	0.3	1	4.00	0.570	0.580	0.570	0.580	0.580	0.576
10	500	0.3	1	4.40	0.590	0.590	0.600	0.590	0.590	0.592
10	500	0.3	1	4.80	0.600	0.590	0.600	0.600	0.590	0.596
10	500	0.3	1	6.00	0.560	0.570	0.570	0.570	0.570	0.568
10	500	0.3	1	8.00	0.530	0.550	0.540	0.540	0.540	0.540
10	500	0.3	1	10.00	0.50	0.50	0.50	0.50	0.490	0.498
10	500	0.3	1	14.00	0.530	0.530	0.540	0.530	0.530	0.532
10	500	0.3	1	18.00	0.570	0.570	0.580	0.570	0.570	0.572
10	500	0.3	1	22.00	0.600	0.600	0.610	0.600	0.600	0.602
10	500	0.3	1	26.00	0.610	0.620	0.610	0.610	0.610	0.612
10	500	0.3	1	30.00	0.620	0.630	0.620	0.620	0.620	0.622
10	500	0.3	1	34.00	0.640	0.640	0.630	0.640	0.640	0.638
10	500	0.3	1	38.00	0.640	0.640	0.630	0.640	0.630	0.636
10	500	0.3	1	42.00	0.630	0.630	0.620	0.630	0.630	0.628
10	500	0.3	1	46.00	0.620	0.610	0.620	0.620	0.620	0.618
10	500	0.3	1	50.00	0.600	0.600	0.610	0.600	0.600	0.602
10	500	0.5	1	0.05	0.015	0.015	0.010	0.015	0.010	0.013
10	500	0.5	1	0.10	0.045	0.045	0.040	0.045	0.040	0.043
10	500	0.5	1	0.20	0.075	0.092	0.088	0.088	0.088	0.086
10	500	0.5	1	0.30	0.130	0.130	0.125	0.130	0.125	0.128
10	500	0.5	1	0.40	0.140	0.145	0.130	0.135	0.140	0.138
10	500	0.5	1	0.80	0.400	0.410	0.390	0.395	0.400	0.399
10	500	0.5	1	1.20	0.740	0.730	0.730	0.740	0.730	0.734
10	500	0.5	1	1.60	0.940	0.950	0.950	0.945	0.950	0.947
10	500	0.5	1	2.00	1.100	1.090	1.090	1.095	1.090	1.093
10	500	0.5	1	2.40	1.340	1.200	1.200	1.250	1.200	1.238
10	500	0.5	1	2.80	1.280	1.260	1.300	1.280	1.280	1.280
10	500	0.5	1	3.20	1.400	1.390	1.390	1.395	1.390	1.393

10	500	0.5	1	3.60	1.500	1.470	1.430	1.450	1.450	1.460
10	500	0.5	1	4.00	1.490	1.440	1.440	1.450	1.440	1.452
10	500	0.5	1	4.40	1.480	1.480	1.440	1.445	1.445	1.458
10	500	0.5	1	4.80	1.520	1.400	1.560	1.500	1.500	1.496
10	500	0.5	1	6.00	1.420	1.440	1.420	1.420	1.440	1.428
10	500	0.5	1	8.00	1.390	1.380	1.380	1.390	1.380	1.384
10	500	0.5	1	10.00	1.280	1.260	1.260	1.260	1.270	1.266
10	500	0.5	1	14.00	1.200	1.220	1.210	1.210	1.200	1.208
10	500	0.5	1	18.00	1.200	1.210	1.180	1.200	1.200	1.198
10	500	0.5	1	22.00	1.190	1.190	1.190	1.200	1.190	1.192
10	500	0.5	1	26.00	1.195	1.195	1.190	1.185	1.195	1.192
10	500	0.5	1	30.00	1.180	1.180	1.190	1.180	1.180	1.182
10	500	0.5	1	34.00	1.160	1.165	1.160	1.158	1.160	1.161
10	500	0.5	1	38.00	1.145	1.140	1.140	1.138	1.140	1.141
10	500	0.5	1	42.00	1.125	1.128	1.125	1.125	1.125	1.126
10	500	0.5	1	46.00	1.105	1.110	1.110	1.105	1.105	1.107
10	500	0.5	1	50.00	0.995	0.990	0.990	0.990	0.995	0.992
10	500	0.7	1	0.05	0.012	0.010	0.011	0.011	0.012	0.011
10	500	0.7	1	0.10	0.185	0.190	0.190	0.185	0.190	0.188
10	500	0.7	1	0.20	0.480	0.50	0.490	0.50	0.480	0.490
10	500	0.7	1	0.30	0.720	0.730	0.720	0.730	0.720	0.724
10	500	0.7	1	0.40	0.880	0.900	0.900	0.915	0.900	0.899
10	500	0.7	1	0.80	1.360	1.360	1.352	1.350	1.360	1.356
10	500	0.7	1	1.20	1.700	1.540	1.860	1.820	1.800	1.744
10	500	0.7	1	1.60	2.000	2.000	2.000	2.000	2.000	2.000
10	500	0.7	1	2.00	2.130	2.130	2.213	2.200	2.100	2.155
10	500	0.7	1	2.40	2.260	2.260	2.260	2.260	2.260	2.260
10	500	0.7	1	2.80	2.340	2.360	2.346	2.346	2.346	2.348
10	500	0.7	1	3.20	2.373	2.373	2.400	2.375	2.375	2.379
10	500	0.7	1	3.60	2.400	2.386	2.386	2.373	2.386	2.386
10	500	0.7	1	4.00	2.400	2.373	2.400	2.400	2.400	2.395
10	500	0.7	1	4.40	2.400	2.413	2.426	2.410	2.410	2.412
10	500	0.7	1	4.80	2.426	2.426	2.426	2.426	2.426	2.426
10	500	0.7	1	6.00	2.413	2.400	2.400	2.400	2.400	2.403
10	500	0.7	1	8.00	2.240	2.226	2.226	2.240	2.240	2.234
10	500	0.7	1	10.00	2.106	2.133	2.120	2.120	2.133	2.122
10	500	0.7	1	14.00	1.973	1.946	1.960	1.946	1.960	1.957
10	500	0.7	1	18.00	1.720	1.706	1.720	1.720	1.706	1.714
10	500	0.7	1	22.00	1.693	1.706	1.706	1.693	1.707	1.701
10	500	0.7	1	26.00	1.673	1.675	1.670	1.675	1.670	1.673
10	500	0.7	1	30.00	1.626	1.626	1.613	1.626	1.613	1.621
10	500	0.7	1	34.00	1.570	1.580	1.580	1.570	1.580	1.576
10	500	0.7	1	38.00	1.550	1.550	1.550	1.530	1.540	1.544
10	500	0.7	1	42.00	1.490	1.495	1.500	1.495	1.495	1.495

10	500	0.7	1	46.00	1.455	1.450	1.440	1.450	1.445	1.448
10	500	0.7	1	50.00	1.405	1.400	1.395	1.400	1.405	1.401
10	500	0.3	2	0.05	0.000	0.000	0.000	0.000	0.000	0.000
10	500	0.3	2	0.10	0.000	0.000	0.000	0.000	0.000	0.000
10	500	0.3	2	0.20	0.000	0.000	0.000	0.000	0.000	0.000
10	500	0.3	2	0.30	0.000	0.000	0.000	0.000	0.000	0.000
10	500	0.3	2	0.40	0.000	0.000	0.000	0.000	0.000	0.000
10	500	0.3	2	0.80	0.045	0.040	0.040	0.040	0.040	0.041
10	500	0.3	2	1.20	0.145	0.140	0.145	0.140	0.140	0.142
10	500	0.3	2	1.60	0.165	0.170	0.170	0.170	0.165	0.168
10	500	0.3	2	2.00	0.215	0.200	0.210	0.205	0.205	0.207
10	500	0.3	2	2.40	0.245	0.250	0.245	0.245	0.245	0.246
10	500	0.3	2	2.80	0.300	0.290	0.295	0.290	0.290	0.293
10	500	0.3	2	3.20	0.355	0.355	0.350	0.350	0.350	0.352
10	500	0.3	2	3.60	0.400	0.400	0.390	0.400	0.400	0.398
10	500	0.3	2	4.00	0.440	0.440	0.420	0.440	0.440	0.436
10	500	0.3	2	4.40	0.520	0.50	0.50	0.50	0.50	0.54
10	500	0.3	2	4.80	0.560	0.540	0.540	0.540	0.540	0.544
10	500	0.3	2	6.00	0.600	0.620	0.610	0.620	0.620	0.614
10	500	0.3	2	8.00	0.730	0.700	0.740	0.730	0.730	0.726
10	500	0.3	2	10.00	0.860	0.870	0.890	0.880	0.880	0.876
10	500	0.3	2	14.00	0.890	0.890	0.880	0.880	0.890	0.886
10	500	0.3	2	18.00	0.870	0.860	0.850	0.860	0.860	0.860
10	500	0.3	2	22.00	0.840	0.840	0.860	0.840	0.850	0.846
10	500	0.3	2	26.00	0.830	0.830	0.830	0.830	0.820	0.828
10	500	0.3	2	30.00	0.820	0.820	0.840	0.820	0.820	0.824
10	500	0.3	2	34.00	0.820	0.810	0.810	0.810	0.820	0.814
10	500	0.3	2	38.00	0.810	0.810	0.810	0.810	0.810	0.810
10	500	0.3	2	42.00	0.800	0.810	0.800	0.800	0.800	0.802
10	500	0.3	2	46.00	0.800	0.810	0.800	0.790	0.800	0.800
10	500	0.3	2	50.00	0.800	0.800	0.790	0.800	0.790	0.796
10	500	0.5	2	0.05	0.005	0.002	0.005	0.004	0.005	0.004
10	500	0.5	2	0.10	0.025	0.020	0.020	0.022	0.025	0.022
10	500	0.5	2	0.20	0.055	0.050	0.050	0.050	0.055	0.052
10	500	0.5	2	0.30	0.100	0.095	0.095	0.095	0.100	0.097
10	500	0.5	2	0.40	0.110	0.115	0.115	0.110	0.115	0.113
10	500	0.5	2	0.80	0.230	0.235	0.230	0.230	0.235	0.232
10	500	0.5	2	1.20	0.410	0.400	0.400	0.405	0.400	0.403
10	500	0.5	2	1.60	0.600	0.610	0.600	0.605	0.605	0.604
10	500	0.5	2	2.00	0.900	0.890	0.890	0.895	0.890	0.893
10	500	0.5	2	2.40	1.030	1.020	1.030	1.030	1.020	1.026
10	500	0.5	2	2.80	1.160	1.140	1.160	1.140	1.150	1.150
10	500	0.5	2	3.20	1.220	1.220	1.220	1.225	1.220	1.221
10	500	0.5	2	3.60	1.320	1.325	1.330	1.330	1.330	1.327

10	500	0.5	2	4.00	1.380	1.375	1.375	1.375	1.380	1.377
10	500	0.5	2	4.40	1.410	1.410	1.405	1.410	1.405	1.408
10	500	0.5	2	4.80	1.520	1.510	1.510	1.500	1.510	1.510
10	500	0.5	2	6.00	1.770	1.765	1.765	1.770	1.765	1.767
10	500	0.5	2	8.00	2.020	2.010	2.010	2.020	2.010	2.014
10	500	0.5	2	10.00	2.320	2.320	2.310	2.310	2.320	2.316
10	500	0.5	2	14.00	2.280	2.260	2.260	2.265	2.260	2.265
10	500	0.5	2	18.00	2.220	2.220	2.220	2.210	2.220	2.218
10	500	0.5	2	22.00	2.120	2.120	2.110	2.115	2.115	2.116
10	500	0.5	2	26.00	2.040	2.070	2.040	2.045	2.045	2.048
10	500	0.5	2	30.00	2.000	2.000	1.990	2.000	1.995	1.997
10	500	0.5	2	34.00	1.960	1.960	1.955	1.960	1.960	1.959
10	500	0.5	2	38.00	1.920	1.925	1.925	1.920	1.925	1.923
10	500	0.5	2	42.00	1.900	1.905	1.900	1.905	1.905	1.903
10	500	0.5	2	46.00	1.840	1.860	1.855	1.855	1.855	1.853
10	500	0.5	2	50.00	1.820	1.810	1.820	1.820	1.820	1.818
10	500	0.7	2	0.05	0.040	0.030	0.030	0.030	0.025	0.031
10	500	0.7	2	0.10	0.180	0.175	0.180	0.175	0.175	0.177
10	500	0.7	2	0.20	0.450	0.470	0.480	0.470	0.470	0.468
10	500	0.7	2	0.30	0.700	0.710	0.690	0.710	0.705	0.703
10	500	0.7	2	0.40	0.880	0.880	0.885	0.890	0.880	0.883
10	500	0.7	2	0.80	1.200	1.195	1.200	1.200	1.205	1.200
10	500	0.7	2	1.20	1.430	1.425	1.425	1.430	1.425	1.427
10	500	0.7	2	1.60	1.670	1.660	1.670	1.670	1.670	1.668
10	500	0.7	2	2.00	1.970	1.980	1.970	1.970	1.980	1.974
10	500	0.7	2	2.40	2.060	2.040	2.060	2.070	2.060	2.058
10	500	0.7	2	2.80	2.230	2.240	2.230	2.230	2.220	2.230
10	500	0.7	2	3.20	2.240	2.250	2.250	2.250	2.250	2.248
10	500	0.7	2	3.60	2.270	2.280	2.280	2.260	2.270	2.272
10	500	0.7	2	4.00	2.340	2.330	2.340	2.340	2.330	2.336
10	500	0.7	2	4.40	2.380	2.380	2.370	2.380	2.370	2.376
10	500	0.7	2	4.80	2.460	2.440	2.460	2.450	2.460	2.454
10	500	0.7	2	6.00	2.760	2.760	2.750	2.760	2.750	2.756
10	500	0.7	2	8.00	2.880	2.870	2.880	2.880	2.870	2.876
10	500	0.7	2	10.00	3.190	3.180	3.180	3.190	3.190	3.186
10	500	0.7	2	14.00	3.020	3.030	3.020	3.020	3.010	3.020
10	500	0.7	2	18.00	2.750	2.750	2.740	2.750	2.740	2.746
10	500	0.7	2	22.00	2.630	2.640	2.640	2.630	2.640	2.636
10	500	0.7	2	26.00	2.540	2.540	2.550	2.540	2.540	2.542
10	500	0.7	2	30.00	2.440	2.450	2.440	2.450	2.450	2.446
10	500	0.7	2	34.00	2.390	2.390	2.380	2.390	2.380	2.386
10	500	0.7	2	38.00	2.340	2.340	2.330	2.340	2.340	2.338
10	500	0.7	2	42.00	2.290	2.280	2.280	2.290	2.280	2.284
10	500	0.7	2	46.00	2.210	2.210	2.200	2.210	2.210	2.208

10	500	0.7	2	50.00	2.240	2.230	2.240	2.240	2.230	2.236
10	500	0.3	3	0.05	0.000	0.000	0.000	0.000	0.000	0.000
10	500	0.3	3	0.10	0.000	0.000	0.000	0.000	0.000	0.000
10	500	0.3	3	0.20	0.000	0.000	0.000	0.000	0.000	0.000
10	500	0.3	3	0.30	0.000	0.000	0.000	0.000	0.000	0.000
10	500	0.3	3	0.40	0.000	0.000	0.000	0.000	0.000	0.000
10	500	0.3	3	0.80	0.005	0.025	0.015	0.015	0.010	0.014
10	500	0.3	3	1.20	0.040	0.045	0.035	0.035	0.035	0.038
10	500	0.3	3	1.60	0.125	0.125	0.130	0.125	0.125	0.126
10	500	0.3	3	2.00	0.170	0.185	0.180	0.180	0.175	0.178
10	500	0.3	3	2.40	0.270	0.270	0.260	0.270	0.270	0.268
10	500	0.3	3	2.80	0.310	0.290	0.300	0.300	0.290	0.298
10	500	0.3	3	3.20	0.380	0.370	0.380	0.380	0.380	0.378
10	500	0.3	3	3.60	0.410	0.400	0.400	0.400	0.410	0.404
10	500	0.3	3	4.00	0.450	0.440	0.440	0.440	0.450	0.444
10	500	0.3	3	4.40	0.50	0.50	0.490	0.50	0.50	0.498
10	500	0.3	3	4.80	0.540	0.520	0.520	0.530	0.520	0.526
10	500	0.3	3	6.00	0.690	0.680	0.690	0.680	0.680	0.684
10	500	0.3	3	8.00	0.860	0.880	0.880	0.870	0.880	0.874
10	500	0.3	3	10.00	1.120	1.090	1.120	1.110	1.120	1.112
10	500	0.3	3	14.00	1.280	1.220	1.220	1.230	1.220	1.234
10	500	0.3	3	18.00	1.220	1.280	1.270	1.280	1.270	1.264
10	500	0.3	3	22.00	1.260	1.280	1.280	1.270	1.280	1.274
10	500	0.3	3	26.00	1.260	1.300	1.290	1.300	1.290	1.288
10	500	0.3	3	30.00	1.320	1.300	1.310	1.310	1.300	1.308
10	500	0.3	3	34.00	1.240	1.260	1.260	1.250	1.260	1.254
10	500	0.3	3	38.00	1.200	1.220	1.220	1.210	1.220	1.214
10	500	0.3	3	42.00	1.180	1.180	1.170	1.180	1.180	1.178
10	500	0.3	3	46.00	1.120	1.160	1.160	1.150	1.160	1.150
10	500	0.3	3	50.00	1.140	1.120	1.130	1.120	1.120	1.126
10	500	0.5	3	0.05	0.000	0.000	0.000	0.000	0.000	0.000
10	500	0.5	3	0.10	0.010	0.050	0.015	0.015	0.010	0.020
10	500	0.5	3	0.20	0.075	0.080	0.075	0.075	0.075	0.076
10	500	0.5	3	0.30	0.105	0.105	0.110	0.105	0.105	0.106
10	500	0.5	3	0.40	0.140	0.130	0.145	0.140	0.140	0.139
10	500	0.5	3	0.80	0.240	0.225	0.240	0.240	0.235	0.236
10	500	0.5	3	1.20	0.5	0.470	0.480	0.480	0.480	0.484
10	500	0.5	3	1.60	0.770	0.780	0.760	0.760	0.770	0.768
10	500	0.5	3	2.00	0.900	0.920	0.910	0.900	0.910	0.908
10	500	0.5	3	2.40	1.100	1.080	1.080	1.090	1.080	1.086
10	500	0.5	3	2.80	1.210	1.230	1.220	1.220	1.220	1.220
10	500	0.5	3	3.20	1.220	1.250	1.220	1.220	1.230	1.228
10	500	0.5	3	3.60	1.350	1.390	1.380	1.370	1.370	1.372
10	500	0.5	3	4.00	1.620	1.580	1.610	1.595	1.600	1.601

10	500	0.5	3	4.40	1.790	1.780	1.790	1.790	1.780	1.786
10	500	0.5	3	4.80	1.900	1.920	1.910	1.910	1.900	1.908
10	500	0.5	3	6.00	1.940	1.950	1.940	1.940	1.940	1.942
10	500	0.5	3	8.00	2.490	2.460	2.480	2.480	2.470	2.476
10	500	0.5	3	10.00	2.850	2.880	2.880	2.880	2.870	2.872
10	500	0.5	3	14.00	3.120	3.120	3.110	3.120	3.120	3.118
10	500	0.5	3	18.00	3.060	3.060	3.070	3.070	3.080	3.068
10	500	0.5	3	22.00	3.090	3.060	3.060	3.060	3.060	3.066
10	500	0.5	3	26.00	2.940	2.970	2.960	2.960	2.950	2.956
10	500	0.5	3	30.00	2.910	2.910	2.920	2.910	2.910	2.912
10	500	0.5	3	34.00	2.820	2.850	2.840	2.840	2.840	2.838
10	500	0.5	3	38.00	2.790	2.820	2.810	2.820	2.820	2.812
10	500	0.5	3	42.00	2.670	2.700	2.680	2.690	2.680	2.684
10	500	0.5	3	46.00	2.640	2.670	2.660	2.660	2.660	2.658
10	500	0.5	3	50.00	2.610	2.580	2.600	2.590	2.600	2.596
10	500	0.7	3	0.05	0.050	0.070	0.070	0.070	0.060	0.064
10	500	0.7	3	0.10	0.135	0.165	0.170	0.165	0.165	0.160
10	500	0.7	3	0.20	0.355	0.390	0.315	0.380	0.380	0.364
10	500	0.7	3	0.30	0.480	0.550	0.570	0.560	0.560	0.544
10	500	0.7	3	0.40	0.710	0.750	0.740	0.740	0.750	0.738
10	500	0.7	3	0.80	1.230	1.220	1.220	1.220	1.230	1.224
10	500	0.7	3	1.20	1.570	1.590	1.590	1.580	1.590	1.584
10	500	0.7	3	1.60	2.280	2.290	2.280	2.280	2.290	2.284
10	500	0.7	3	2.00	2.460	2.450	2.450	2.450	2.450	2.452
10	500	0.7	3	2.40	2.640	2.560	2.560	2.570	2.570	2.580
10	500	0.7	3	2.80	2.720	2.640	2.710	2.710	2.720	2.700
10	500	0.7	3	3.20	2.900	2.860	2.880	2.880	2.900	2.884
10	500	0.7	3	3.60	3.120	3.040	3.040	3.040	3.050	3.058
10	500	0.7	3	4.00	3.040	3.000	3.040	3.040	3.040	3.032
10	500	0.7	3	4.40	3.200	3.200	3.200	3.180	3.180	3.192
10	500	0.7	3	4.80	3.200	3.240	3.220	3.220	3.220	3.220
10	500	0.7	3	6.00	3.560	3.500	3.520	3.520	3.520	3.524
10	500	0.7	3	8.00	3.880	3.820	3.880	3.880	3.860	3.864
10	500	0.7	3	10.00	4.500	4.380	4.400	4.390	3.390	4.212
10	500	0.7	3	14.00	4.620	4.560	4.560	4.560	4.560	4.572
10	500	0.7	3	18.00	4.620	4.620	4.620	4.610	4.620	4.618
10	500	0.7	3	22.00	4.560	4.590	4.570	4.560	4.560	4.568
10	500	0.7	3	26.00	4.410	4.380	4.400	4.400	4.400	4.398
10	500	0.7	3	30.00	4.200	4.230	4.220	4.220	4.210	4.216
10	500	0.7	3	34.00	4.170	4.110	4.120	4.120	4.120	4.128
10	500	0.7	3	38.00	4.020	3.990	4.000	4.010	4.010	4.006
10	500	0.7	3	42.00	3.960	3.900	3.920	3.920	3.910	3.922
10	500	0.7	3	46.00	3.900	3.840	3.860	3.860	3.860	3.864
10	500	0.7	3	50.00	3.720	3.780	3.770	3.760	3.760	3.758



14	500	0.3	1	0.05	0.000	0.000	0.000	0.000	0.000	0.000
14	500	0.3	1	0.10	0.000	0.000	0.000	0.000	0.000	0.000
14	500	0.3	1	0.20	0.000	0.000	0.000	0.000	0.000	0.000
14	500	0.3	1	0.30	0.000	0.000	0.000	0.000	0.000	0.000
14	500	0.3	1	0.40	0.000	0.000	0.000	0.000	0.000	0.000
14	500	0.3	1	0.80	0.000	0.000	0.000	0.000	0.000	0.000
14	500	0.3	1	1.20	0.000	0.000	0.000	0.000	0.000	0.000
14	500	0.3	1	1.60	0.000	0.000	0.000	0.000	0.000	0.000
14	500	0.3	1	2.00	0.000	0.000	0.000	0.000	0.000	0.000
14	500	0.3	1	2.40	0.040	0.035	0.040	0.040	0.035	0.038
14	500	0.3	1	2.80	0.105	0.100	0.100	0.110	0.100	0.103
14	500	0.3	1	3.20	0.260	0.250	0.260	0.250	0.250	0.254
14	500	0.3	1	3.60	0.350	0.350	0.360	0.360	0.350	0.354
14	500	0.3	1	4.00	0.420	0.410	0.420	0.410	0.420	0.416
14	500	0.3	1	4.40	0.50	0.50	0.490	0.50	0.490	0.496
14	500	0.3	1	4.80	0.540	0.550	0.560	0.550	0.540	0.548
14	500	0.3	1	6.00	0.650	0.640	0.660	0.650	0.650	0.650
14	500	0.3	1	8.00	0.780	0.800	0.790	0.790	0.780	0.788
14	500	0.3	1	10.00	0.860	0.860	0.860	0.855	0.850	0.857
14	500	0.3	1	14.00	0.980	0.920	0.930	0.930	0.920	0.936
14	500	0.3	1	18.00	1.060	1.040	1.050	1.050	1.060	1.052
14	500	0.3	1	22.00	1.040	1.040	1.060	1.050	1.060	1.050
14	500	0.3	1	26.00	1.080	1.100	1.090	1.100	1.090	1.092
14	500	0.3	1	30.00	1.120	1.120	1.110	1.120	1.110	1.116
14	500	0.3	1	34.00	1.180	1.170	1.160	1.170	1.170	1.170
14	500	0.3	1	38.00	1.220	1.200	1.210	1.200	1.210	1.208
14	500	0.3	1	42.00	1.260	1.270	1.260	1.250	1.255	1.259
14	500	0.3	1	46.00	1.320	1.320	1.310	1.320	1.310	1.316
14	500	0.3	1	50.00	1.340	1.360	1.350	1.350	1.360	1.352
14	500	0.5	1	0.05	0.000	0.000	0.000	0.000	0.000	0.000
14	500	0.5	1	0.10	0.000	0.000	0.000	0.000	0.000	0.000
14	500	0.5	1	0.20	0.000	0.000	0.000	0.000	0.000	0.000
14	500	0.5	1	0.30	0.000	0.000	0.000	0.000	0.000	0.000
14	500	0.5	1	0.40	0.000	0.000	0.000	0.000	0.000	0.000
14	500	0.5	1	0.80	0.105	0.100	0.100	0.095	0.100	0.100
14	500	0.5	1	1.20	0.225	0.230	0.230	0.240	0.230	0.231
14	500	0.5	1	1.60	0.490	0.480	0.485	0.480	0.490	0.485
14	500	0.5	1	2.00	0.780	0.780	0.770	0.780	0.780	0.778
14	500	0.5	1	2.40	1.020	1.010	1.020	1.010	1.020	1.016
14	500	0.5	1	2.80	1.240	1.230	1.240	1.230	1.220	1.232
14	500	0.5	1	3.20	1.430	1.440	1.440	1.440	1.430	1.436
14	500	0.5	1	3.60	1.600	1.580	1.580	1.590	1.590	1.588
14	500	0.5	1	4.00	1.680	1.680	1.680	1.670	1.670	1.676
14	500	0.5	1	4.40	1.800	1.790	1.780	1.800	1.790	1.792

14	500	0.5	1	4.80	1.900	1.910	1.920	1.910	1.920	1.912
14	500	0.5	1	6.00	2.080	2.090	2.100	2.090	2.100	2.092
14	500	0.5	1	8.00	2.240	2.280	2.270	2.260	2.270	2.264
14	500	0.5	1	10.00	2.360	2.360	2.350	2.360	2.360	2.358
14	500	0.5	1	14.00	2.400	2.460	2.440	2.440	2.450	2.438
14	500	0.5	1	18.00	2.440	2.400	2.410	2.410	2.400	2.412
14	500	0.5	1	22.00	2.400	2.400	2.380	2.390	2.400	2.394
14	500	0.5	1	26.00	2.320	2.390	2.380	2.380	2.380	2.370
14	500	0.5	1	30.00	2.380	2.360	2.370	2.370	2.360	2.368
14	500	0.5	1	34.00	2.400	2.400	2.390	2.390	2.380	2.392
14	500	0.5	1	38.00	2.380	2.390	2.400	2.390	2.400	2.392
14	500	0.5	1	42.00	2.410	2.400	2.400	2.400	2.410	2.404
14	500	0.5	1	46.00	2.400	2.400	2.420	2.410	2.410	2.408
14	500	0.5	1	50.00	2.480	2.440	2.450	2.440	2.440	2.450
14	500	0.7	1	0.05	0.000	0.000	0.000	0.000	0.000	0.000
14	500	0.7	1	0.10	0.000	0.000	0.000	0.000	0.000	0.000
14	500	0.7	1	0.20	0.000	0.000	0.000	0.000	0.000	0.000
14	500	0.7	1	0.30	0.200	0.195	0.200	0.200	0.200	0.199
14	500	0.7	1	0.40	0.460	0.480	0.460	0.465	0.460	0.465
14	500	0.7	1	0.80	1.200	1.220	1.200	1.200	1.205	1.205
14	500	0.7	1	1.20	1.880	1.920	1.890	1.900	1.890	1.896
14	500	0.7	1	1.60	2.320	2.360	2.330	2.340	2.340	2.338
14	500	0.7	1	2.00	2.640	2.640	2.635	2.640	2.640	2.639
14	500	0.7	1	2.40	2.880	2.880	2.880	2.880	2.875	2.879
14	500	0.7	1	2.80	3.120	3.050	3.060	3.060	3.050	3.068
14	500	0.7	1	3.20	3.280	3.320	3.290	3.290	3.280	3.292
14	500	0.7	1	3.60	3.440	3.420	3.440	3.440	3.430	3.434
14	500	0.7	1	4.00	3.600	3.580	3.580	3.590	3.580	3.586
14	500	0.7	1	4.40	3.660	3.650	3.660	3.660	3.660	3.658
14	500	0.7	1	4.80	3.760	3.770	3.770	3.765	3.760	3.765
14	500	0.7	1	6.00	3.910	3.900	3.910	3.910	3.900	3.906
14	500	0.7	1	8.00	4.000	4.040	3.920	4.000	4.000	3.992
14	500	0.7	1	10.00	4.000	4.000	3.995	3.995	4.000	3.998
14	500	0.7	1	14.00	3.920	3.920	3.910	3.910	3.920	3.916
14	500	0.7	1	18.00	3.800	3.760	3.770	3.760	3.770	3.772
14	500	0.7	1	22.00	3.720	3.660	3.680	3.660	3.670	3.678
14	500	0.7	1	26.00	3.600	3.640	3.600	3.630	3.620	3.618
14	500	0.7	1	30.00	3.600	3.630	3.600	3.610	3.610	3.610
14	500	0.7	1	34.00	3.640	3.600	3.620	3.620	3.610	3.618
14	500	0.7	1	38.00	3.600	3.610	3.600	3.600	3.610	3.604
14	500	0.7	1	42.00	3.620	3.580	3.600	3.590	3.580	3.594
14	500	0.7	1	46.00	3.600	3.620	3.600	3.610	3.600	3.606
14	500	0.7	1	50.00	3.630	3.610	3.610	3.610	3.605	3.613

